SETTER DESIGN FOR BINDER REMOVAL FROM INJECTION-MOLDED CERAMIC COMPONENTS

by

CESARE MONTI

B.S. Aerospace Engineering, Texas A&M University
(1994)

Submitted to the Department of
Materials Science and Engineering in
Partial Fulfillment of the Requirements
for the Degree of

MASTER OF SCIENCE

at the
Massachusetts Institute of Technology

June 1996

Signature of Author _____
Department of Materials Science and Engineering
May 10, 1996

Certified by _____
Michael J. Cima
Norton Professor of Ceramics
Thesis Supervisor

Accepted by _____
Michael F. Rubner
TDK Professor of Materials Science and Engineering
Chair, Departmental Committee on Graduate Students

SETTER DESIGN FOR BINDER REMOVAL FROM INJECTION-MOLDED CERAMIC COMPONENTS

by

CESARE MONTI

Submitted to the Department of Materials Science and Engineering
on May 10, 1996 in partial fulfillment of the requirements
for the Degree of Master of Science
in Materials Science and Engineering

ABSTRACT

Distortions in injection-molded ceramic components are introduced during the thermolysis cycle due to slumping of the green body as well as binder concentration gradients imparted by localized binder removal. Extraction of the liquefied binder system immediately after melting is essential in reducing the extent of deformation. Injection-molded samples with two types of binder systems where heat treated at low temperatures on several types of porous setters and different interface geometries. Wicking behavior was found to be dependent on binder viscosity, setter porosity, and sample/setter interface geometry and area. Study of binder removal rates showed that these increased non-linearly with increasing interfacial area. Binder fluxes were proven to be dependent on binder migration distance within the sample. Deformation due to creep was modeled with a final element analysis tool and compared with experimental results from samples heat treated over non-porous setters. Excellent agreement was found between theoretical and experimental deformation rates. Deformation behavior was found to be conspicuously different in samples heat treated over porous setters. The results suggested that deformation due to creep and those due to uneven binder removal throughout the sample were highly coupled.

Thesis Supervisor: Dr. Michael J. Cima

Title: Norton Professor of Ceramics

TABLE OF CONTENTS

LIST OF FIGURES

Chapter 2

Chapter 3

Chapter 4

LIST OF TABLES

Chapter 1

Chapter 2

Chapter 3

Chapter 4

ACKNOWLEDGMENTS

A friend of mine, Kevin, told me more than two years ago, that MIT would completely change my life in ways I could never even imagine. At the time I thought the guy was "clueless" and did not know what he was talking about. It turns out I was the "clueless" one. I was completely unaware of the unpredictable changes that MIT was going to "rush" into my life. Within the last year and a half everything regarding my existence, my prospects for the future, my perception of the past, has been, in one way or another, changed, sometimes for better, sometimes for worse. There is no doubt in my mind that this brief experience has enriched me deeply. I would like to dedicate this thesis to all the people that have made these changes possible.

My deepest gratitude goes to my parents, Anna Maria and Giancarlo, for always supporting and believing in me. To Myrna Sharpe, who treats me like her own son, my sister Marianna, my grandparents Erminia and Aldo, my cousin Lara, my uncle Marco, my aunt Mimma and her husband Angel, thanks for being as wonderful as you all are. This is what really amazes me. No matter how questionable and senseless many of my decisions may have been, you have always stood behind me; always, in good and bad times.

My gratitude and admiration go to Prof. Michael Cima, for guiding me through this year and a half of research and for sharing his wisdom and vision. To Barbara Layne (the Dragon Lady), John Centorino, and Leonard Rigione, thank you for all the help (and tons of patience!) you have given me. To Karina, Kamala, Jae, Scotty, and Todd, thanks for being the best office mates in the world; I don't think I will ever get a better office environment than this. Karina, thanks for listening, listening, and listening for months in a row. My thanks to the whole CPRL gang, Michael, Jason, Bugra, Lynne, Bill, Ben, Ken, Satbir, Daniel, Jack, John, Kevin, Neville, Wendell, Bob, and Man-Fai, for being great people to work with and talk to. A special thanks to Ken for sharing thesis editing nightmares with me; good luck in New York! I will really miss CPRL!

I would also like to thank Bobby and all my friends back in Italy, especially Marco, Antonio, and Gianluca because it is great to come back home and find old friends. A special thanks to Margherita: I don't know how this comes about after all that has happened, but thanks for five unforgettable years.

Finally, but not last, I would like to thank two people that have showed me the importance of living fully and intensely: Kirsten and, her husband, Alessandro. You are not forgotten.

1. INTRODUCTION AND BACKGROUND

1.1 INJECTION MOLDING

The use of ceramics has seen, and is currently experiencing, a dramatic growth in high technology fields as electronics and optics. Ceramics can be used to create devices, components, with mechanical, electrical, thermal, and chemical properties unmatched by either metals or polymers. Creating ceramic components, however, is not an easy task. Conventional forming methods used with metals and polymers cannot usually be applied to ceramics because of their brittle nature[1].

Injection molding is a forming process originally designed for polymers that has been successfully adapted to ceramics. It is possible to incorporate fine ceramic powders into polymer binder systems such that the resulting compound can be processed by plastic injection molding. This type of technique is particularly attractive for those applications requiring production of complex of high dimensional accuracy, high strength and uniformity, low scrap rates, and low cost. In addition, injection molding offers the possibility of automated production at high rates. There are five stages involved in the fabrication of injection molded ceramic components [2]:

1. Compounding, which involves the mixing of a ceramic powder with an organic vehicle to confer sufficient fluidity to fill the mold under available machine pressures.
2. Injection in the mold cavity.
3. Removal of the organic vehicle.
4. Sintering of the body to near full density.
5. Machining.

It is often the binder removal stage that introduces defects and dimensional irregularities in the component. Certain applications of ceramics, such in optics, require the

production of very high dimensionally accurate parts and high production rates. It is often necessary to apply extensive machining because of the defects introduced during the binder removal stage. This drastically increases production costs making the whole process unfitted for such applications. Optimizing the binder removal process to reduce or eliminate defects and distortions is, therefore, essential in ensuring the applicability of this otherwise powerful processing technique.

1.2 BINDER SYSTEMS

1.2.1 FUNCTIONS

Binders or flocculants are essential for the processing of many commercial ceramics because they provide green strength and plasticity to ceramic powders so that bodies can be molded and maintain the desired shape before firing [3]. Their functions are varied and range from wetting agents to thickening agents [4]. Table 1.1 shows some of the most common binder functions [5, 6].

The selection of the polymeric additive(s) for a specific ceramic process depends in part on the rheological characteristics of the polymer-powder system. The rheology is influenced by the flexibility of the polymer molecules and by the amount of polymer in solution. For example, vinyl- and acrylic-based binders have flexible backbones, while carbohydrate-derived binders are rather inflexible because of their connected ring structure. Polymer additives enhance the strength of green bodies by binding the ceramic particles together. Their binding action results from either the physical wetting of the particle surfaces or the chemical adsorption of organic functional groups onto the particulate surfaces[6].

Table 1.1: Functions of organic additives in ceramic processing [5, 6].

Additive	Function
Polymer (binder)	Green strength
Plasticizer	Rheological aid
Dispersant	Steric dispersion
Solvent	Solvating other additives; rheological aid
Lubricant	Mold release; interparticle sliding
Wetting agent	Lowering surface tension of liquid
Water retention agent	Preventing squeezing-out of water during pressure applications
Antistatic agent	Charge control
Antifoaming agent	Preventing foam or strengthening desired foams
Chelating agent	Inactivating undesirable ions
Fungicides/Bactericides	Stabilizing against degradation with aging

Plasticizers adsorb on the polymer and reduce the secondary valence forces between polymer chains. The effects of platicization are increased segmental motion of the polymer molecules, increased free volume, reduced modulus or stiffness, and reduced glass transition temperature[6].

The binder system is proportioned to form a continuous matrix. The volume fraction of particles in the mix is usually kept below f_{cr}^{v}, the packing factor at which flow is blocked (Dougherty-Kreiger equation)[4].

1.2.2 BINDER REMOVAL

The polymer removal stage involves the extraction of typically 30-40vol.% of vehicle. Five polymer removal techniques can be identified[7]:

1. Thermal degradation of the organic binder in an inert atmosphere.

2. Oxidative degradation.
3. Capillary flow into a finer powder or a porous substrate (wicking).
4. Evaporation.
5. Solvent extraction.

This thesis is mostly concern with capillary flow into a porous medium and thermal degradation.

1.2.2.1 Thermal degradation

This the most widely used technique. It involves a very slow heating rate and this leads to very long cycle times which can be several weeks for complex shapes. Initially, the green body can be heated to its softening point fairly rapidly whereupon the vehicle becomes fluid. Subsequently extremely slow heating rate is required at the early stages of decomposition. Vacuum or inert gas atmospheres are preferred during polymer removal[7]. Polymers undergo a variety of degradation phenomena during thermolysis, including depolymerization, random scission, side group elimination, and cyclization. These degradation processes can be complicated by cross-linking reactions or by side reactions with ceramic surfaces, both of which lead to the formation of residual carbon[6]. The degradation process can be divided into three different stages associated with different amounts of binder loss:

1. The first weight loss (10% to 20% organics) below 200°C is associated with vaporization of absorbed water, residual solvent or mineral oil.
2. Rapid binder loss (40% to 70% organics) occurs from 200-350°C, and it is caused by polymer decomposition. This is the stage at which bubble formation, and spalling can occur.
3. The final weight loss (10% to 20% organics) is believed to be due to the oxidation of the carbon residue formed by the decomposition of the binder[3].

1.2.2.2 Binder wicking

Binder wicking and thermal degradation are closely related. Usually, green bodies are heat treated on a porous substrate or embedded in a fine powder[7,8,9]. The binder is removed through capillary suction which is inversely proportional to the size of the pores in the substrate or powder bed. The process starts early on during the thermolysis cycle, as soon as liquefaction of the binder takes place. Small changes in processing variables in melt wicking exert great influence on the resulting debinding rate. For example, green bodies with larger particle size require less time for debinding than bodies with smaller particle size. Debinding rates decrease with increasing amount of binder loss because of the decrease in the combined average permeability of the sample and wick when more of the binder is in the low permeability wick[8]. The procedure of embedding the article in a fine powder gives the advantage of offering structural support, thus reducing the amount of slumping in the green body. Unfortunately, embedding in powder is not a feasible option for very small articles and high production volumes.

1.3 MASS TRANSFER

The process of binder removal involves the transfer of binder through porous media. The binder components are driven to migrate by capillary forces. The capillary suction pressure in the setter is higher than in the green body. Processes in which binder loadings are high (15-50vol%), such as injection molding, lead to green samples referred to as 'closed-pore' compacts because the void space is nearly or completely filled with binder. Binder removal is particularly difficult in these cases because there is an initial absence of connected pore space. Injection molding techniques often use binder systems that are the result of combinations of several polymers and plasticizers. Analysis of the mass transfer process, in these cases, is even more difficult since different transport processes take place contemporarily[6]. This thesis is, however, primarily interested in the mass transfer of liquefied binder through a porous medium. Mass transfer of volatile components will be briefly discussed in Chapter 3.

The equation governing fluid motion through a porous medium is known as Darcy's Law. This equation relates binder flux to the specific physical, mechanical, and geometrical characteristics of the fluid/porous medium system such as the permeability of the porous matrix, the surface tension (the wetting properties) and the viscosity of the binder. This law can be adjusted to different levels of saturation in the green sample through the permeability of the porous medium. It was mentioned earlier that permeability and binder content are closely related[10].

1.4 CREEP

Liquefaction of the binder medium causes loss of structural support and slumping, sagging, of the green body. The mechanics of deformation of the sample are analogous to those encountered in creep. Creep is a slow, continuous deformation of a material under constant stress. Creep can be generally described in terms of three different stages: primary creep (in which creep proceeds at an increasing rate), secondary creep (steady state), and tertiary creep (in which creep proceeds at a decreasing rate)[11]. Creep is a complex process involving several mechanisms ranging from diffusion to dislocation slip[12]. However, the applications analyzed in this thesis all assume the immediate onset of steady state creep. This assumption, which is backed by experimental evidence, greatly simplifies the problem of calculating deformation rates by using slightly modified versions of the elastic stress/strain equations (Hooke's law). Unfortunately, even with this assumption, modeling of creep is still a difficult task because of geometrical complexities. Finite element modeling is a convenient method for converting the spatial components of complex sets of continuous partial differential equations to a set of discrete nodal equations for numerical solving. The spatial area of interest is gridded into small patches called finite elements over which the variables are represented by simple polynomials. A solution can be found within any preset error limit[13,14] if a sufficiently fine grid and a sufficiently high power polynomial are used.

[1] Theilgaard, Naseem, "Injection moulding of technical ceramics," Technological Institute, Gregersensvej, 1989.

[2] Edirisinghe, M., J., Evans, J., R., G., "Review: Fabrication of engineering ceramics by injection molding. I. Materials Selection," Int. J. High Tech. Ceramics, **2** (1986) 1-31.

[3] Dong, C., "Binder removal in ceramics," Ph.D. Thesis, Dept. Mat. Sci. Eng., MIT, Cambridge, MA (1990).

[4] Reed, J., S., "Introduction to the principles of ceramic processing," John Wiley & Sons, New York, 1988.

[5] Pincus, A., G., Shipley, L., E., "The role of organic binders in ceramic processing," Ceram. Ind., **92** [4] 106-109 (1969).

[6] Lewis, J. A., "Binder distribution processes in ceramic green tapes during thermolysis," Ph.D. Thesis, Dept. Mat. Sci. Eng., MIT, Cambridge, MA (1990).

[7] Edirisinghe, M., J., Evans, J., R., G., "Review: Fabrication of engineering ceramics by injection molding. II. Techniques," Int. J. High Tech. Ceramics **2** (1986) 249-278.

[8] Patterson, B., R., Aria, C., S., "Debinding injection molded materials by melt wicking," Research Summary.

[9] Edirisinghe, M., J., "Removal of organic binder from moulded ceramic bodies," "Fabrication Technology," Institute of ceramics, Shelton, UK, 1990.

[10] Bear, J., "Dynamics of fluids in porous media," Dover Publications Inc., New York, 1988.

[11] Findley, W., N., Lai, J., S., Onaran, K., "Creep and relaxation of nonlinear viscoelastic materials," North-Holland Publishing Co., New York, 1976.

[12] Gittus, J., Creep, viscoelasticity and creep fracture in solids, John Wiley & Sons, New York, 1975.

[13] Gunnar, B., "Fields of physics on the PC by finite element analysis," Studentlitteratur, Lund Sweden, 1994.

[14] "PDEase2® Release Notes," SPDE Inc., Bass Lake, CA, 1995.

2. MONITORITNG OF SAMPLE DISTORTIONS DURING HEAT TREATMENT

2.1 INTRODUCTION

The onset of deformation during the binder removal cycle of injection molded ceramic components is one of the factors limiting a wider commercial application of this type of processing technology. Distortions and slumping occurring during the thermal degradation cycle have been examined in the past. Injection molded components are designed to flow at elevated temperature so that the polymer-binder mix can fill the die. This characteristic poses a problem during heat treatment, since conditions are created that allow the mixture to flow once again. Components, therefore, tend to deform under their own weight and slump. Slumping, however, is not the only type of distortion affecting injection molded samples. Ceramics and polymers have low coefficients of thermal conductivity. It is not unusual for temperature gradients to be created within the component during heat treatment. This represents a problem since polymers experience large volume changes during the transition from solid to liquid. Different levels of melting can be created within the sample, with consequent formation of internal stresses that are released through distortion of the component. Internal stresses can be created during the demolding process following injection and cooling. Relaxation of these stresses can also be responsible for the onset of distortion. This type of distortion, together with that created by uneven melting, can be analyzed with in-situ measurement techniques.

Dimensional instabilities in injection molded components generally depend strongly upon heating rate during the binder thermal degradation cycle. These deformations are more pronounced as heating rates are increased[1,2]. Quackenbush *et al.* heated articles at 10°C/hr. up to the melting point of the binder and then decreased the heating rate 2°C/hr. at higher temperatures[3]. The results showed that the deformations were somehow related to the release of the binder and the products of degradation from

the injection molded part. Cima and Dong conducted a detailed analysis of bubble formation in components containing different amounts and types of organic vehicles. Their work showed that initial bubbles of trapped gas can shrink or disappear as temperature increases. However, undisappeared initial gas and solvent bubbles can act as natural nucleation sites for formation of decomposed polymer gas pockets. They also noticed that bubble density increases as heating rate increases and that bubble-nucleation and bubble-shrinkage temperatures increase as heating rate increases. Theoretical and experimental studies were made on the effect of pressure fluctuations on binder removal and carbon residue inside fired samples[4].

The studies presented in this chapter focused on the early stages of binder removal. The chapter is divided in two sections. The first section describes a series of experiments designed to detect the exact onset of deformation in the injection molded samples. The second part describes experiments that were designed to characterize the type of deformation occurring in the samples (slumping, bubble formation, etc.).

2.2 ONSET OF DIMENSIONAL INSTABILITIES

2.2.1 INTRODUCTION

Binder removal is believed to contribute significantly to the formation of defects (such as bubbles and blisters) and to the distortion of the ceramic component. The control of the binder burnout cycle is critical in preventing these types of defects, especially when considering the large amount of organic vehicle contained in the green body (30 to 60% binder loadings on a volume basis are typically used for injection molding). The actual time of onset of deformation, however, is not known. The experiments described in this section were designed to determine the actual time of onset of dimensional instabilities in injection molded samples.

Figure 2.1 shows the type of sample used in this project. The samples were provided by an outside vendor which produced them according to a design developed by Prof. Michael Cima and 3M Corp. The shape of the samples was chosen for two reasons: on one hand the part resembles the shape of actual components of interest; on the other hand, it offers numerous reference points that will facilitate performing cross-sectional measurements. The notch at the bottom of the sample had a slight taper to facilitate mold release.

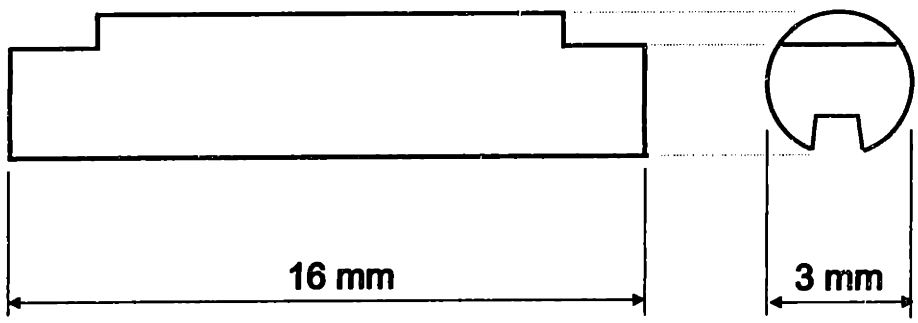

Figure 2.1: Typical injection molded sample with major dimensions.

Two types of samples were delivered. One type of sample had a wax based proprietary binder sytem composition characterized by low viscosity. These samples were referred to as Low Viscosity System Samples (LV system). The binder of the second type of sample was designed by Prof. Cima. These samples had the following composition in percent by volume: 27% reed wax 89100, 13.5% polyethylene (Aldrich Catalogue # 19,191-4), 13.5% stearic acid and 46% zirconia powder. The polyethylene component acts as a rheological aid which increases the viscosity of the binder mixture. The zirconia powder was tested at the 3M premises with a particle analyzer (Microtrac-X100 Particle Analyzer) and the results showed a primary particle size of less than 1.35μm. These samples had higher viscosity than the LV system samples. They were referred to as High Viscosity System Samples (HV system).

Measurement of deformation at low temperatures during heat treatment required the construction of a special furnace shown in Figure 2.2. The body of the furnace consisted of a 4ft. long Pyrex tube with an internal diameter of 2 in. Two different types of heating elements were mounted. The exterior walls of the Pyrex tube were heated with two cylindrical heating elements connected to an Omega controller (Omega Engineering Inc., Stamford, CT 06907-9987). The interior of the furnace was heated with a coiled resistance connected to a separate Omega controller as well. This heating element was also used to increase the temperature of the incoming flow of pre-purified nitrogen. The whole set-up was wrapped with insulating material. Actual measurements were made with a Point Range Sensor (PRS-15, CyberOptics Corporation, 2505 Kennedy Street NE, Minneapolis, Minnesota 55413). The sensor used laser triangulation to measure variations in distance. The sensor is not affected by surface smoothness because it refocuses a scattered return signal onto a detector. This method allowed a resolution of 0.38 μm (actual resolution obtained in the experiments were lower due to background noise created by the electrical components in the furnace and the nitrogen flow). A slit, 1.5 in. long and perpendicular to the axis of the furnace, was cut on the

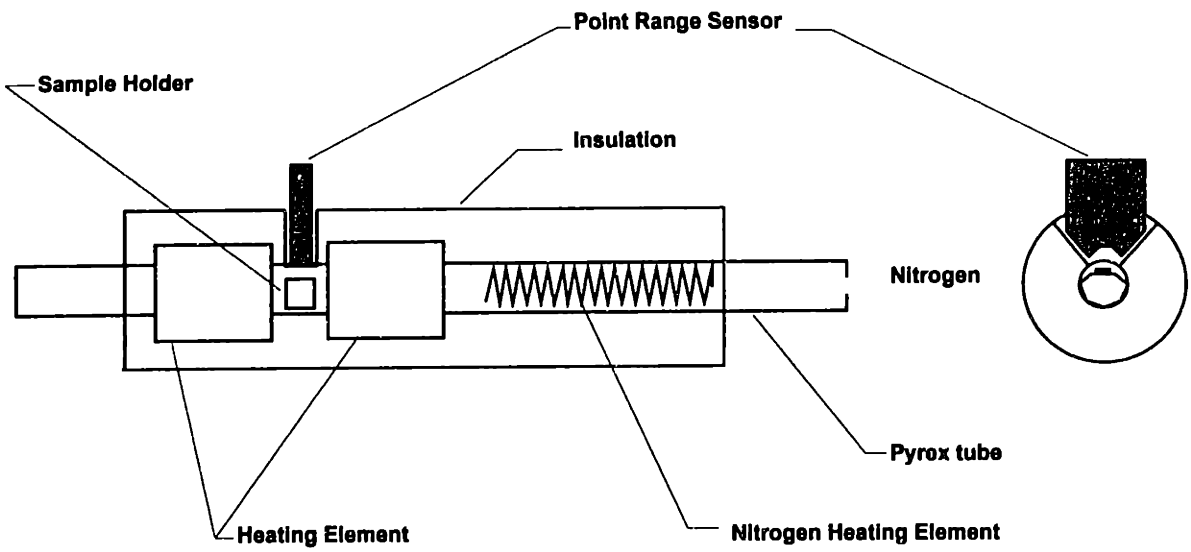

Figure 2.2: Experimental set-up used to perform in situ distortion measurements.

Pyrex tube to prevent diffraction effects from influencing measurements. The laser was located on top of the slit through a window obtained from the insulation material. Two type K thermocouples were used to monitor temperature (Omega Engineering Inc.). One thermocouple was placed directly below the slit in the Pyrex tube, the second one, at the same height as the sample.

2.2.3 Experimental Procedure

The first set of experiments was performed to determine the exact onset of deformations during heat treatment for both type of samples. Typically the green injection molded sample was weighed prior to heat treatment and placed on a non-porous setter. A flat rectangular fragment of high density alumina was placed on the setter, next to the sample. This alumina part was used as a reference point during heat treatment. The Point Range Sensor was used to measure an initial profile of the sample surface and to measure the distance to the alumina reference sample. The sensor was placed on one of the two flat surfaces on the upper part of the injection molded sample (visible in Figure 2.2) and the distance measured and recorded. A continuous flow of pre-purified nitrogen was maintained inside the furnace throughout the experiment (nitrogen flow rate: 5 SCFH). Both types of heating elements were then activated and controlled to maintain a steady temperature raise, the rate of which was varied in several experiments. The distance to the flat surface on the sample was recorded every time the temperature increased by 2°C. This procedure was followed up to when the target temperature (which varied with each experiment) was reached. This temperature never exceeded 100°C for two reasons. First, preliminary experiments performed on similar types of samples showed that major distortions occurred at relatively low temperatures (50-60°C). Second, the laser could not be exposed to higher temperatures to prevent risk of malfunction or distortion of the laser case. A second full profile of the sample surface was taken and the distance to the reference point measured again when the final temperature was reached. The furnace was then shut off, and, while keeping a constant

nitrogen flow, cooled down to room temperature. The distance to the top flat surface of the sample was measured every 2°C during this time. A final surface profile of the sample was taken as well as an ulterior measurement of the reference point when room temperature was reached. Final weight of the sample was recorded.

The data obtained with this experiments were plotted in two different types of graphs. One plot showed variation in height of the sample top flat surface vs. temperature, including the relative distances to the reference point. The second type of plot showed all three complete surface profiles adjusted for variations in the height of the reference point. Thus real relative variations in profile height were obtained independently of thermal distortions of the furnace.

2.2.4 Results and Discussion

Figure 2.3 shows the typical behavior of a LV sample treated to a temperature of 62° C at a rate of 1°C./min. The plot also shows the location of the reference point relative to the laser sensor. The sample height difference between the heating and cooling times is evident. It is also shown that this height difference is not attributable to a thermal deformation of the furnace, since the initial and final reference points show very small changes in height. The sample clearly slumped rapidly at approximately 57° C. The sample lost more than 100μm in height during this process. The slumping of the sample suggests the loss of structural support from the binder. This can be explained by a phase transformation of the binder mix from solid to liquid. The binder was strong enough to support its own weight and the weight of the ceramic powder below the melting temperature. The binder became unable to support the weight of the sample upon liquefaction. Slumping and distortion of the sample followed as a consequence. Figure 2.4 shows the cross-sections of a typical sample before and after annealing. The sample in (b) rested on a non porous flat surface: the lack of structural support either from the binder or an external structure resulted in the collapse of the sample. These two

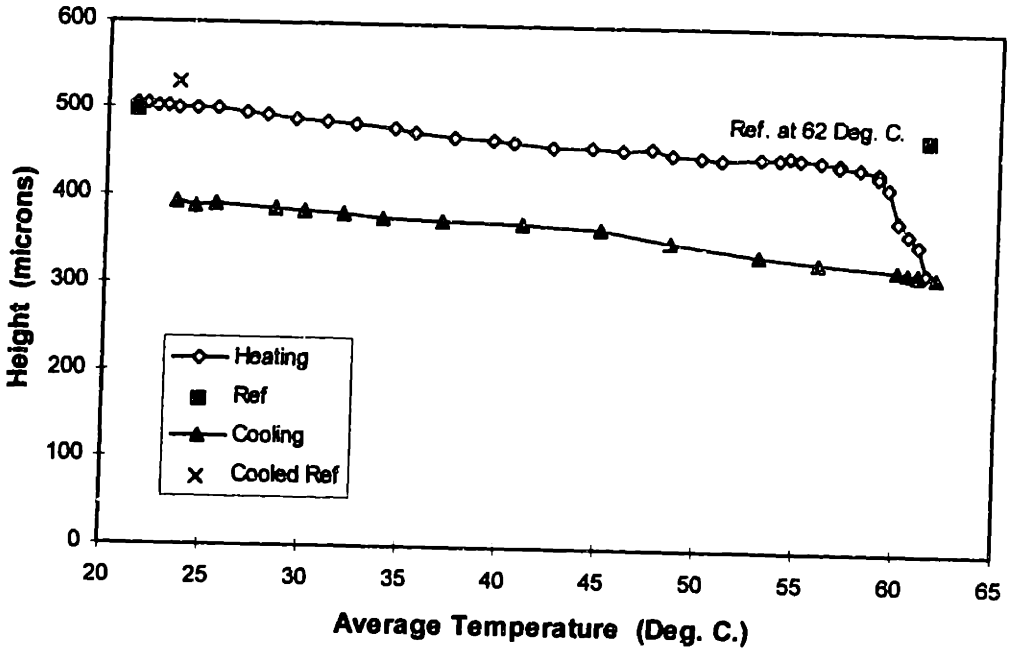

Figure 2.3: Sample distortion vs. temperature (LV System, 62°C).

pictures are not to scale, but Figure 2.5 allows one to appreciate the magnitude of the actual deformation by showing the height of the sample profile during and after heat treatment. These types of deformations, together with the low heating temperature, suggest that no major binder loss did occur. This was confirmed once final weights were compared to the initial sample weights. Results showed that binder loss was minimal in all of the experiments, peaking at a value of 1.5% for specimens treated at 100°C.

Normally, in industry, components are not heat treated on flat surfaces. It is common practice to lay the injection molded components into special "setters" the shape of which is designed to offer better support to the parts, and guarantee specified spacing between components. Figure 2.6 shows the height variation of a sample that had been placed in a v-grooved setter. This type of geometry offered improved support and this is shown but the reduced magnitude of the deflections. These values are, however, still well beyond acceptable quality levels.

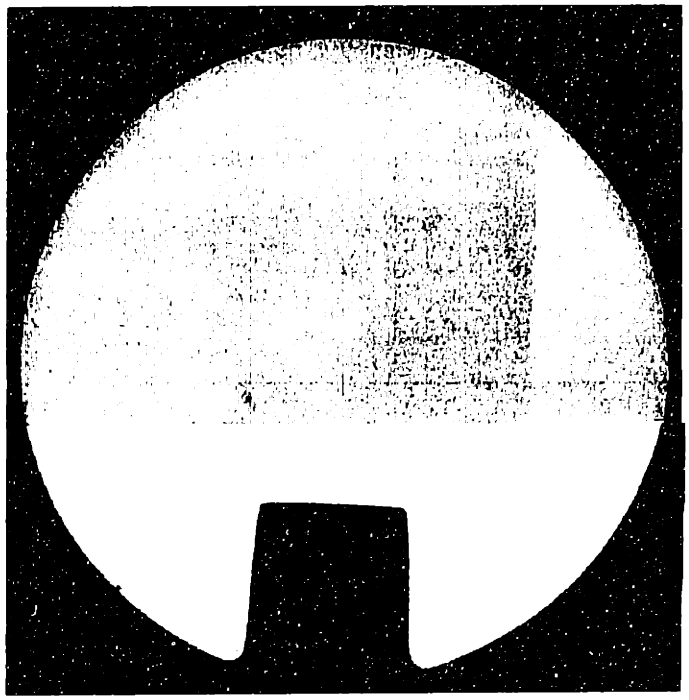

(a)

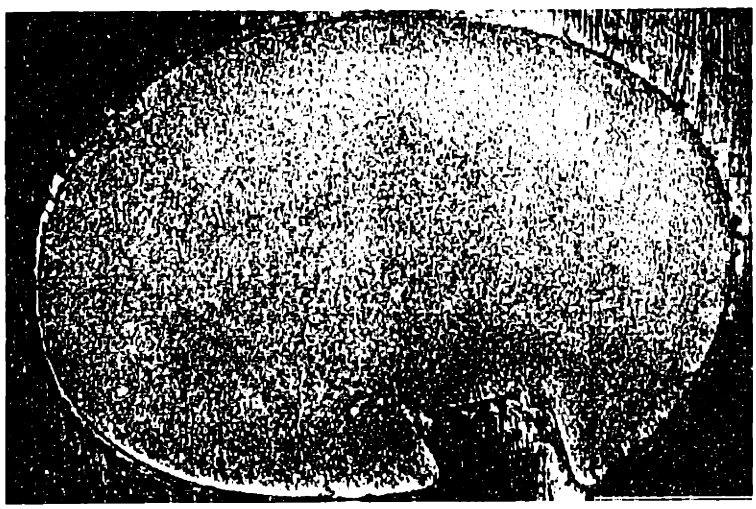

(b)

Figure 2.4: Sample cross-sections; (a) before heat treatment, (b) after heat treatment.

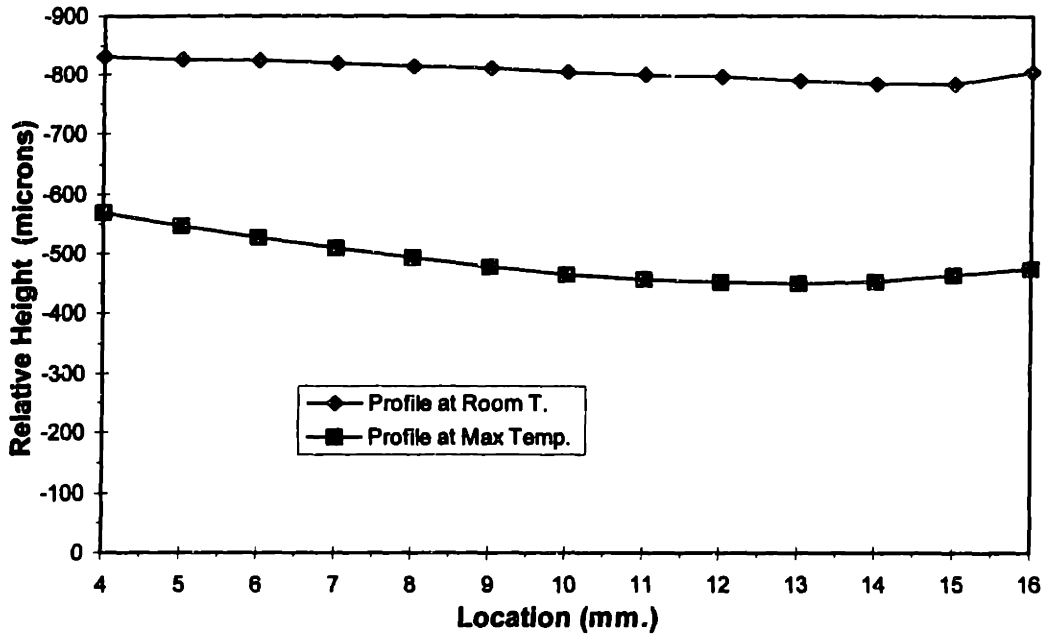

Figure 2.5: Sample profile during and after heat treatment.

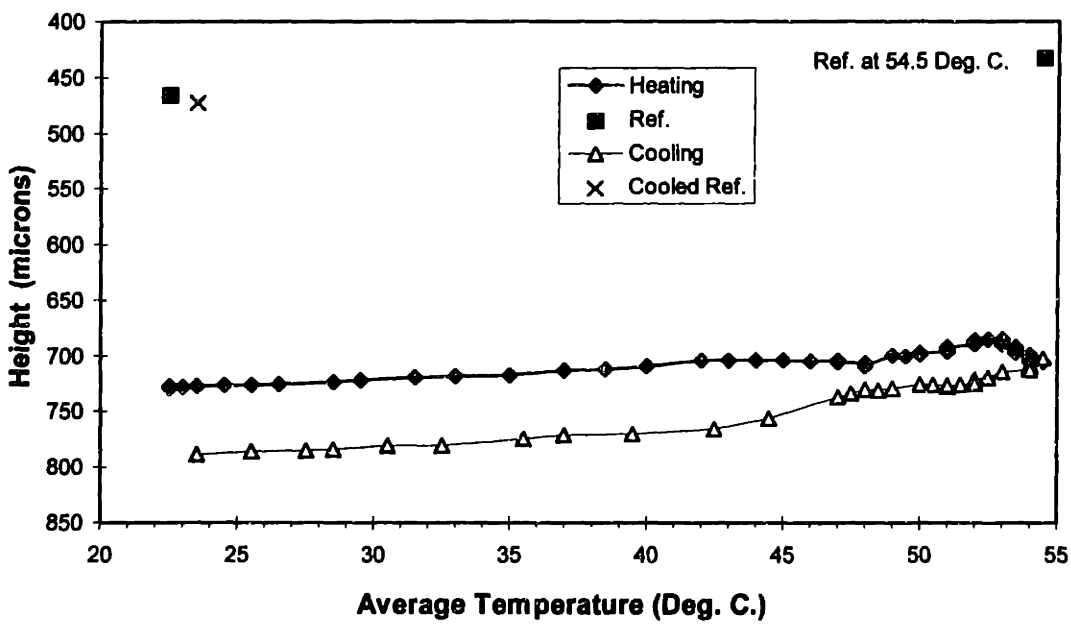

Figure 2.6: Sample distortion vs. temperature for an article resting on a v-grooved setter (LV system).

The strengthening effect of the polyethylene was demonstrated by the same experiment performed with the HV system sample.

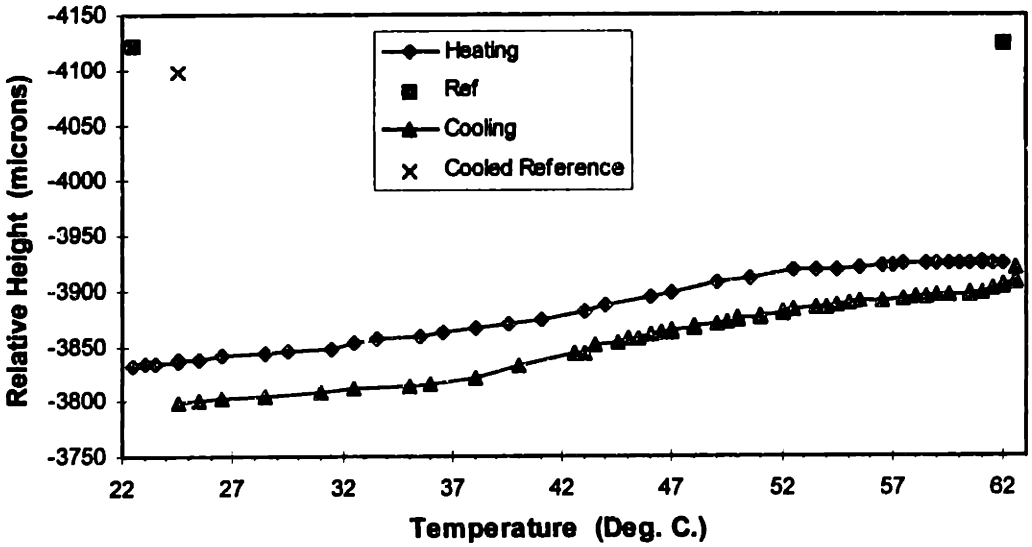

Figure 2.7: Sample distortion vs. temperature (62°C - HV system).

The strengthening effect is shown in Figure 2.7 by the reduced size of the sample deformation during heat treatment. The differences in sample heights were, in fact, comparable to the difference in height of the reference point before and after heat treatment. This means that the difference in height can be mostly attributed to the deformation occurring in the furnace due to thermal expansion phenomena. The LV system samples showed deformation that could be mostly attributed to slumping.

Figure 2.8 shows the effect of thermal expansion measured in HV samples during heat treatment. This is due to the change in volume associated wit the glass transition temperature of polyethylene. The specific volume of polyethylene varies from 1.172-1.176 in the amorphous state to 1.060-1.073 in the crystalline state[1]. These values can be used to calculated the volume change of the sample through the glass transition temperature. The volume of the sample varies from 113.1mm^3 in the crystalline state, to

125.5mm^3 in the amorphous state (using dimensions shown in Figure 2.1). This volume change corresponds to a diameter change of .105mm or 105μm. This change in diameter corresponds to the difference in heights of the sample at high and low temperatures shown in Figure 2.8.

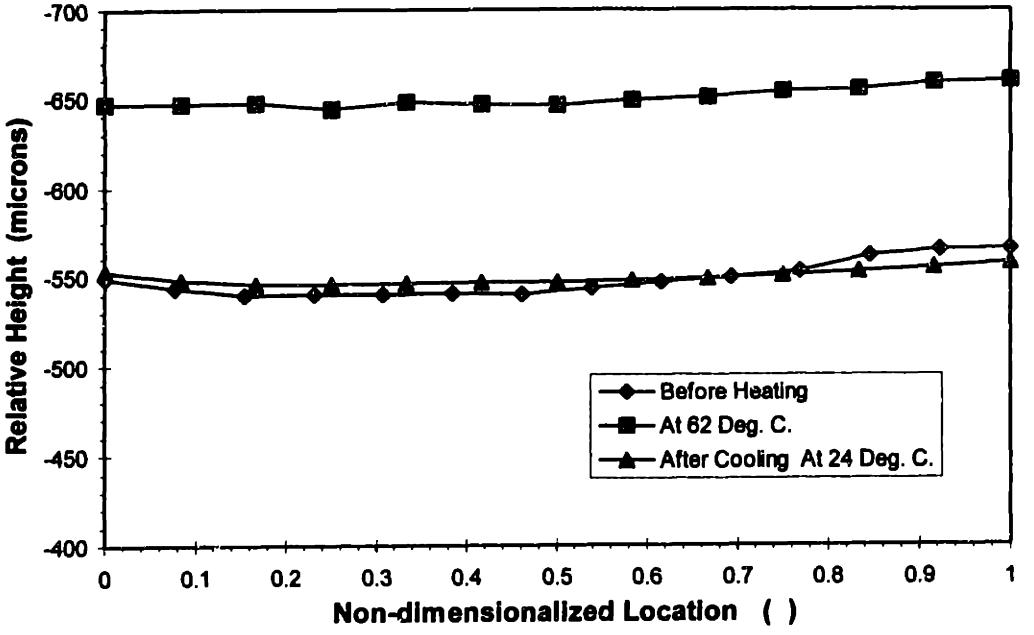

Figure 2.8: Sample profile before, during, and after heat treatment (HV System)

This plot also shows that the high deformations due to the volume changes in polyethylene are reversible and do not create significant permanent deformation in the sample.

2.2.5 CONCLUSIONS

This set of experiments gave useful insight in the onset and modality of sample deformation occurring during heat treatment. It was shown that the slumping of the article due to loss of structural support from the liquefied binder represented the major contributor to the dimensional instability of the injection molded parts. These deformations occurred quite rapidly immediately after reaching the melting temperature

of the major binder component. The presence of polyethylene greatly reduced the amplitude of the deformation by increasing binder viscosity. The geometry of the setter also played an important role. It was shown that setters offering lateral support for the sample contributed to reducing the overall magnitude of the deformations, even though, these were still intolerable for practical applications.

2.3 SURFACE PROFILES OF SPECIMENS UNDERGOING DIFFERENT DEGREES OF HEAT TREATMENT

2.3.1 INTRODUCTION

Binder liquefaction and consequent slumping of the injection molded ceramic article has already been determined to be a conspicuous contributors to the onset of dimensional instabilities. The role of other phenomena that could lead to deformations, however, has not been determined at this time. It is necessary to investigate other possible causes leading to sample deformation and relate them to specific processing conditions.

Some of the defects that can be expected during binder burnout are due to excessive vapor pressure generated by binder decomposition. The kind of defect existing in the final article depends on the plasticity of the compact structure and the stage of the binder removal process[4]. Bubbles, blisters, and pores are more likely to occur in plastic structures because theses are likely to yield in a non-catastrophic manner. Cracks or explosive spalling are likely to occur in rigid structures. Bubble formation is extremely important in determining the final quality of ceramic articles. The size and extent of the bubbles can be primarily related to the heating rate as well as the polymeric content of the article. Polymers decompose during heat treatment into monomers which diffuse towards the liquid/vapor interface. The rate of generation of these volatile products is primarily determined by the rate at which heat is applied to the article. The liquid

polymer may be supersaturated with the instantaneously decomposed monomer when a critical heating rate is exceeded. The volatile components may not have time to diffuse to the liquid/vapor interface, and bubble formation may occur.

Non-uniform binder melting due to temperature gradients within the sample are also an important source of deformation. This type of deformation is likely to occur in injection molded ceramic components because both, binder and ceramic components are poor thermal conductors. The experiments described below were designed to determine whether sample deformations can be significantly related to phenomena such as uneven binder liquefaction and blister formation.

2.3.2 Experimental Procedure

The higher temperatures necessary to obtain complete binder burnout did not allow the use of the Point Range Sensor to directly monitor distortions during heat treatment. These experiments were performed using a Lindberg furnace type 54352 with a maximum temperature limit of 1200°C (Lindberg, 304 Hart St., Watertown, Wis. 53094). The furnace was programmed with an Omega controller analogous to the one mentioned earlier. A source of pre-purified nitrogen was also connected to the furnace. A type K thermocouple was used to monitor temperatures.

Typically 4 to 5 samples were used for run in this type of experiment. Each one of the samples was weighed prior to heat treatment and then placed on a porous setter in which a 90° v-groove had been carved in a milling machine. The setters were fabricated from alumina/silica insulating boards obtained from an outside company (ZAL 45 and ZAL 15, Zircar Products Inc., Florida, New York 10921). The table below shows the primary characteristics of the board. Porosimetry tests (Autopore II 9220, Micrometrics, Norcross, GA 30093) performed on the setter material ZAL 45 had an average pore size of 8 μm., while ZAL 15 had an average pore size of 17 μm. Table 2.1 shows characteristics of the setters.

Table 2.1: Characteristics of the insulating board used to fabricate setters.

Composition (wt%)	ZAL 45	ZAL 45
Al_2O_3	85	85
SiO_2	15	15
Organic	0	0
Density gm/cm^3	0.24	0.72
Porosity (%)	93	70

Samples where heat treated to a final temperature of 450°C, which allows for complete binder removal as determined in preliminary experiments by comparing initial and final weights of samples fired at several temperatures. The original profiles of the samples were measured using the Point Range Sensor. The samples were placed in the Lindberg furnace which was then sealed and filled with pre-purified nitrogen (2-4 SCFH). The furnace was started and controlled to operate with a heating rate of .5 or 2°C/min. depending on the experiment. Samples were removed from the furnace when predetermined target temperatures between room temperature and 450°C were reached (usually 50, 150, 250, 350, and 450°C). The sample profiles were remeasured with the Point Range Sensor and their final weights recorded after complete cooling to room temperature. The heat treated samples, together with a green sample were embedded in epoxy (Epo-Kwick, Buehler LTD., Lake Bluff, IL 60044). The samples could then be cut (Isomet Low Speed Saw, Buehler LTD) and polished (Ecomet IV, Buehler LTD) to measure their cross-sectional dimensions using a measuring microscope. The recorded profiles were plotted as a function of temperature and so were the cross-sectional dimensions of the samples.

2.3.3 RESULTS AND DISCUSSION

Figure 2.9 shows typical sample profiles after heat treatment at different heating rates. The profile of a sample at room temperature is also shown for comparison purposes.

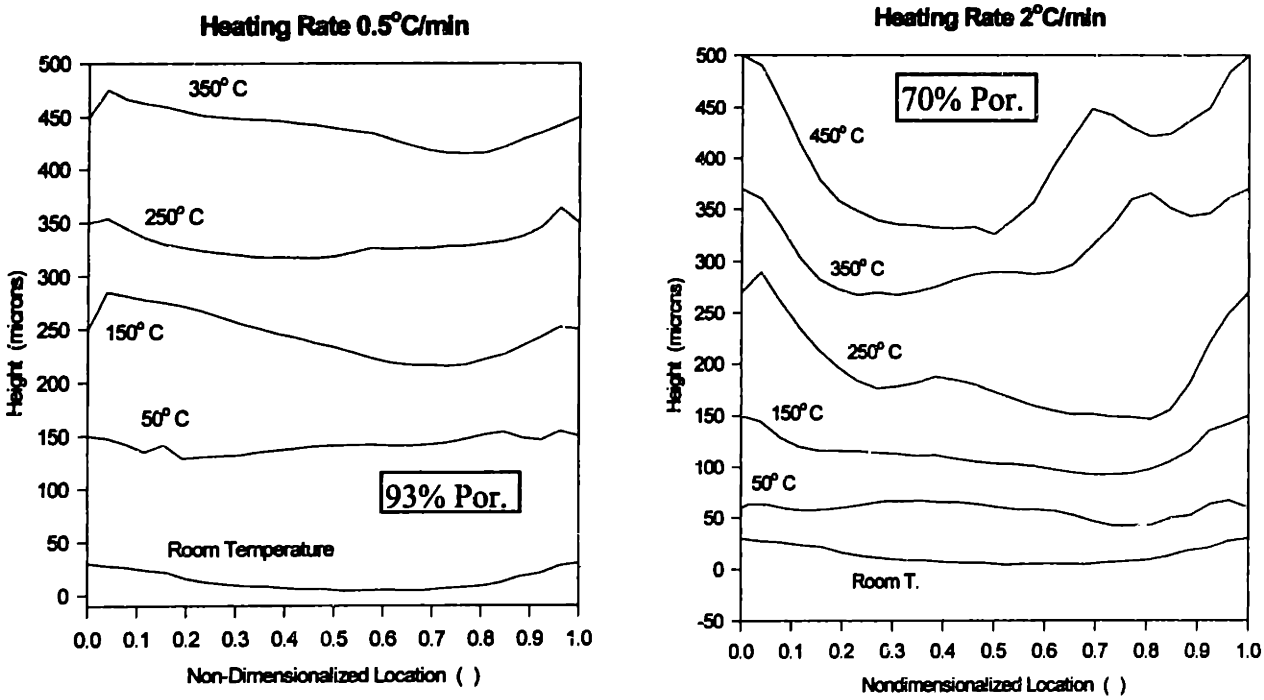

Figure 2.9: Sample profiles as a function of temperature for two different heating rates (LV System).

The degree of distortion of the sample was, in both cases, excessive and well beyond the tolerances required for optical applications. There is, however, considerable difference in the magnitude of the distortions depending on heating rate. The distortions of the sample treated at high heating rates were more pronounced than at low ramp rates. One of the factors causing deformation of the sample was bubble and blister formation. The liquid polymer is supersaturated with the instantaneously decomposed monomer when a critical heating rate is exceeded. The volatile components do not have time to diffuse to the

liquid/vapor interface, and bubble formation occurs. This type of distortion was reported by Cima and Dong[4] in ceramic tapes. Volatilized binder diffusing from the interior of the green body was prevented from creating bubbles by longer heating times. Two gas pockets are visible in the profiles of samples heated to 350 and 450°C at 2°C/min, while no bubbles were reported in the sample heat treated at 0.5°C/min.

The profile deformation patterns for these samples, however, besides blister formation at high heating rates, show that the principal cause of article distortion was indeed slumping. This is particularly true for the samples heat treated at a rate of 0.5°C/min. These samples are most interesting since this is a heating rate more likely to be used in industry.

Figure 2.10 shows dimensional changes in the heat treated samples as a function of temperature (LV - system, 70% Porous setters).

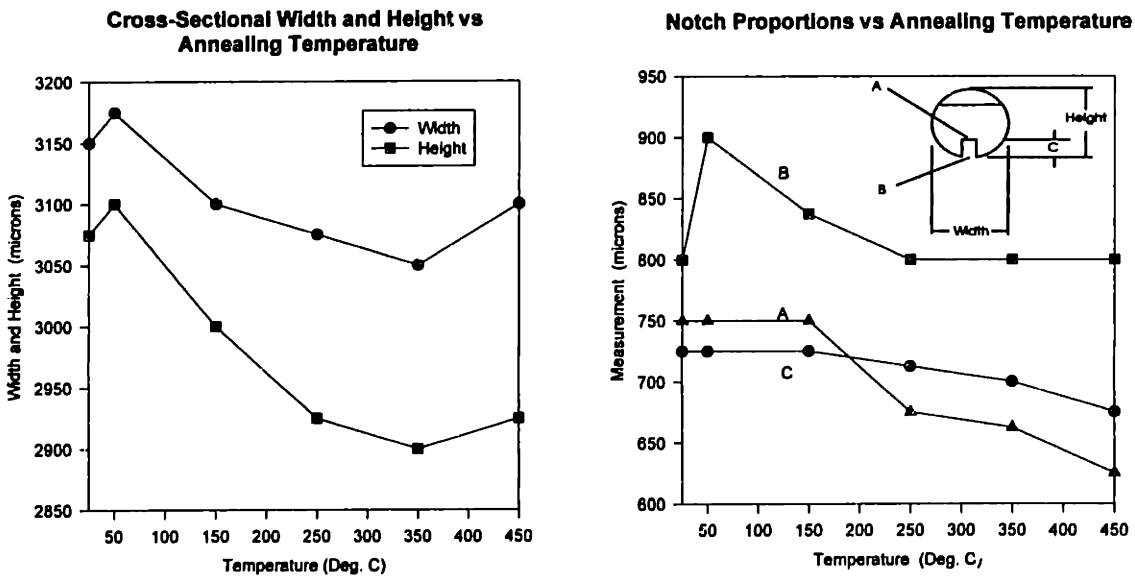

Figure 2.10: Characteristic sample dimensions vs. temperature (LV system - 70% Porous setters).

These dimensional changes show that the sample is undergoing two types of deformations: slumping due to loss of structural support, and shrinkage due to binder removal. Some dimensions, like the length of the bottom of the notch (dimension "B") show, at low temperatures, an increase that can be attributed to the loss of structural support and collapsing of the part. The next chapter will deal in greater detail with deformations due to creep effects. Spreading of the notch is found only in samples heat treated over non-porous setters, as discussed in the next chapter. Samples heat treated over porous setters, such as in the case above, showed shrinkage of the notch due to localize depletion of binder. The expansion of the notch shown in Figure 2.10 might seem in contrast with these results. This expansion was measured at a relatively low temperature and minimum binder removal took place before the sample was removed from the furnace. This explains why notch expansion instead of shrinkage, which is measured when large amounts of binder are removed, was not detected at 50°C. Measurements made at higher temperatures show the shrinking behavior. Further analysis of sample deformation will be discussed in the next chapter.

The HV system articles were also heat treated at several temperatures and their profiles measured. Figure 2.11 shows the results of heat treatment to 450°C at a rate of 0.5°C/min. on these samples.

The deformations measured in the HV system samples is much smaller than those measured in LV system samples. This can, once again, be explained by the higher viscosity of the binder system. This binder system flows at a much lower rate than the less viscous LV system. Deformation due to creep is, therefore, minimized. Other sources of deformation, like blisters, were not found for two reasons. The slow heating rate allowed the products of volatilization to migrate at the surface without becoming super saturated within the sample. The greater viscosity of the binder system is also more likely to contain eventual small bubbles formed within the sample without showing major deformation at the surface of the sample.

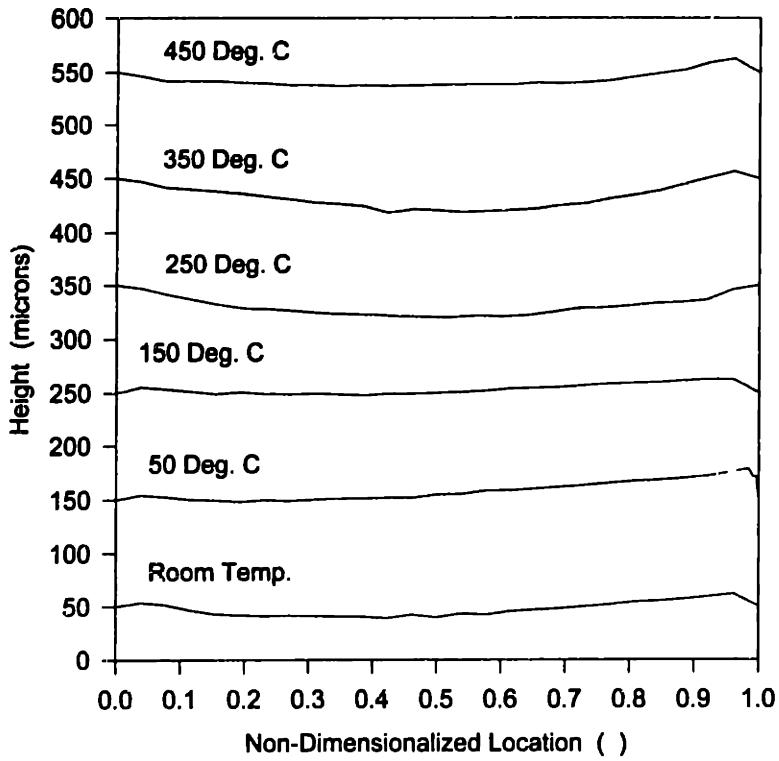

Figure 2.11: Sample profiles as a function of temperature (0.5°C/min. - HV system)

2.3.4 CONCLUSIONS

This set of experiments showed that sample deformations were closely related to heating rate since samples heated rapidly were more likely to show large distortions as well as experience bubble formation. HV samples deformed less than LV samples because of their higher viscosity. However, at low heating rates, slumping seemed to be the only source of deformation during the early stages of heat treatment. This does not mean, however, that other deformation mechanisms might have been taking place. In

particular, it is essential to study the influence of setter characteristics on the binder removal, wicking, of binder from the sample.

The experiments described in this chapter were only preliminary experiments leading to a more in depth study of the relationship existing between setter characteristics, sample/setter interface geometry, binder wicking, and sample distortions.

[1] Edirisinghe, M. J., Evans, J. R. G., "Fabrication of Engineering Ceramics by Injection Moulding. I. Materials Selection," Int. J. High Technology Ceramics, **2**, 1-31 (1986)

[2] Edirisinghe, M. J., Evans, J. R. G., "Fabrication of Engineering Ceramics by Injection Moulding. II. Techniques," Int. J. High Technology Ceramics, **2**, 249-278 (1986)

[3] Quackenbush, C. L., French, K. and Neil, J. T., "Fabrication of Sinterable Silicon Nitride by Injection Moulding," Ceram. Eng. Sci. Proc., **3**, 20-34 (1982)

[4] Dong, C., "Binder Removal in Ceramics," Ph.D. Thesis, Dept. Mat. Sci. Eng., MIT, Cambridge, MA (1990).

3. CREEP MODELING

3.1 FINITE ELEMENT MODELING OF SAMPLE DISTORTION

3.1.1 INTRODUCTION

The previous chapter was devoted to the analysis of the causes leading to sample distortion during heat treatment. This part of the research project was important in allowing the researchers focus on a specific issue. Slumping due to melting of the binder component was determined to be the most important contributor to distortion. Deformation is influenced by several factors, including heating rate and setter geometry. Optimization of these parameters to reduce overall deformation is usually an empirical process achieved mostly through trial and error rather than through scientific analysis. This is partly due to the fact that engineering tools allowing for prediction of component deformations during and after heat treatment have not received the deserved attention. Considerable information has been gathered regarding the effect of heating rate on part distortions[1,2]. However, little is known about the effect of setter geometry on these deformations.

This chapter focuses on the development of a model capable of predicting part deformation from relatively few parameters: article and setter geometry, burnout temperature, and thermo-mechanical characteristics of the ceramic/binder compound. The mechanics of creep and viscoelastic deformation will be discussed first. The analysis will then move to the derivation of the partial differential equations governing this phenomenon. Finally, the actual finite element tool used to solve the partial differential equations according to the related boundary conditions will be overviewed, together with sample cases.

3.1.2 CREEP OF VISCOELASTIC MATERIALS

Viscoelasticity is the generalization of elasticity and viscosity. The ideal elastic element is the spring. The elongation of the spring is proportional to the magnitude of the applied force. The ideal viscous element is a dashpot. The sides of a dashpot move apart at a rate proportional to the applied force[3]. Figure 3.1 shows both types of elements.

Figure 3.1: The elastic and viscous elements: spring and dashpot.

The equations relating elongation to applied force are different for these two elements. The displacement a for springs is related to a force F by Hooke's law:

$$F = Ea \tag{1}$$

where E is the modulus of the spring or modulus of elasticity. In a dashpot, an applied force is related to the elongation by the following:

$$F = \eta \frac{da}{dt} \tag{2}$$

where η is the viscosity of the dashpot.

Behavior of perfectly elastic materials can be described by equation 1 alone (adapted, obviously, to three dimensional geometries). Analogously, equation 2 can be used to describe perfectly viscous materials. Combinations of springs and dashpots can be used to describe viscoelastic materials and their creep behavior. Many of these models, (Maxwell, Voigt) are described in several references[3,4].

Creep is a slow continuous deformation of a material under constant stress. It can be described in terms of three different stages illustrated in Figure 3.2[5]. In the first stage, creep occurs at a decreasing rate (primary creep), in the second stage creep proceeds at a nearly constant rate (secondary or steady state creep), and in the third stage creep proceeds at an increasing rate till failure (tertiary creep)[5,6].

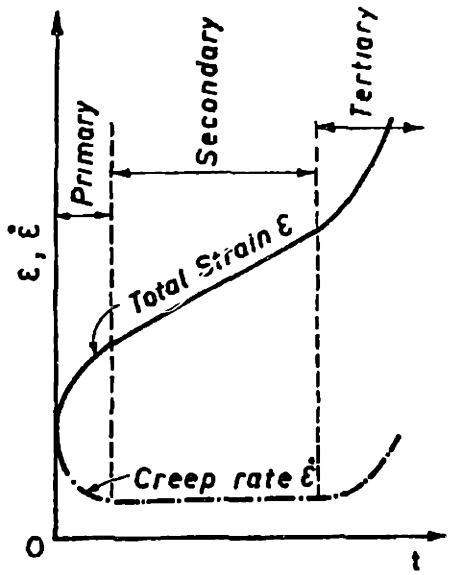

Figure 3.2: Three stages of creep[5].

These three stages of creep are governed by different deformation mechanisms which, in turn, lead to different models. We are mainly interested with linear steady state creep. A material is said to be linear viscoelastic if stress is proportional to strain at a given time, and a linear superposition principle holds. These linear requirements can be stated mathematically in two equations:

$$\mathcal{L}[c\,\sigma(t)] = c\,\mathcal{L}[\sigma(t)] \tag{3}$$

$$\mathcal{L}[\sigma_1(t) + \sigma_2(t-t_1)] = \mathcal{L}[\sigma_1(t)] + \mathcal{L}[\sigma_2(t-t_1)] \tag{4}$$

in which ε and σ are the strain output and the stress input, respectively, and c is a constant. Equation 3 states that the strain output due to a stress input $c\sigma(t)$ is equal to c times the strain output of $\sigma(t)$. Equation 4 states that the strain output of two arbitrary but different stress inputs applied at different times equals the sum of the strain outputs resulting from each of the two stress inputs acting separately[5].

Together with the linearity and steady state requirements, another assumption is going to be made about the specific creep behavior of the injection molded ceramic article. The creep behavior of the part is assumed to be dependent only on the viscous properties of the material and not on the elastic characteristics. This is equivalent to assuming that the article is flowing as a viscous liquid. It is known that the binder is, indeed, liquid, but, is it reasonable to assume that the whole article deforms as a liquid? Experiments described in Chapter 2, showed that part deformations were finite, that is, the component deformed but eventually reached equilibrium and creep ceased. The fact that viscous flows eventually ceases does not mean that elastic effects are important. Rather, it means that the viscous behavior is complex. Yield stresses might be important in determining the level of deformation of the part. Assuming that during deformation elastic effects are negligible is a reasonable approximation.

The plots that where studied in Chapter 2, showing sample distortion vs. time, also show that in early stages of the deformation cycle, distortions increase linearly with time. This means that deformations are occurring at a nearly constant rate, making the steady state assumption valid.

The basic mechanism controlling part deformation has been established. It is now possible to develop the equations that will enable us to quantify rates of deformation according to the material properties and geometrical architecture of the ceramic articles. The geometry of the setter/sample system dictates the boundary conditions necessary to solve the partial differential equations involved. It should be noted, one more time, that these equations are going to be based on the following assumptions:

1) Steady state creep.
2) Viscous flow-like behavior with no elastic effects.

3.1.3 DERIVATION OF PARTIAL DIFFERENTIAL EQUATIONS GOVERNING VISCOUS FLOW.

It has been assumed that the mechanical behavior of the injection molded article under gravitational forces is dominated by viscous forces and can, therefore, be modeled after equation 2. The substitution of a strain with a strain rate is what distinguishes equation 2 from equation 1. It is possible for simplicity, to use directly the equations governing elastic behavior and substitute the modulus of elasticity of the material with the viscosity in order to obtain the strain rate of the viscous flow. The equations of mechanical equilibrium for a volume element are shown below[7], and the corresponding coordinate system is shown in Figure 3.3.

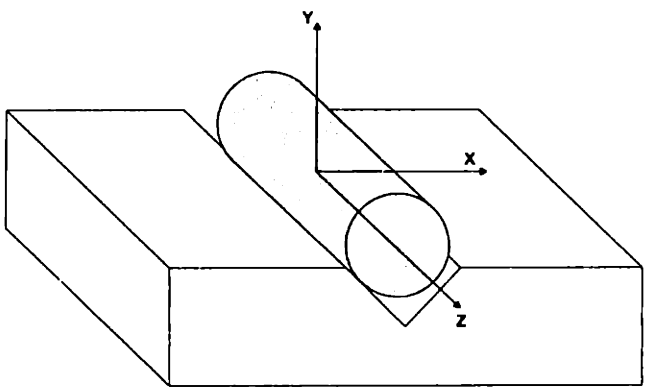

Figure 3.3: Typical sample/setter configuration with coordinate system.

$$\left\{\begin{array}{l} \dfrac{\partial \sigma_x}{\partial x}+\dfrac{\partial \tau_{xy}}{\partial y}+\dfrac{\partial \tau_{xz}}{\partial z}+F_x=0 \\ \dfrac{\partial \tau_{xy}}{\partial x}+\dfrac{\partial \sigma_y}{\partial y}+\dfrac{\partial \tau_{yz}}{\partial z}+F_y=0 \\ \dfrac{\partial \tau_{xz}}{\partial x}+\dfrac{\partial \tau_{yz}}{\partial y}+\dfrac{\partial \sigma_z}{\partial z}+F_z=0 \end{array}\right\} \qquad (5)$$

where σ are the normal and τ the shear components of stress associated with the three axes. The components of the external force F refer to unit volume. Gravitational forces are responsible for the deformation of the samples. Therefore only the F_y component will be considered. It is possible to rewrite Hooke's law in terms of strains obtaining

$$\begin{aligned}
\varepsilon_x &= \frac{1}{E}\left[\sigma_x - \mu(\sigma_y + \sigma_z)\right] \\
\varepsilon_y &= \frac{1}{E}\left[\sigma_y - \mu(\sigma_x + \sigma_z)\right] \\
\varepsilon_z &= \frac{1}{E}\left[\sigma_z - \mu(\sigma_x + \sigma_y)\right]
\end{aligned} \tag{6}$$

$$\begin{aligned}
\gamma_{xy} &= \frac{1}{G}\tau_{xy} \\
\gamma_{xz} &= \frac{1}{G}\tau_{xz} \\
\gamma_{yz} &= \frac{1}{G}\tau_{yz}
\end{aligned}$$

with $\frac{1}{G} = \frac{2(1+\mu)}{E}$,

where ε are the normal strain rate components, γ the shear strain rate components, and μ Poisson's ratio. Temperature effects have been neglected.

Note that in these equations the third dimension cannot simply be decoupled by "insulation"; stresses in the *xy* plane produce strain in the z-direction. Two assumptions lead to two different sets of equations. These assumptions regard the presence of stresses and strains in the z-direction. The plain strain assumptions is based on considering that no strain is developed in the z-direction. This means that strains form only in the xy plane, while stresses will form along all three axis[8]. This corresponds to the case in which the part is bonded to the substrate and unable to contract in the z-direction. With ε_z=0 equation (6) becomes

$$\begin{Bmatrix} \varepsilon_x \\ \varepsilon_y \\ 0 \end{Bmatrix} = \frac{1}{E}\begin{bmatrix} 1 & -\mu & -\mu \\ -\mu & 1 & -\mu \\ -\mu & -\mu & 1 \end{bmatrix}\begin{Bmatrix} \sigma_x \\ \sigma_y \\ \sigma_z \end{Bmatrix} \tag{7}$$

The plain stress assumption is based on considering that no stresses are developed in the z-direction while strains develop along all three axis. This corresponds to a perfect slip, no friction, condition at the sample/substrate interface. With $\sigma_z=0$, equation (6) becomes

$$\begin{Bmatrix} \varepsilon_x \\ \varepsilon_y \\ \varepsilon_z \end{Bmatrix} = \frac{1}{E}\begin{bmatrix} 1 & -\mu & -\mu \\ -\mu & 1 & -\mu \\ -\mu & -\mu & 1 \end{bmatrix}\begin{Bmatrix} \sigma_x \\ \sigma_y \\ 0 \end{Bmatrix} \tag{8}$$

The systems of equations (7) and (8) relate strains to stresses. Strain rates ($\dot{\varepsilon}_x$, $\dot{\varepsilon}_y$) can be substituted to the strains (ε_x, ε_y) by simply using three times the zero shear steady state viscosity (3η) to modulus of elasticity (E)[9]. It is now possible to obtain two expressions that can be implemented in a partial differential equation solver by inverting the matrix and using the following differential expressions for the strain rates in terms of displacements rates in the x and y-directions

$$\dot{\varepsilon}_x = \frac{\partial u}{\partial x}, \quad \dot{\varepsilon}_y = \frac{\partial v}{\partial y}, \text{ and } \dot{\gamma}_{xy} = \frac{\partial v}{\partial x} + \frac{\partial u}{\partial y}$$

For the plain strain condition

$$\begin{aligned} &\frac{\partial}{\partial x}\left[\left(\frac{1-\mu}{1+\mu}\right)\frac{3\eta}{(1-2\mu)}\frac{\partial u}{\partial x} + \frac{\mu}{(1+\mu)}\frac{3\eta}{(1-2\mu)}\frac{\partial v}{\partial y}\right] + \frac{\partial}{\partial y}\left[\frac{3\eta}{2(1+\mu)}\left(\frac{\partial v}{\partial x}+\frac{\partial u}{\partial y}\right)\right] = 0 \\ &\frac{\partial}{\partial x}\left[\frac{3\eta}{2(1+\mu)}\left(\frac{\partial v}{\partial x}+\frac{\partial u}{\partial y}\right)\right] + \frac{\partial}{\partial y}\left[\left(\frac{\mu}{1+\mu}\right)\frac{3\eta}{(1-2\mu)}\frac{\partial u}{\partial x} + \left(\frac{1-\mu}{1+\mu}\right)\frac{3\eta}{(1-2\mu)}\frac{\partial v}{\partial y}\right] - F_y = 0 \end{aligned} \tag{9}$$

and for the plain stress condition

$$\begin{aligned} &\frac{\partial}{\partial x}\left(\frac{3\eta}{1-\mu^2}\left[\frac{\partial u}{\partial x} + \mu\frac{\partial v}{\partial y}\right]\right) + \frac{\partial}{\partial y}\left(\frac{3\eta}{2(1+\mu)}\left[\frac{\partial v}{\partial x}+\frac{\partial u}{\partial y}\right]\right) = 0 \\ &\frac{\partial}{\partial x}\left(\frac{3\eta}{2(1+\mu)}\left[\frac{\partial v}{\partial x}+\frac{\partial u}{\partial y}\right]\right) + \frac{\partial}{\partial y}\left(\frac{3\eta}{1-\mu^2}\left[\frac{\partial v}{\partial y} + \mu\frac{\partial u}{\partial x}\right]\right) - F_y = 0 \end{aligned} \tag{10}$$

These are the partial differential equations that express the mechanics of part deformation controlled by viscous and gravitational forces. The tools used to solve these sets equations are described in the following section.

3.1.4 FINITE ELEMENT MODEL APPROACH

3.1.4.1 Finite element methods

The partial differential equations derived in the previous section need to be solved in order to obtain deformation rates. Solutions to complex sets of PDE's are not easy to obtain and, often, analytical solutions can be derived only for greatly simplified models. Numerical solutions represent the only way of obtaining good approximate results for problems like the one described in this chapter. The availability of larger and cheaper computing power has made possible the development of economical numerical solver packages for a variety of partial differential equations. Most of these programs use a finite element approach to find an approximate numerical solution.

Finite element methods are a powerful tool for solving complex problems that cannot be readily simplified. These methods convert the spatial components of complex sets of continuous partial differential equations (with well defined boundary values) to a set of discrete nodal equations for numerical solving. The spatial area of interest is divided into small patches (finite elements) over which problem variables are represented by simple polynomials. It is possible to obtain solutions within any preset error limits by using a sufficiently fine grid and a sufficiently high order polynomial[7,10]. Finite element solvers use an iterative approach in which at first a coarse grid of finite elements is created. Using this original coarse grid an approximate solution to the problem is obtained. The error in each element is estimated and this information is used to refine the grid by subdividing those elements with an error higher than a pre-specified limit. The new grid is then used to obtain a new solution and the process continues until each element has an error lower than the limit. Figure 3.4 shows this process graphically. The process shown above is performed by the software package used in this analysis (PDEase, Macsyma, Inc., MA 02174). The basic features of the program will be described in the following paragraphs.

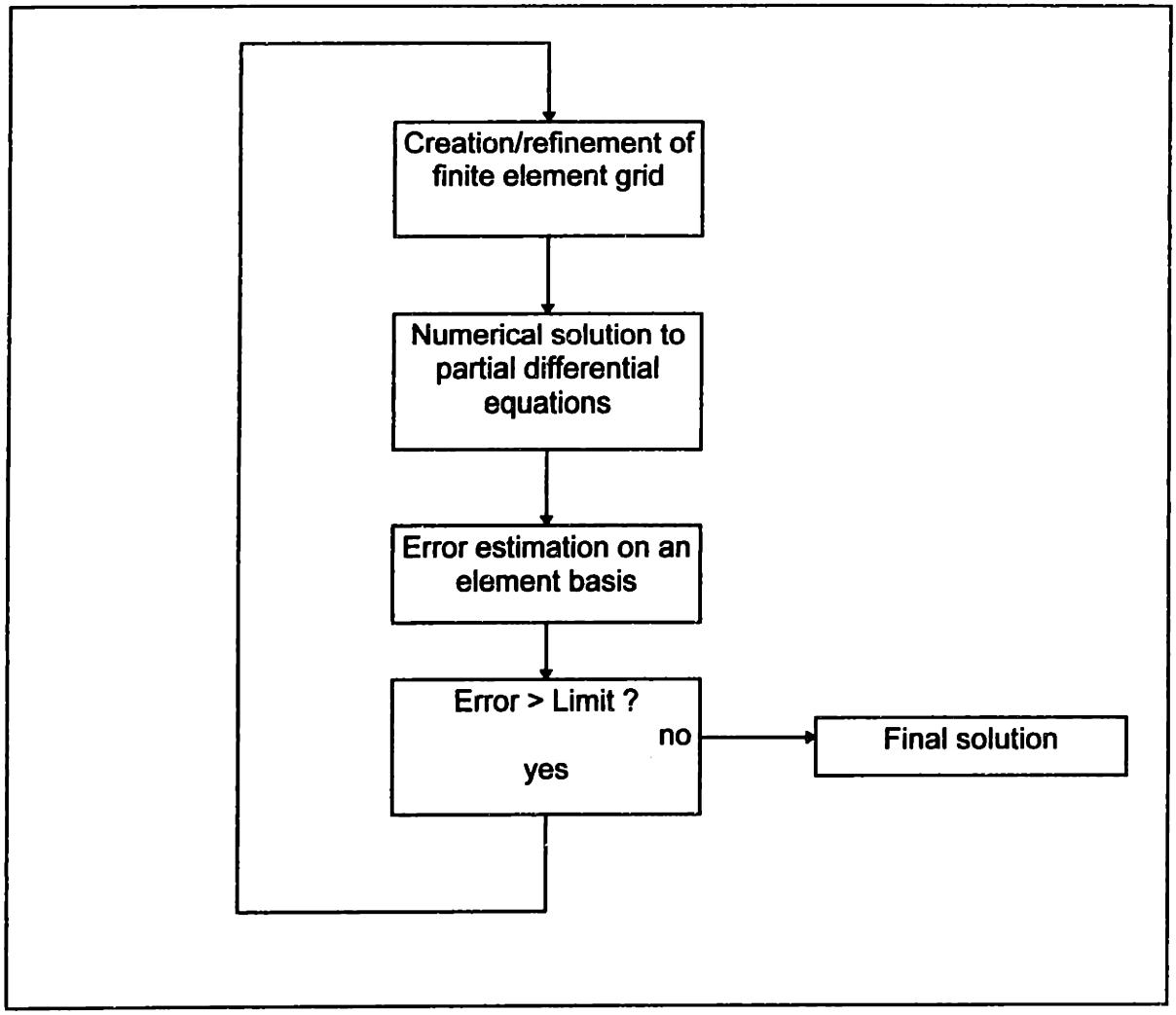

Figure 3.4: Finite element program solution process.

3.1.4.2 Initial grid generation

PDEase2 creates the initial grid according to a precise sequence of node generation and repositioning. First, a series of nodes is created on the boundary segments of the model. The initial density of these nodes can be set a priori. Associated to the node is a "scale size" equal to the length of the smallest leg connected to the node. Internal nodes are created by scattering nodes on successively finer regular meshes and keeping only those that are not within a scale size of the previous node. Node

distribution is completed by scattering the interior nodes as a gas of charged particles: repulsive forces are relaxed until a uniform distribution is achieved. Finally nodes are connected to each other through triangular elements[7].

3.1.4.3 Finite element solver

PDEase2 solves partial differential equations using the Galerkin Finite Element model. The partial differential equation is integrated over the volume (in 3D) or area (in 2D) represented by each cell [9]. The generalized equation

$$L(U) + S = 0 \tag{11}$$

becomes

$$\iiint L(U)\Psi_N dV + \iiint S\Psi_N dV = 0 \tag{12}$$

where Ψ_N is a weighting factor associated with node N, and the volume element dV in Cartesian coordinates is $dxdydz$ ($dxdy$ in 2D) and in cylindrical coordinates is $rdrd\phi dz$ ($rdrdz$ in 2D)[7].

After forming the Galerkin Equations, PDEase2 reduces them by replacing integrals of DIV and CURL operators by their appropriate surface integrals. Any remaining derivative terms are integrated by parts.

3.1.4.4 Measurement of accuracy

Accuracy information is obtained directly from the Galerkin integrals. This information is evaluated at each iterative cycle and it represents the basis for re-gridding of the existing mesh.

3.1.5 FINITE ELEMENT MODEL IMPLEMENTATION

PDEase2 solves two dimensional partial differential equations. A two dimensional model of the injection molded article and the v-grooved setter was prepared. Figure 3.5 shows the finite element model with initial grid.

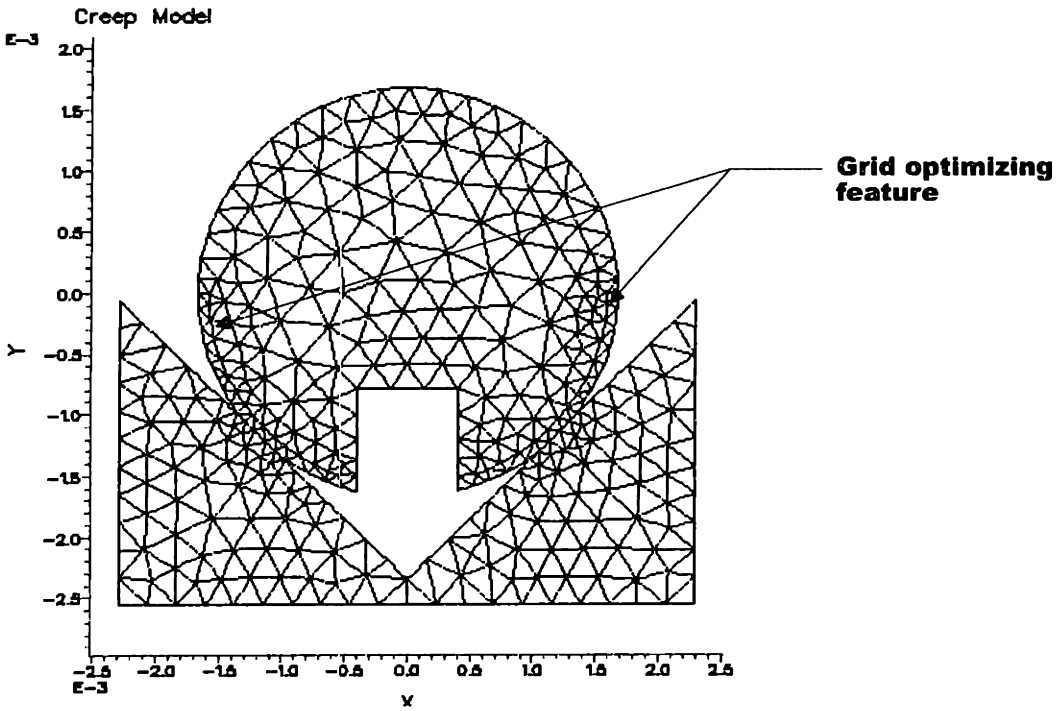

Figure 3.5: Original undeformed grid with grid optimizing feature.

Geometrically this model is identical to the real life sample/setter configuration but for one small detail. The line interface between sample and setter (which corresponds to a point interface in two dimensions) is a point of singularity that can potentially introduce large errors in the computation of the strain rate. The interface between sample and setter was enlarged slightly to prevent this from happening. This was done by forcing the setter walls to intercept the circumference of the sample at a distance from the center of the sample equal to 0.999 times the radius. Figure 3.5 shows

also two small arcs at the base of the sample. These two arcs don't contain any boundary conditions but were designed to improve grid generation around the interface areas by reducing the size of single grid elements.

The model is divided into two regions, ceramic article and setter. The material properties of the two were set separately. The sample properties correspond to those of LV system samples. The body force, F_y, shown in equation (9) and (10) corresponds to the three dimensional specific weight of the sample (32.48×10^3 N/m^3). Information on the steady state shear viscosity of the sample was obtained directly from Creep (600 sec)/Recovery (600 sec) tests at 100°C. The viscosity of the slip compound ranged from a maximum value of 35,000 Pa-sec., to a minimum value of 10 Pa-sec. The material characteristics of the setter were set arbitrarily since the setters, made of aluminum, are undeformable. The setter viscosity was set many orders of magnitude higher than that of the sample and an infinitesimal value was given to the specific weight.

Boundary conditions were relatively easy to set. They consisted in attributing undeformability to the setter by forcing all strain rates in the setter equal to zero. No boundary conditions where imposed on the sample besides the immobility of the sample/setter interface.

3.1.6 RESULTS AND DISCUSSION

Figure 3.6 shows the final grid obtained by the finite element model (see Appendix A for PDEase2 code). The bulk of the grid modifications is concentrated in the area of the interface between the ceramic article and the setter. This result should be expected. Most of the stresses are concentrated in this area which means that the finite element program needs smaller elements to reduce the margin of error.

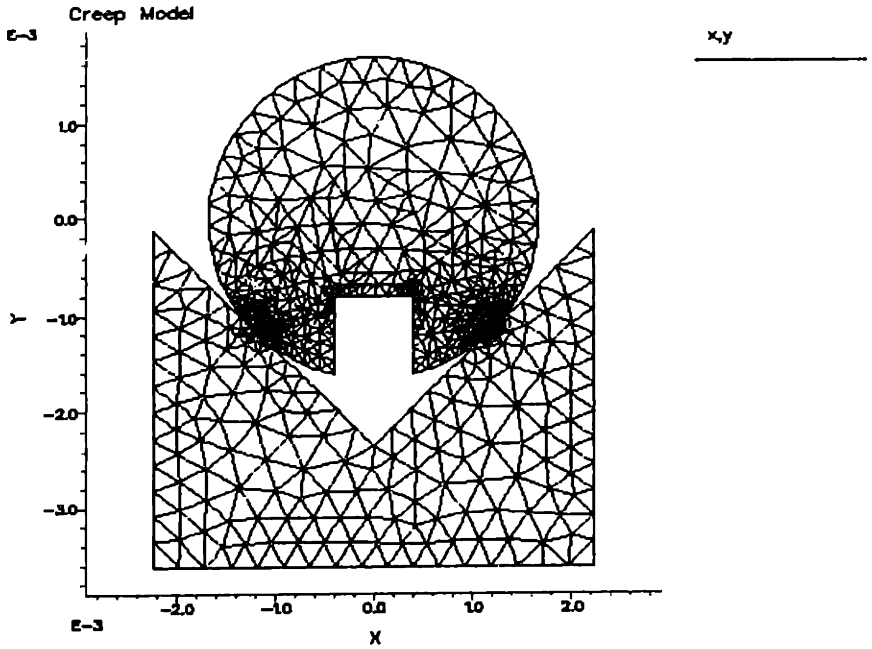

Figure 3.6: Final modified grid.

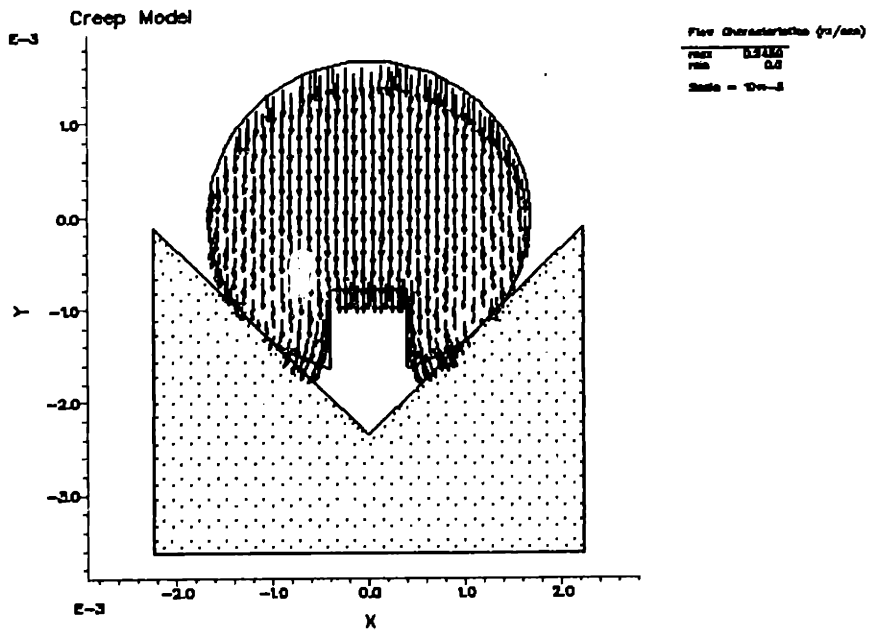

Figure 3.7: Flow path of ceramic article after binder meltdown.

Figure 3.7 shows the calculated flow path of the creeping article. This flow contour is applicable only to the very initial stages of melting. It is, however, indicative of the type of deformation behavior the part experiences. The information given by the finite element program regards strain rates and not deformation magnitudes. It is necessary to check these deformation rates with experimental values. This will be described in the next section.

More accurate information about flow rates at specific locations in the part cross section can be obtained from the type of contour plots shown in Figure 3.8. These contour plots show flow velocity profiles in the x- and y-directions (plots (a) and (b) respectively).

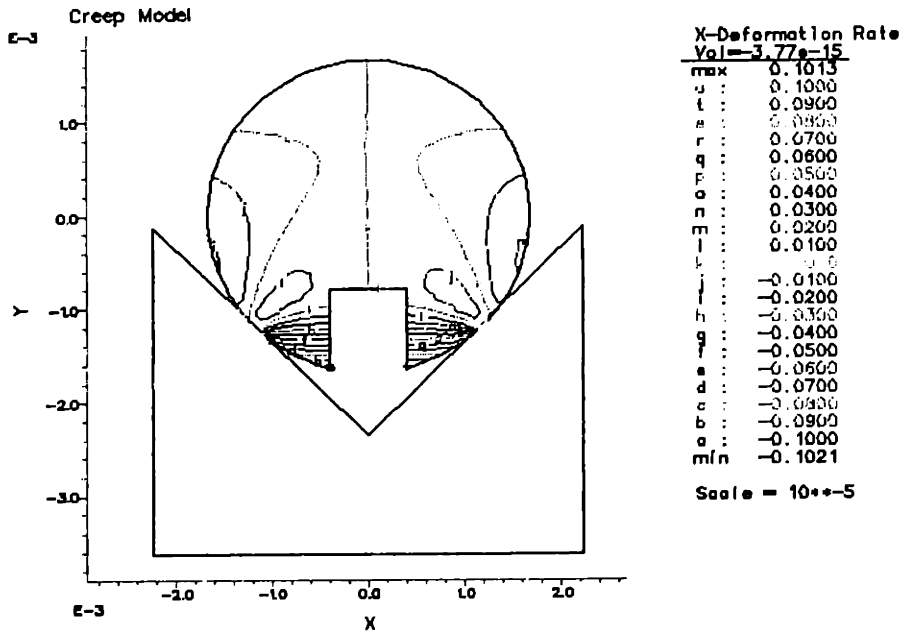

(a)

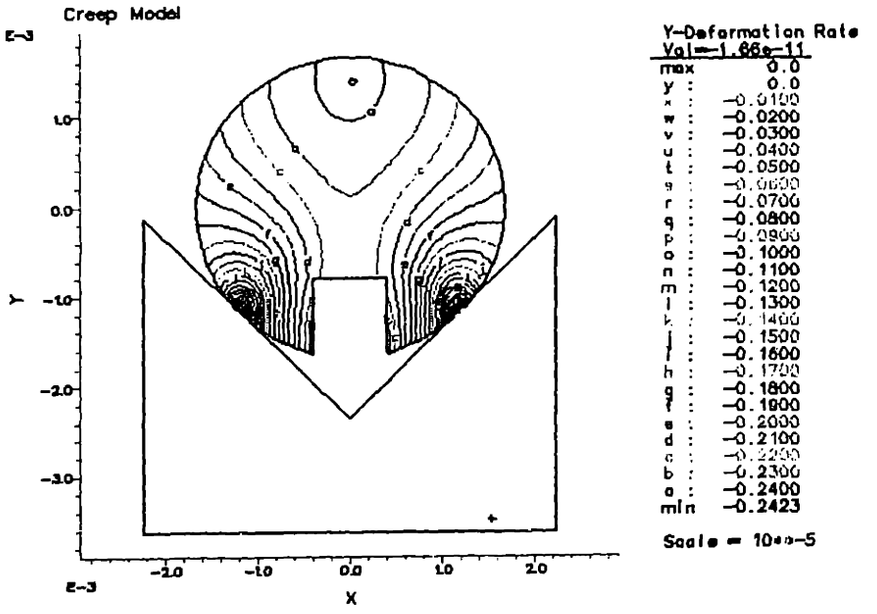

(b)

Figure 3.8: Flow rates in each of the coordinate axis. (a) x-direction, (b) y-direction.

These plots permit calculation of the actual rate of change of sample dimensions such as sample height and width, and notch width. For example, the rate of deformation of the height of the sample (dimension shown in Figure 3.9) was estimated by subtracting the y-flow rates of the uppermost and lowermost nodes of the grid. This deformation rate was calculated for two different values of the viscosity. Table 3.1 shows the rates of height shrinkage for these two values.

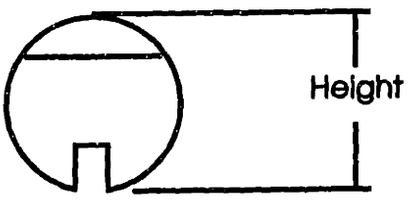

Figure 3.9: Characteristic dimension considered in the calculation of deformation rates.

Table 3.1: Height deformation rates as a function of viscosity.

Sample viscosity at 100°C. (Pa-sec)	Height Deformation Rate (μm/s)
40,000	-.067
48,333	-.056

The negative sign indicates shrinkage. Naturally higher viscosity corresponds to higher stiffness and lower deformation rates.

The values shown above have been obtained using stress equations relative to the plain strain condition. It is possible to compare these results with those that are obtained using the plain stress equations. Table 3.2 shows a comparison between height deformation rates obtained with the plain strain and plain stress conditions.

Table 3.2: Comparison between deformation rates obtained with the plain strain and plain stress conditions (η = 40,000 Pa-sec).

Plain Strain (μm/s)	Plain Stress (μm/s)
-.067	-.102

There is considerable difference between the values obtained according to the two models. The difference between the two can be understood when considering the physical meaning of the two models. The plain strain condition corresponds to a sample bonded to the setter through the sample/setter interface and, therefore unable to deform in the axial direction (this is the condition usually encountered experimentally). The associated stress generated in the axial direction reduces the extent of slumping in the sample. Equation 7 can be used to calculate stresses in the z-direction. The finite element model shows that the component is mostly in compression in the z-direction except for a small area surrounding the notch. An object in compression tends to expand in the plane perpendicular to the compression force. This expansion compensates, in

part, for the effect of slumping, by reducing the difference between top and bottom deformation rates in the sample.

The finite element model can also be used to test different setter geometries, and, in particular, different setter/sample interface angles. Figure 3.10 shows the flow patterns of a sample positioned on a setter with a 60° interface angle.

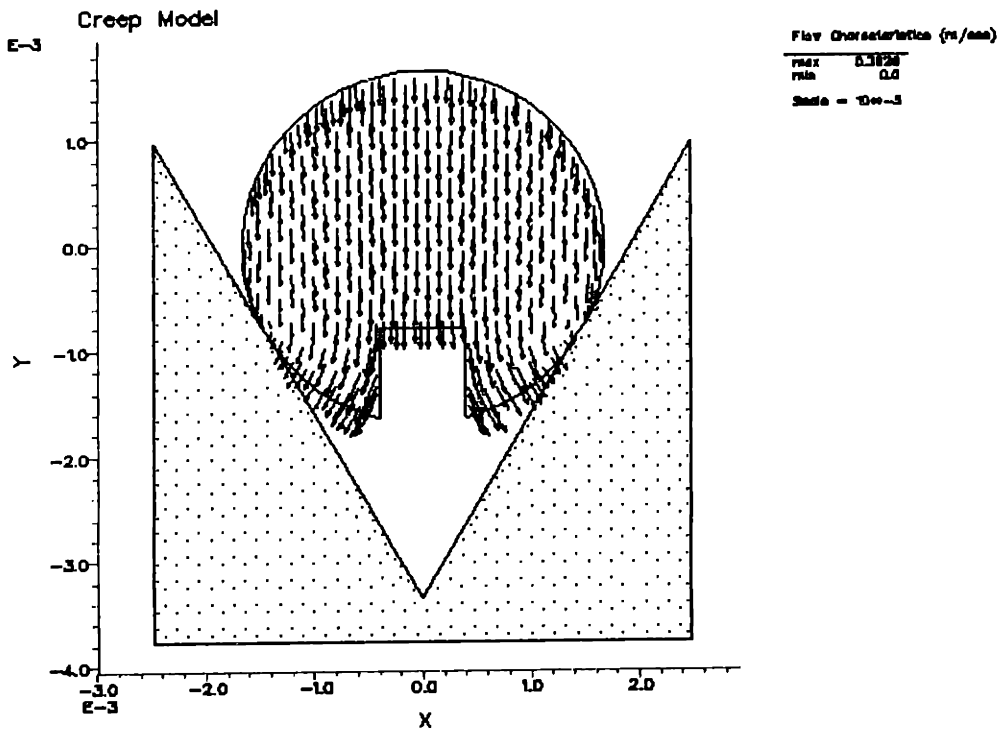

Figure 3.10: Flow pattern for a sample resting on a 60° setter.

Table 3.3 shows a comparison for the rate of change in height for samples on 45° and 60° setters.

Table 3.3: Height deformation rates for samples resting on 45° and 60° sample/setter interface surfaces.

45° Groove (μm/s)	60° Groove (μm/s)
-.067	.457

The most striking feature about the two rates of deformation is that the height of the sample being heat treated on the 45° groove setter diminishes while that of the sample on the 60° groove setter increases. These two modes of deformation could not have predicted without the use of the finite element model, and this fact re-emphasizes the importance and usefulness of the theoretical approach. This result suggests that there is a setter groove angle between 45° and 60° that inhibits deformations in the height of the sample. This groove angle was determined by trial and error with the use of the finite element program. Several setter groove angles were tested and the rates of deformation of the height of the sample calculated. Figure 3.11 shows the results of this search.

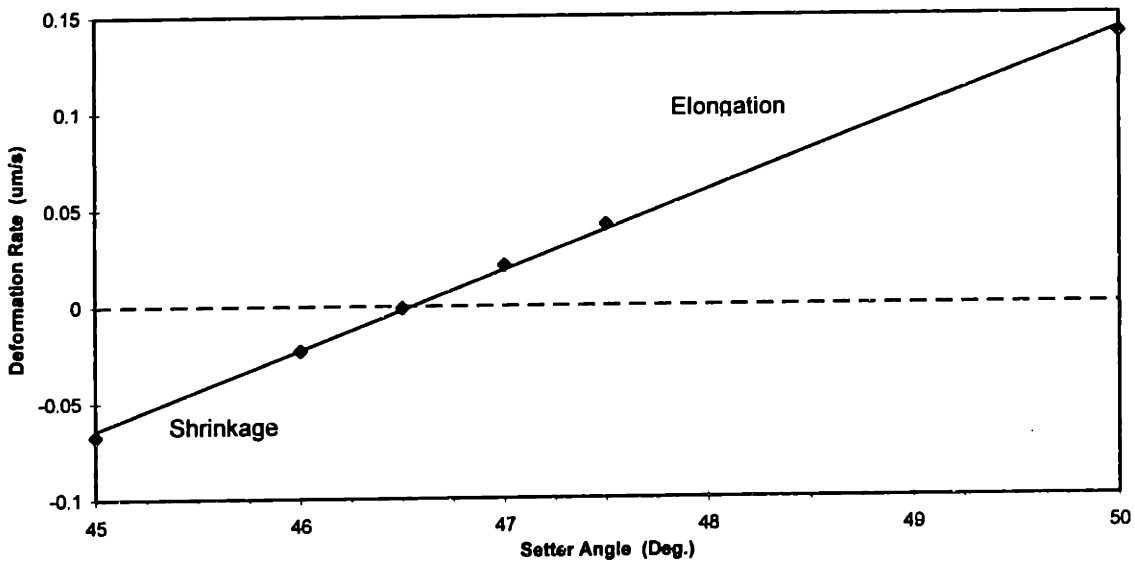

Figure 3.11: Height deformation rates as a function of groove angle.

Height deformation rate seems to be very sensitive to setter angle. The setter angle that inhibits distortions in the height of the sample is 46.5°. It should be noted, however, that the sample still undergoes distortions in other dimensions: the considered angle optimizes only the height changes in the sample, not other characteristic dimensions. It is interesting to note that the angle necessary to obtain no height distortions produces the lowest and narrowest stress distributions in the sample. This is shown by Figure 3.12 which depicts x and y-stress distributions in the sample cross-section.

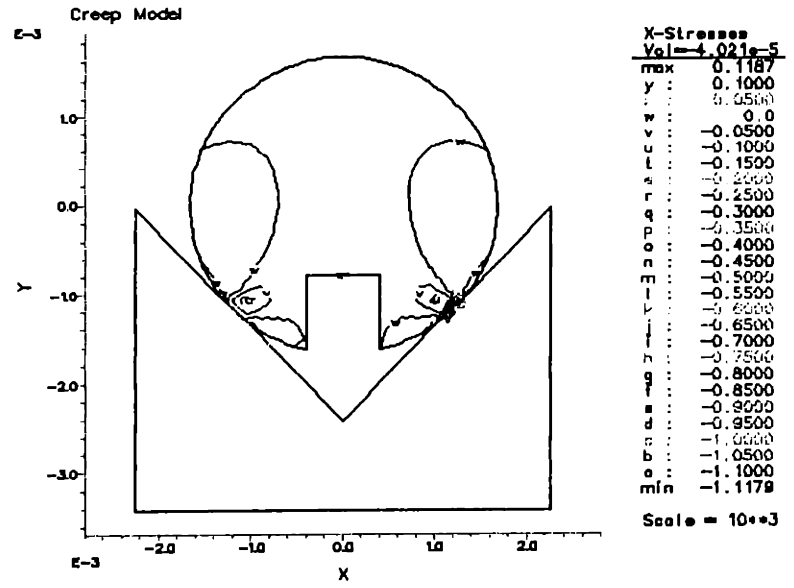

(a)

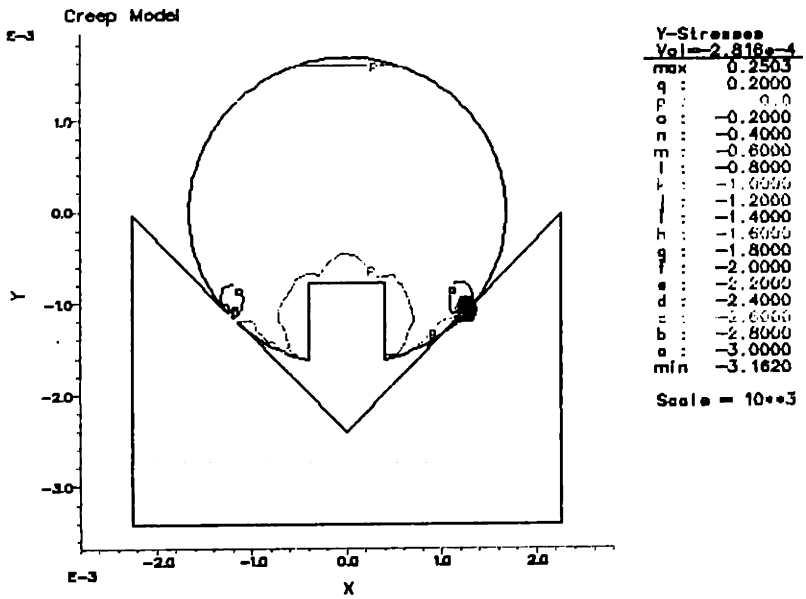

(b)

Figure 3.12: Internal stress distributions for a sample on a setter with a 46.5° groove angle.

3.1.7 CONCLUSIONS

The creation of a model capable of predicting part deformation rates was an important tool in optimizing production parameters. It gave useful insight in the complex interactions existing between ceramic article and setter. The model can be a helpful tool in determining what setter geometry would allow for minimum part distortion of a particular dimension, before preliminary production runs even begin. The accuracy of the model, however, needs still to be tested. The theoretical results need to be compared with the deformation rates encountered in real components. It should also be noted that the model described in this chapter focuses on part flow rates based solely on viscous and gravitational forces. The mass transfer of binder between the sample and the setter has not been modeled because of the complexity of the problem.

The following section describes experiments aimed at determining the accuracy and dependability of the finite element model. The correlation existing between this particular model and heat treatments in which binder is transferred from sample to setter is considered in the next chapter.

3.2 CORRELATION BETWEEN FINITE ELEMENT MODEL AND EXPERIMENTAL RESULTS

3.2.1 INTRODUCTION

The previous section was devoted to the description and analysis of a finite element model used to predict deformation rates in injection molded ceramic articles during heat treatment. The finite element model was designed to reproduce the distortions occurring in a ceramic component resting on a v-grooved aluminum setter at 100°C. Transfer of binder from the ceramic article to the setter was not modeled because of the complexity that this would introduce into the model. It is still necessary, however, to determine the

accuracy of the model and determine where discrepancies with the experimental results occur.

This section describes a set of experiments aimed at determining the finite element accuracy in predicting deformation rates. The experimental setup and measuring technique will be described first. Results obtained from the model and those obtained experimentally will then be compared to each other, and conclusions on the model's accuracy will be drawn.

3.2.2 MATERIALS AND METHODS

LV system samples were used in this experiment. The samples were heat treated as received. Setters were prepared from aluminum blocks. This material was chosen because of the absence of pores (which is necessary to reproduce the same conditions of the finite element model), and the relatively ease of machining. The 45° degree grooves where prepared using a multi-flute carbide bur with a 90° tip in a milling machine. The grooves were approximately 2 mm deep. The experiment was performed in a Lindberg furnace type 54352 (Lindberg, Watertown, Wis. 53094).

Sectioning was performed with a low speed saw (Isomet Low Speed Saw, Buehler LTD) and polished (Ecomet IV, Buehler LTD). Pictures of the cross-sections of the samples were taken using a macro camera (Nikon). These pictures where digitized and analyzed using an image measurement program (Sigma Scan, Jandel Corp., San Rafael, CA 94912-7005).

3.2.3 EXPERIMENTAL PROCEDURE

An inert atmosphere of nitrogen (flow rate = 1 SCFH) was maintained in the furnace to prevent binder degradation due to oxidation. The samples where placed over the aluminum setters and heated at a rate of 2°C/min to 100°C. This unusually high heating rate was chosen to minimize the time required to reach the target temperature in order to reduce distortions occurring in between melting and 100°C. Samples were extracted from the furnace as soon as the target temperature was reached and 4, 14, 49, and 234 minutes thereafter. Samples were quenched in air upon extraction.

The main objective of this experiment was to extract data regarding deformation rates from the measurements of the cross-sections of the samples. To do this, samples were first bonded with 5 minute epoxy to the internal edge of a 3cmx3cmx3cm cubic plastic container and then enclosed in epoxy. This was done to ensure that all samples were sectioned with a plane perfectly perpendicular to their main axis. Figure 3.13 shows sample handling procedure.

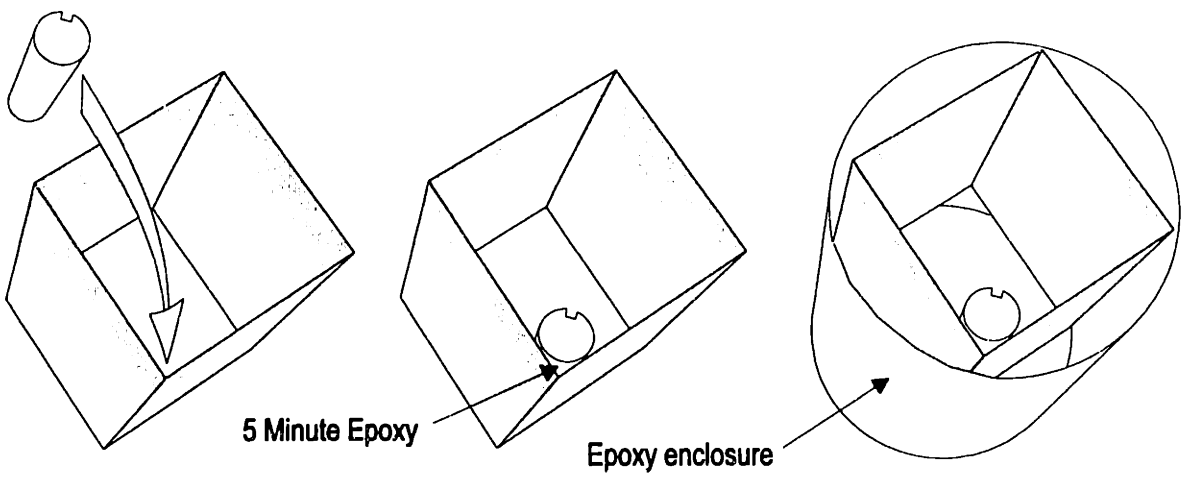

Figure 3.13: Sample handling procedure prior to sectioning.

Theoretical deformation rates were obtained from the PDEase2 finite element model for two different shear viscosities. These deformation rates were then plotted together with the deformations measured experimentally.

3.2.4 RESULTS AND DISCUSSION

Figure 3.14 shows five different sample cross-sections after heat treatment. The evolution of the sample deformation is quite evident from the photographs. Two major areas of deformation can be observed. One area of deformation is located at the interface between sample and setter. This area of the sample flattens and spreads against the surface of the setter. The deformation is already visible at time "0", which is the time at which the sample reached the target temperature, meaning that significant deformations occurred immediately after binder melting. This type of behavior was also encountered in preliminary experiments (see Chapter 2). Also, it should be noted that, in part, this deformation was already included in the finite element model by increasing the size of the sample/setter interface. Even if it was done to avoid a point of singularity, the geometry chosen in the model reflected actual deformation. The second noticeable deformation feature is the spreading of the notch at the bottom of the sample. The walls of the notch spread apart from each other increasing the distance between the bottom two corners, and the process continued throughout the whole heating cycle.

An initial qualitative analysis can be made by comparing experimental flow patterns, shown in Figure 3.7, with theoretical ones obtained with PDEase2 and shown in Figure 3.14. The correlation between the model predictions and the actual flow patterns is impressive.

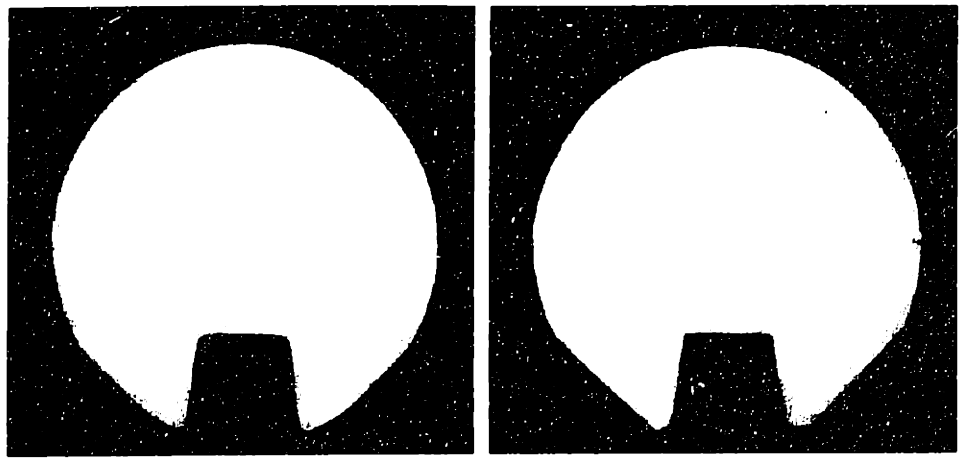

0 min

4 min

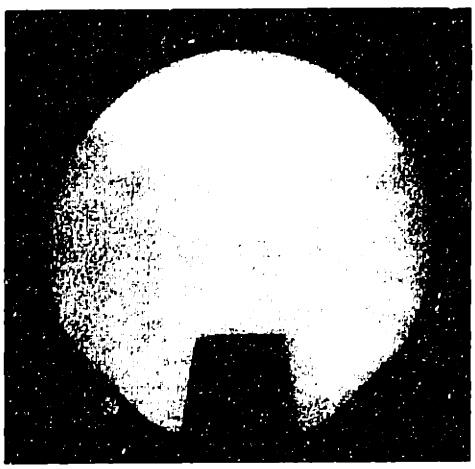

14 min

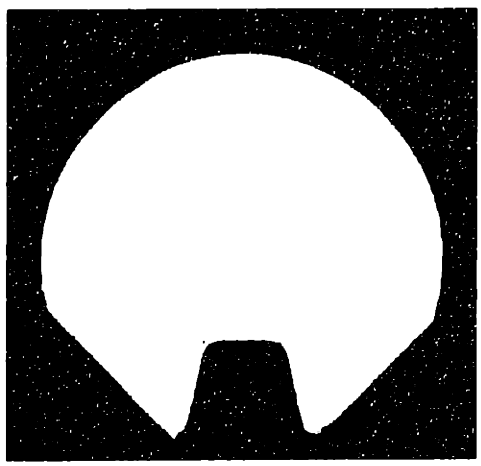

49 min

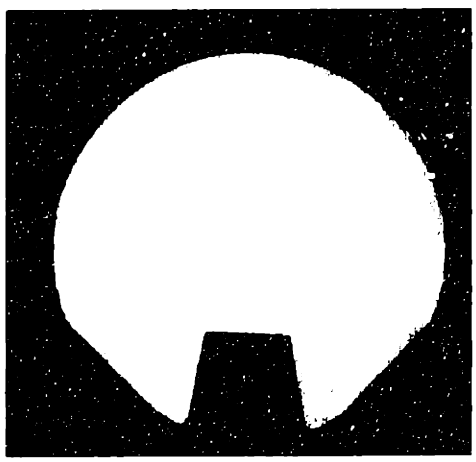

234 min.

Figure 3.14: Sample cross-sections after heat treatment (LV system).

The two deformation features noticed above, the flattening of the sample/setter interface and the spreading of the notch, are well reproduced by the finite element model, confirming the qualitative accuracy of the model.

The accuracy of the finite element model needs to be evaluated quantitatively as well. To do this, measured deformation rates were compared with the theoretical values obtained from PDEase2. The characteristic length compared was the height of the sample cross-section, shown in Figure 3.9. The deformation rates have been reported in Table 3.1.

These values can be plotted against the measured heights as a function of time. Figure 3.15 shows a comparison between theoretical and experimental height changes as a function of time. The changes are calculated relative to the height of the sample at 100°C. The finite element generated deformation rates are represented as the slope of the theoretical curves. The plot shows that, at least initially, experimental deformations vary almost linearly with time. This corroborates the assumptions made in the finite element model. There is a very close correspondence between the experimental values and theoretical predictions from the finite element model. The initial experimental deformation rate falls in between the curves obtained for values of viscosity between 40,000 and 45,333 Pa-sec. The experimental deformation rate decreases as time increases, as expected, since only in the early stages of distortion the part behaves as a perfectly viscous fluid. The theoretical model, as explained earlier in this chapter, produces a constant deformation rate. The match between theoretical and experimental results is excellent up to approximately 15 minutes after reaching the target temperature. It should also be remembered that Figure 3.15 does not show deformation occurring in the time required to reach 100°C.

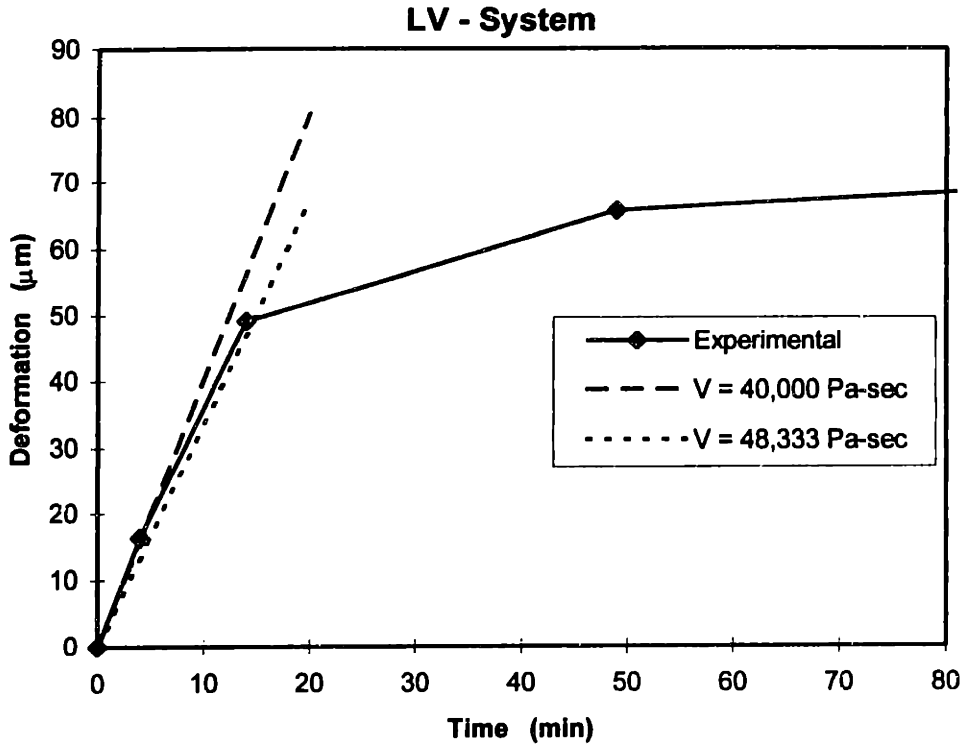

Figure 3.15: Theoretical and experimental values for height shrinkage as a function of time.

3.2.5 CONCLUSIONS

The accuracy of the finite element model was evaluated qualitatively and quantitatively. The finite element model predicted with great accuracy flow patterns and deformation rates of the sample height, confirming not only the feasibility but also the usefulness of modeling complex phenomena for this type of applications. It should be noted that the finite element model should be used carefully. Minimizing deformation of a particular dimension does not necessarily mean that all sample dimensions are minimized. Great care should be taken in establishing which sample features are affected by specific setter geometries. The finite element model allows to do this conveniently and accurately.

The model as it is, however, applies to a very specific deformation regime in which no mass transfer takes place between sample and setter. This phenomenon is difficult to model and it was not pursued in this study. Future research should focus in adjusting the model to include the effect of mass transfer. This cannot be done before determining the factors governing binder transfer from the sample to the setter and the effect on article deformation. The next chapter will describe a series of experiments aimed at understanding this complex phenomenon.

[1] Edirisinghe, M. J., Evans, J. R. G., "Fabrication of Engineering Ceramics by Injection Moulding. I. Materials Selection," Int. J. High Technology Ceramics, **2**, 1-31 (1986).

[2] Edirisinghe, M. J., Evans, J. R. G., "Fabrication of Engineering Ceramics by Injection Moulding. II. Techniques," Int. J. High Technology Ceramics, **2**, 249-278 (1986).

[3] Bland, D. R., "The Theory of Linear Viscoelasticity," Pergamon Press, Oxford, 1960.

[4] Gittus, J., "Creep, Viscoelasticity and Creep Fracture in Solids," John Wiley & Sons, New York, 1975.

[5] Findley, W. N., Lai, J. S., Ovaran, K., "Creep and Relaxation of Nonlinear Viscoelastic Materials," North-Holland Publishing Company, New York, 1976.

[6] Poirier, J. P., "Creep of Crystals: High Temperature Deformation Processes in Metals, Ceramics and Minerals," Cambridge University Press, Cambridge, 1983.

[7] "PDEase2® Release Notes," SPDE Inc., Bass Lake, CA, 1995.

[8] Backstrom, G., "Fields of Physics on the PC," Studentlitteratur, Lund, 1994.

[9] Byron, R. B., Armstrong, R. C., Hassager, O., "Dynamics of Polymeric Liquids. Volume 1: Fluid Mechanics," John Wiley & Sons, New York, 1987.

[10] Plybon, F., "Applied Numerical Analysis," PWS-Kent Publishing Co., Boston, 1992.

4. BINDER WICKING

4.1 INTRODUCTION

The previous chapters have been dedicated to the analysis of the deformations occurring in injection molded samples during heat treatment and to the formulation of a model capable of predicting rates of deformation. The experiments described in Chapter 3 showed that the most important contributor to article deformation was slumping due to liquefaction of the ceramic component and consequent loss of structural support. This phenomenon occurred, as expected, independently of heating rate. Bubble formation was seen to have a role only at high heating rates. These results suggested that removal of the liquefied binder played an important role in reducing distortions.

Binder removal from injection molded ceramic articles can be performed in several ways including thermal degradation, oxidative degradation, evaporation, solvent extraction, and capillary flow into a porous media[1,2]. The latter is sometimes performed by embedding the injection molded articles in a fine powder such as alumina. The powder bed performs several functions. It allows for temperature uniformity at the surface of the article, it extracts fluid from the article by capillary action, and it supports the part in its softened state preventing sagging[1]. Capillary action from the powder bed depends closely on processing variables. Finer powders lead to higher binder removal rates. This is due to the greater capillary pressure exerted by the smaller pores in the wick, since capillary pressure is inversely proportional to pore radius. Analogously, binder removal rates are higher for samples with larger pore sizes (computed as one-half the mean free path between particles). Also, as the percentage of debinding increases, the binder removal rate decreases because of the decreased permeability of the sample and the presence of greater amounts of binder in the low permeability wick[2]. This factor will be important when considering binder migration inside the sample.

Embedding the ceramic component in a powder medium is a useful technique when trying to maximize the amount of binder removed. This technique, however, can only be used with relatively large parts and in low production runs. It is difficult, however, to reproducibly pack small articles in the ceramic powder. The whole operation becomes too laborious, time consuming, and expensive.

The impracticality of performing binder removal by capillary flow into a porous powder covering the article does not exclude the possibility of using similar techniques more apt to be used in the manufacturing process. A common technique used in industry consists of removing binder from the ceramic article by capillary suction into a porous substrate. This technique does not require the part to be covered by a powder medium; the porous medium need not be in powder form at all. Instead, the ceramic article rests on a porous substrate known as "setter" which performs a function similar to that of the porous powder. Setter geometry as well as microstructure play a very important role in determining the extent and rate of development of the binder removal process. However, very little interest has been shown in optimizing setter characteristics to maximize binder removal and minimize sample distortions. The decision of choosing a particular setter instead of another is usually based on three setter characteristics that are not necessarily determinant factors in the binder removal process. Mostly companies are interested in using setters that are light, easy to handle (tough and impact resistant), and economical[3]. Very little research has been done into studying exactly how mass transfer between sample and setter is affected by setter geometry, sample/setter interface configuration, setter microstructural characteristics. This chapter will analyze setter characteristics with the specific goal of asserting their influence on binder removal from the green ceramic sample. The chapter describes a series of experiments aimed at providing greater understanding of the relationship existing between the parameters and characteristics described above and their influence on mass transfer and, consequently, sample distortion. The experiments focused on three major areas:

1) mass transfer between sample and setter as a function of interface geometry and setter microstructural characteristics;

2) rate of binder loss and flux as a function of sample dimensions;

3) sample deformations as a function of binder transfer rates and magnitudes.

4.2 RELATIONSHIP BETWEEN BINDER REMOVAL, SETTER POROSITY, AND INTERFACE GEOMETRY

4.2.1 INTRODUCTION

The results analyzed in Chapter 2 showed that considerable distortion was encountered during the initial stages of heat treatment, at relatively low temperatures and binder losses. The analysis of these deformations through a range of temperatures confirmed the theory that distortions were mostly caused by slumping of the sample due to loss of structural support from the binder. Dimensional instabilities are created by a transition from solid to viscous binder behavior. The experiments described in Chapter 2 and 3 and the finite element model described in Chapter 3 showed that these deformations occur soon after liquefaction and at relatively high rates. It is therefore critical to remove as much binding medium as possible after liquefaction to reduce slumping of the parts. This process has the effect of reducing the viscous behavior of the binder.

There are two ways that binder can be removed from the sample during heat treatment: wicking into the setter and volatilization. Wicking of the binder into the setter can take place only after melting, while volatilization can be achieved only when one or more of the binder components vaporizes. Because of their nature, these two mechanisms are dominant at different stages during the binder removal process and at different temperatures. Wicking will be likely to act as the more prominent mechanism during the early stages of heat treatment and at relatively low temperatures, which are the conditions researchers and industry are most interested in.

Little is known about mass transfer between sample and setter and how this is influenced by both, nature of the setter (in particular porosity), and type of interface

between sample and setter. It is necessary to understand how these parameters affect binder removal and how they can be tailored to reduce the magnitude of the distortion affecting the heat treated parts.

It should be noted first that the process of substituting fluids from porous materials is quite complex. Capillary pressure is subject to hysteresis. Because of this phenomenon, the relationship between the capillary pressure and the saturation of the material are not unique, and one cannot determine one value from knowledge of the other without knowing the pat wetting-drying history of the material considered. Different capillary pressure vs. saturation curves may be obtained, depending on whether a material is initially saturated with a wetting or non-wetting material. Substitution of the wetting fluid with a non-wetting one is called drainage. The opposite process is called imbition. Figure 4.1 shows two curves, one for drainage and one for imbition, of capillary pressure vs. saturation (kerosene and water in sandstone)[4].

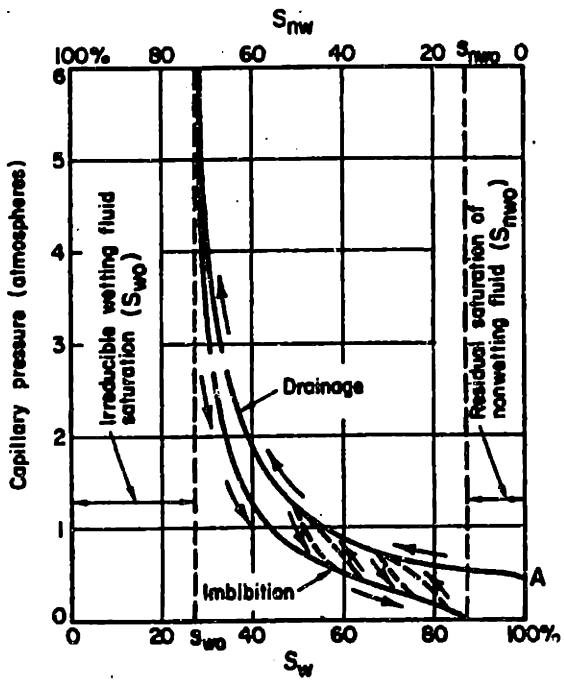

Figure 4.1: Typical capillary pressure-wetting fluid saturation curves illustrating hysteresis[4].

Drainage and imbition stop when equilibrium between capillary pressures of the fluid-fluid interfaces is achieved. This condition, however, does not correspond to same

level of saturation because of hysteresis. Equations 1 and 2 are therefore oversimplified but they represent a good and useful approximation for modeling wicking phenomena.

Prior to performing the experiments required to understand these mechanisms, it is necessary to create a model that allows to predict to what extent binder can be removed from the sample by wicking. The extent of binder wicking into the sample is controlled by the relative pressures exerted by the curvatures of the sample and the pores in the setter. Two cases are considered, as shown by the idealized sample cross-sections shown in Figure 4.2.

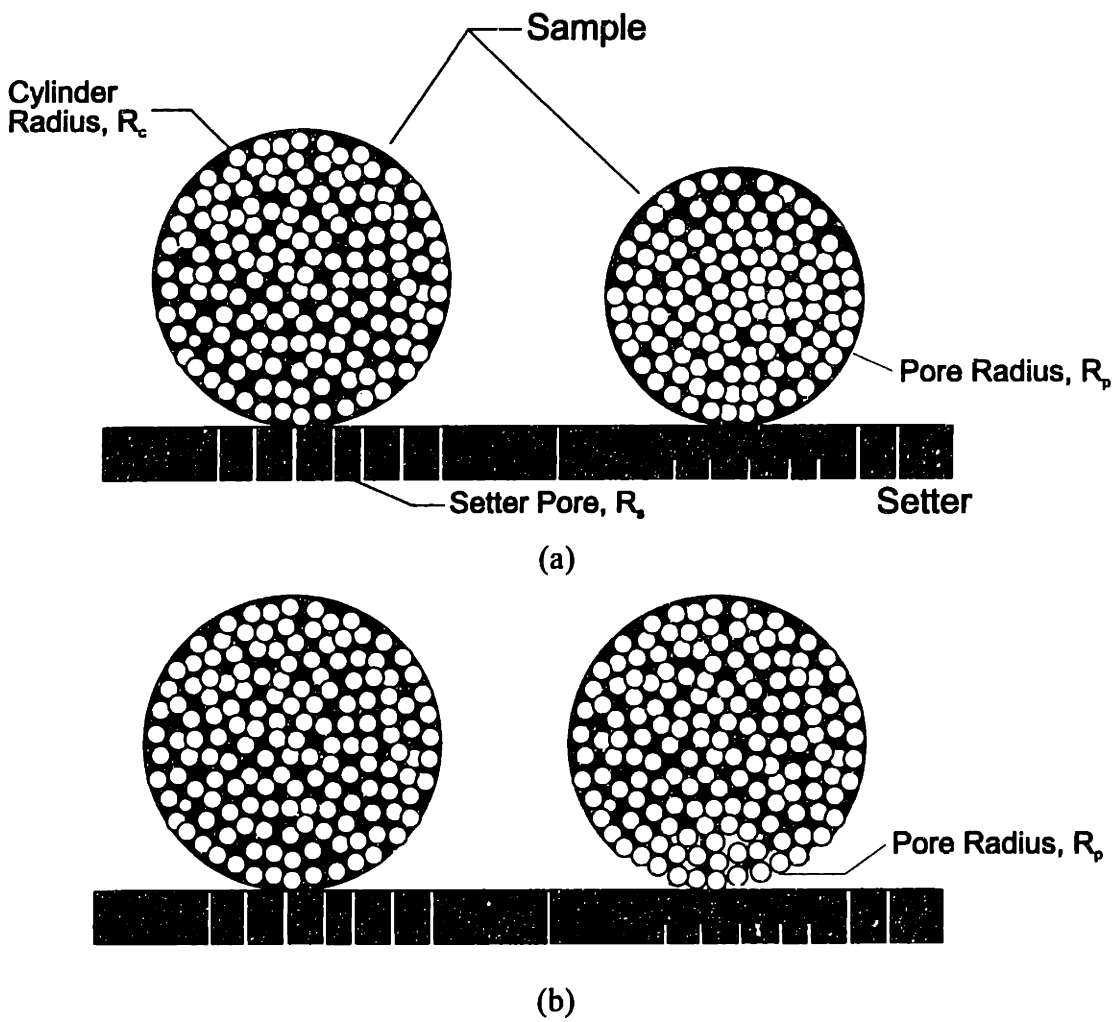

Figure 4.2: Idealized representation of sample cross-section before and after wicking of binder for two different wicking mechanisms.

Figure 4.2(a) shows initial and final cross-sections of a sample in which very low hydraulic resistance opposes binder transfer within the sample (hydraulic resistance will be discussed shortly). Binder is removed from the sample/setter interface and it is drawn uniformly from throughout the sample. Ceramic particles are reorganized as mass is lost, so that uniform shrinkage with little pore formation takes place. Once the particles reach a random closed packed structure and no further reorganizing is possible, pores start forming at the surface of the body. Wicking terminates when pores in the setter and the sample become equal in size and no capillary pressure difference exists. Hydraulic resistance to mass transfer through the porous medium is much larger in case (b). Binder can only be removed from areas close to the interface between sample and setter and pores are created in this region. Little or no shrinkage of the part occurs and binder concentration gradients are created within the sample. Binder wicking ceases when capillary pressure in the sample and the setter equalize or when hydraulic resistance becomes too high due to decreased permeability.

Capillary pressure is inversely proportional to curvature of the liquid-vapor interface. The pressure gradients due to curvature between the sample and the setter are different for the two cases. In the green, untreated, sample there are no pores between particles. The difference in pressure (assuming zero contact angle) is therefore

$$\Delta P = -\frac{2\gamma}{R_s} - \frac{\gamma}{R_c} \tag{1}$$

where γ is the surface tension of the binder, and R_c and R_s the radiuses of the sample and the setter pore respectively. The radius of the sample is much larger than that of the pores in the setter so that the second term of the above equation can be neglected. The difference in pressure between the setter and the sample drives the binder from the sample to the setter causing wicking.

$$\Delta P = -\frac{2\gamma}{R_s} + \frac{\gamma}{R_p} \tag{2}$$

The case represented by the idealized samples on the right is different. Since binder has been removed, pores that are formed in the sample have to be considered. These pores counteract the pressure exerted from the pores in the setter. The expression

for the pressure difference between sample and setter now becomes (2), where R_p is the radius of the pore in the sample. This equation shows that when the radius of the pores in the sample and the setter are equal, wicking of the binder ceases because the driving pressure from the setter and the resisting pressure exerted by the pores in the sample equal each other. This means that the amount of binder removed from the sample depends on two factors: the size of the pores in the setter, which determines the primary driving force, and the size and extent of pores forming in the samples as binder wicks out.

The resistance to flow inside a porous medium needs also be considered as well. Equation (3)

$$q = -\left(\frac{k}{\eta}\right)\frac{\partial \Phi}{\partial x} \tag{3}$$

is the one dimensional version of Darcy's law, governing the flow of a fluid with viscosity η through an isotropic porous medium under a pressure gradient $\partial\Phi/\partial x$; q is the specific flux vector and k is the permeability of the porous matrix[4]. There exist several expressions for k, ranging from empirical formulations to purely theoretical ones. For this application k can be calculated as

$$k = \frac{\beta d^2 \varepsilon^2}{[\lambda(1-\varepsilon)]} \tag{4}$$

where β is a geometric factor (for spherical particles $\beta = \pi/6$), d is the diameter of the powder particles, ε is the void fraction of packing, and λ is a coefficient that depends on the streamline configuration around the spherical particles. For the case of a particle in an infinite fluid, fully saturated green sample, $\lambda = 3\pi$[4].

Darcy's law allows to calculate the pressure gradient necessary to remove binder as a function of distance from the interface, the larger the distance, the stronger the pressure required to remove binder at a given rate. This will determine how far inside the sample the action of the setter can be felt, that is, from where in the sample binder can be removed. This distance is limited by the capillary pressure exerted by the setter. When the capillary pressure exerted by the setter is small compared to that required to remove

binder, removal will be limited to the areas surrounding the sample/setter interface. These areas will see a decrease in binder content and an increase in porosity. Other areas in the sample will remain relatively binder rich and pore free.

Pore formation can be monitored by measuring sample shrinkage and comparing it to the actual volume loss calculated from binder loss data. Pore formation is shown by the difference between actual shrinkage and expected values obtained from weight loss data. Unfortunately this method does not allow to localize pore formation. Gradients in binder content can, however, be observed by Thermal Gravimetric Analysis which will be described shortly.

4.2.2 MATERIALS AND METHODS

This series of experiments was performed to understand the relationship between setter porosity and sample/setter interface characteristics and amount of binder removed from the sample. The experiments were performed with the same type of samples described in Chapter 2, that is, injection molded ceramic articles consisting of zirconia powder and two different types of binder systems. A low viscosity (LV) wax based proprietary binder system and a high viscosity (HV) polyethylene based binder system. In addition, small amounts (1 to 2% by weight) of solvent red 24 dye where added to some of the samples prior to injection molding. This was done to allow for monitoring of binder distributions through porous setters.

Several types of setters where used in these experiments. The setters were chosen with a wide distribution of pore sizes and microstructures. This was necessary to test binder removal behavior against a relatively large range of setter characteristics. Two types of tests were performed on the setters to characterize their microstructure. Initial tests involved mercury porosimetry [Autopore II 9220, Micromeritics, Norcross, GA 30093]. These preliminary tests allowed to determine the average pore size of each setter and the general pore size distribution obtained from the differential volume intrusion

peaks. Table 4.1 shows the results of the mercury porosimetry analysis and Figure 4.3 shows the plots relative to the differential volume intrusion data.

Table 4.1: Average pore diameter and pore diameter at intrusion volume peaks

Setter type	Average pore diameter (μm)	Pore diameter at intrusion volume peaks (μm)
Selee foam	0.6	0.34 - 0.74 - 1.14 - 1.38
Plaster	0.9	0.4 - 0.85 - 1.3
Blasch - 20% Permeable	1.13	0.35 - 0.85 - 1.23
Zircar - 70% Porous	6.75	2.6 - 8.4
Blasch - 35% Permeable	7.25	6.6 - 8.2
Zircar - 93% Porous	10.65	10.1
Blasch - 45% Permeable	10.70	10.25

The information reported above is necessary in understanding binder wicking behavior but, often, not sufficient. Some particular cases of binder wicking behavior cannot be explained simply by porosimetry data. Further analysis of the microstructure of the setter is necessary. SEM [S-530 Scanning Electron Microscope, Hitachi Instruments Inc., Danbury, CT] analysis was performed on all setters to determine their particular microstructural architectures. This information became extremely useful in explaining the behavior of some sample/setter combinations. The SEM pictures will be shown in this work, whenever necessary.

The setter materials described above where formed in two main types of geometries. These configurations were chosen as two extremes of sample/setter interface areas. Figure 4.4 shows these two types of configurations.

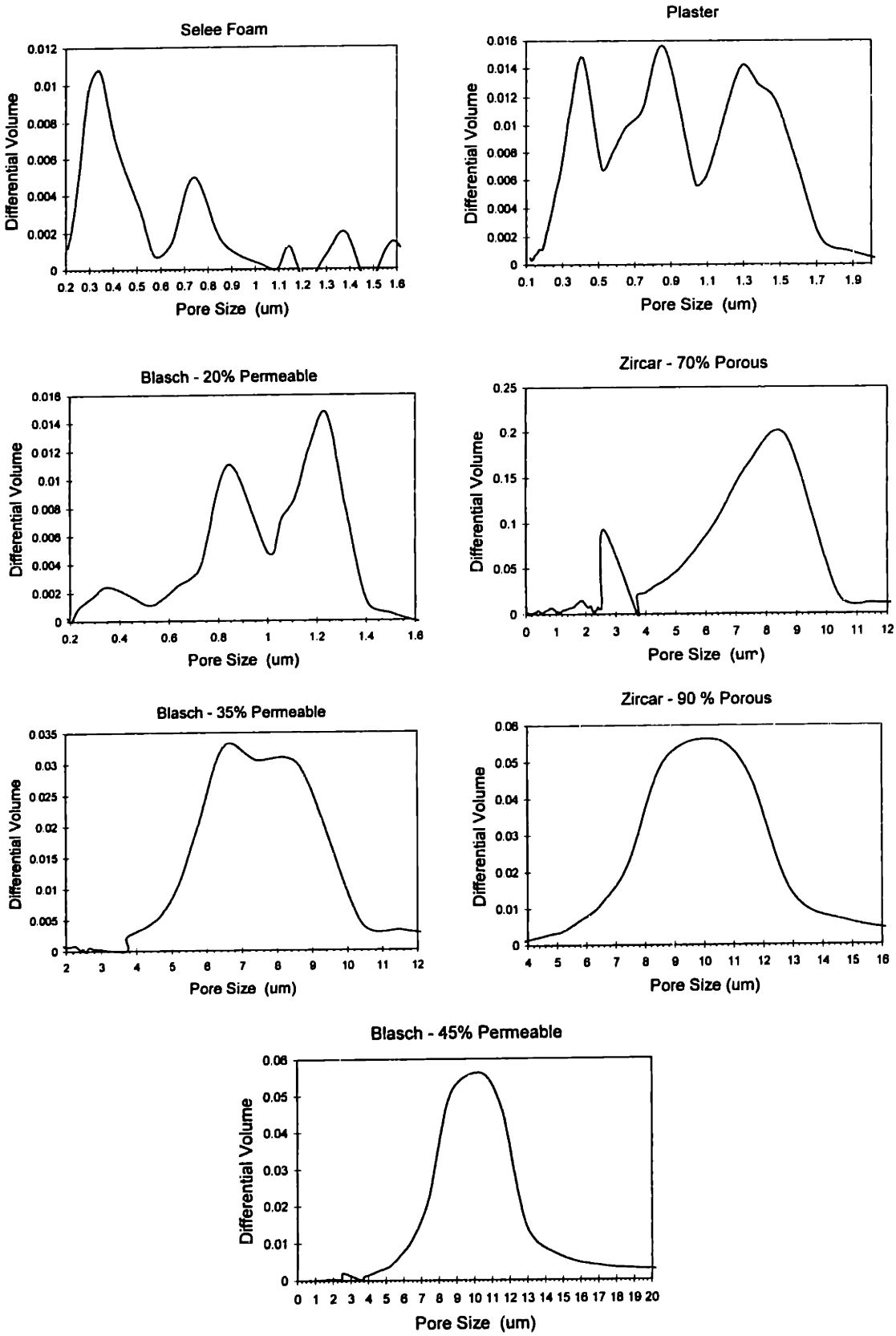

Figure 4.3: Differential volume intrusion peaks from mercury porosimetry data.

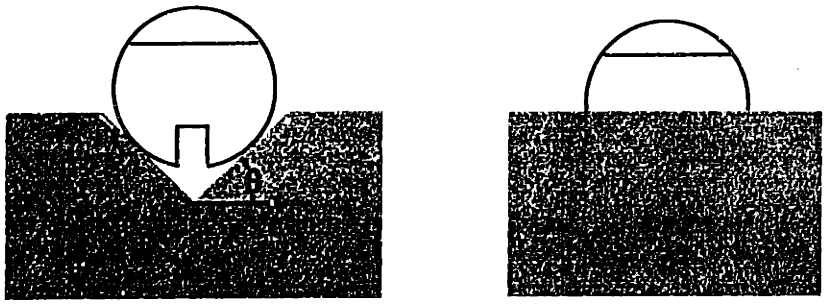

(a) (b)

Figure 4.4: Sample/setter interface configurations: (a) 1D interface; (b) 2D interface.

The 1D interface corresponds to a line contact between sample and setter. Theoretically, the interfacial area between sample and setter is infinitesimally small and the highest resistance to mass transfer is, therefore, expected. The 2D interface corresponds to the largest flat contact area possible between sample and setter. The smallest resistance to mass transfer is expected in this case. The semicircular samples were obtained by grinding the soft green ceramic articles with emery paper [Three-m-ite elek-tro-cut, cloth Jwt. 220, 3M Corp., St. Paul, MN].

The setters were received from outside suppliers as flat boards (except for the plaster setters which arrived with pre-formed grooves of angle $\theta = 60°$). These boards were convenient for the 2D interfaces but had to be machined to obtain suitable 1D interfaces. This was done using different tools depending on the toughness of the setter material. Table 4.2 shows a list of the techniques used to obtain 45° grooves in the setter materials.

Experiments aimed at measuring binder concentration gradients within the setter were performed using a Thermal Gravimetric Analyzer [TGA7, Perkin-Elmer Corp., Norwalk, CT].

Table 4.2: Machining methods and tools

Setter type	Machining technique and tool
Selee foam	Diamond grinding wheel
Plaster	None
Blasch - 20% Permeable	Diamond grinding wheel
Zircar - 70% Porous	Milling machine - 90° Multi-flute carbide bur
Blasch - 35% Permeable	Diamond grinding wheel
Zircar - 93% Porous	Milling machine - 90° Multi-flute carbide bur
Blasch - 45% Permeable	Diamond grinding wheel

4.2.3 EXPERIMENTAL PROCEDURE

The binder wicking experiments were performed at two different temperatures depending on the binder system used. Experiments involving the LV binder system were performed at a temperature of 100°C. This temperature was chosen because viscosity data obtained from outside sources referred to the green article tested at 100°C. Using the same temperature guaranteed the possibility of correlating the experimental results with the theoretical estimates obtained from the finite element model discussed in Chapter 3. The experiments involving samples with the HV binder system were performed at 120°C because of the greater viscosity of the sample. These temperatures were also chosen because they were high enough to guarantee low binder viscosity and large amounts of wicking, and low enough to prevent volatilization. Figure 4.5 shows percent binder losses vs. temperature time for samples heat treated on a porous setter (Zircar - 70% porous material) and on a non porous substrate (aluminum foil, heating rate = 1°C/min). Mass losses of the sample heat treated on the aluminum foil represent the effect of volatilization. The figure shows that, at the chosen temperatures, the amount of binder lost due to volatilization is minimal when compared to that lost through wicking.

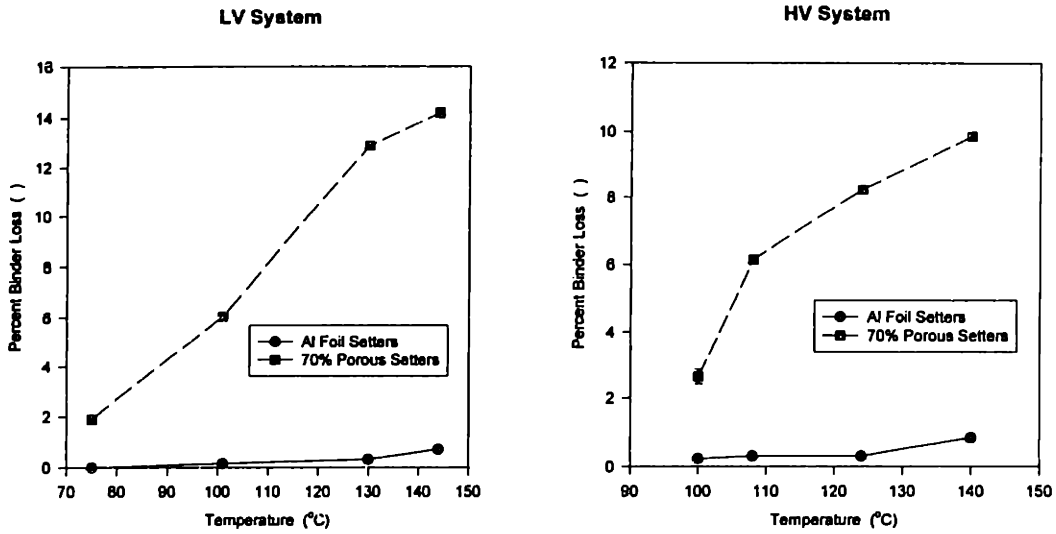

Figure 4.5: Comparison of binder loss due to volatilization and wicking into porous setter: (a) LV system; (b) HV system (1°C/min).

The experiments were performed as follows (the procedure was the same for both types of binder systems). Samples were weighed and then placed on setters; as-received green samples were placed in the groove of the machined setters, and ground semi-cylindrical samples were placed on flat, as received, setters. The samples were then inserted in the Lindberg furnace [Type 54352, Lindberg, Watertown, Wis.] and the furnace atmosphere was saturated with a pre-purified nitrogen flow to prevent binder degradation in oxygen. The furnace temperature was increased at a rate of 1°C/min to the target temperature. Once the target temperature was reached, two samples (one 1D and one 2D) were extracted and weighted. The same procedure was repeated at regular time intervals, increasing residence time as the experiment proceeded. The difference in initial and post annealing weights represented the amount binder loss due to wicking since it had been already asserted that no volatilization was taking place at these temperatures. The samples were enclosed in epoxy, sectioned, photographed, and analyzed after heat treatment as described in Chapter 3. This was done to allow for

measurement of sample distortions, which will be discussed later on in this chapter. Percent binder losses were plotted against residence times. The setters that had been used with died binder systems were sectioned and photographed to monitor binder distribution inside the setters.

Selected samples were used for TGA. In this case the samples were cut and ground to obtain cross sections of specific areas. Relative binder concentrations were obtained and compared with those in other areas of the ceramic article.

4.2.4 RESULTS AND DISCUSSION

4.2.4.1 Binder loss, interface area, and setter porosity

Figure 4.6 shows percent binder losses as a function of residence time for LV system samples distinguished between 1D and 2D interfaces. The plots have been scaled to emphasize differences between different setter types.

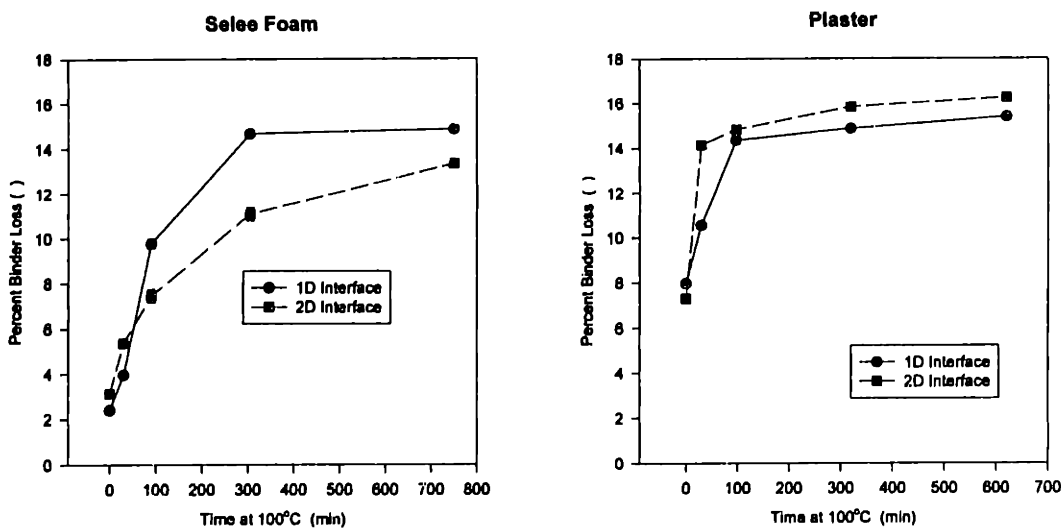

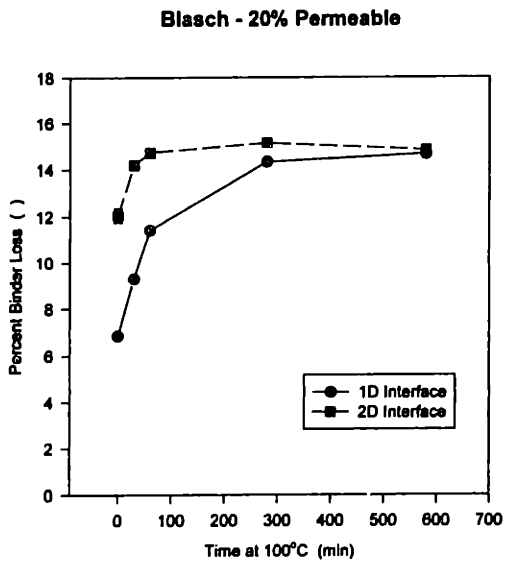
Blasch - 20% Permeable
Percent Binder Loss ( )
Time at 100°C (min)
1D Interface
2D Interface

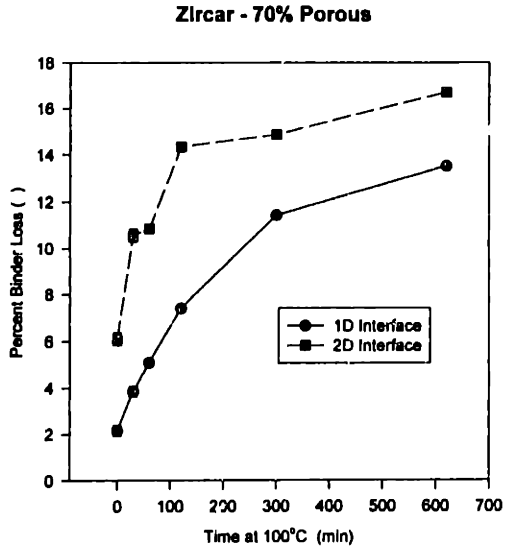
Zircar - 70% Porous
Percent Binder Loss ( )
Time at 100°C (min)
1D Interface
2D Interface

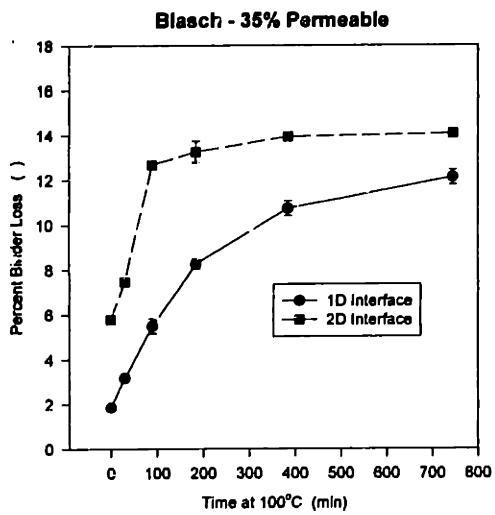
Blasch - 35% Permeable
Percent Binder Loss ( )
Time at 100°C (min)
1D Interface
2D Interface

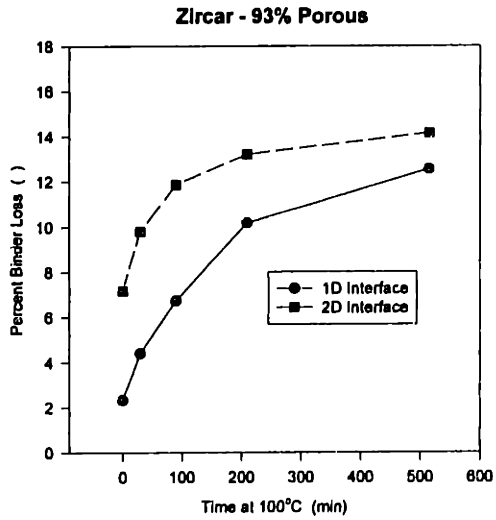
Zircar - 93% Porous
Percent Binder Loss ( )
Time at 100°C (min)
1D Interface
2D Interface

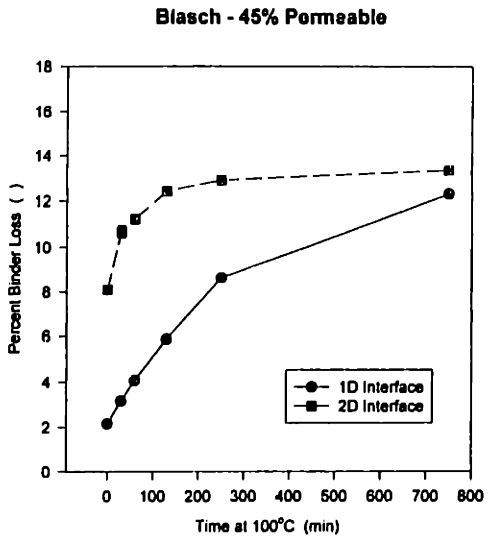

Figure 4.6: Percent binder loss vs. residence time for 1D and 2D interfaces and several setters (LV system).

Note that all plots show that there was binder loss at time zero. This is the amount of binder that was lost during the ramp up to 100°C. The plots show that, in general, the 2D interface was more effective in allowing transfer of greater amounts of binder than the 1D interface. This agrees with the idea that the theoretically infinitesimally small interface exhibits greater resistance to mass transfer than the larger interface. The difference between the amounts of binder removed are just temporary and decrease as wicking proceeds. This agrees with the idea expressed in 4.2.1 regarding saturation and capillary pressure. Both 1D and 2D interface have the same saturation once equilibrium is reached. Binder wicking ceases when equilibrium of capillary pressure is achieved.

The same types of trends can be seen for the samples based on the HV system. Figure 4.7 shows percent binder removed vs. time for these samples.

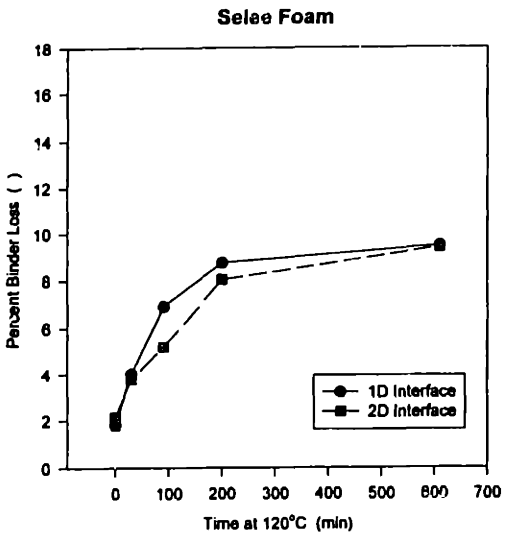
Selee Foam
Percent Binder Loss ( )
Time at 120°C (min)
1D Interface
2D Interface

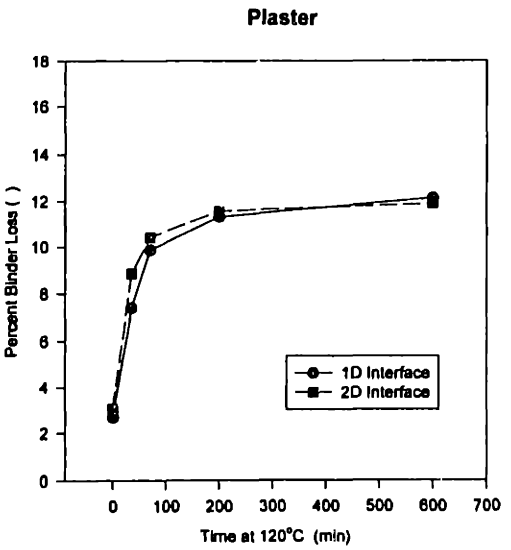
Plaster
Percent Binder Loss ( )
Time at 120°C (min)
1D Interface
2D Interface

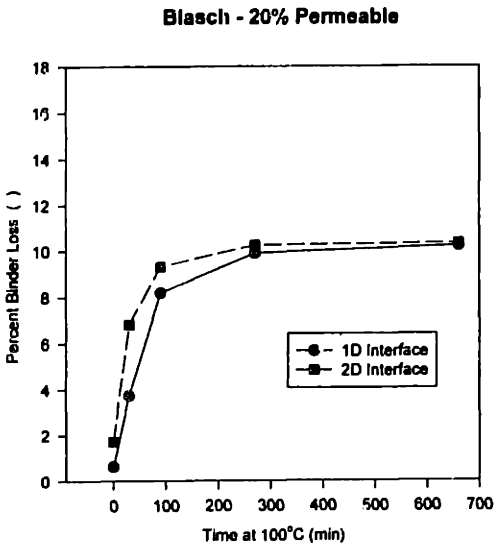
Blasch - 20% Permeable
Percent Binder Loss ( )
Time at 100°C (min)
1D Interface
2D Interface

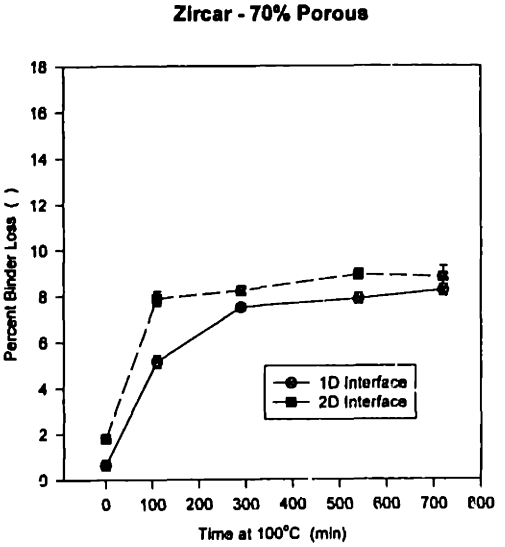
Zircar - 70% Porous
Percent Binder Loss ( )
Time at 100°C (min)
1D Interface
2D Interface

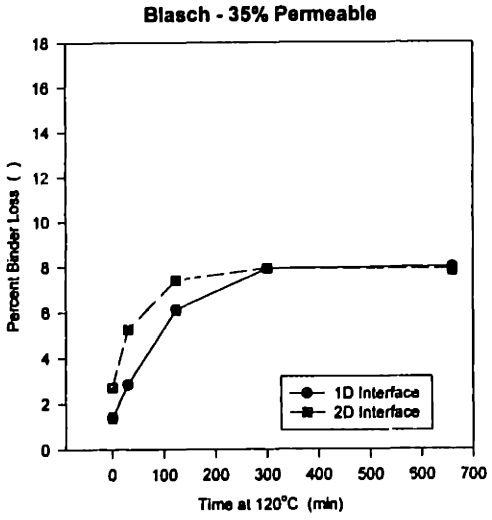
Blasch - 35% Permeable
Percent Binder Loss ( )
Time at 120°C (min)
1D Interface
2D Interface

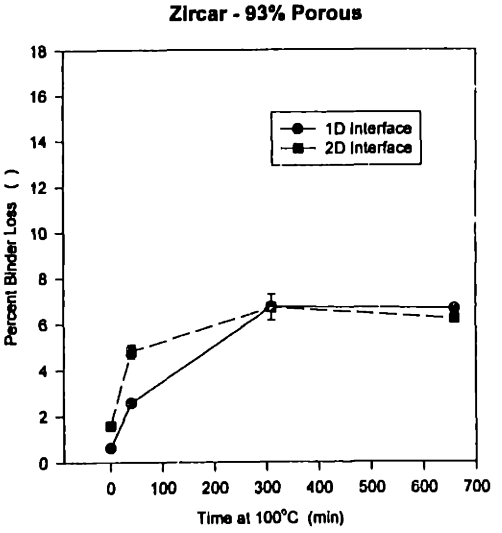
Zircar - 93% Porous
Percent Binder Loss ( )
Time at 100°C (min)
1D Interface
2D Interface

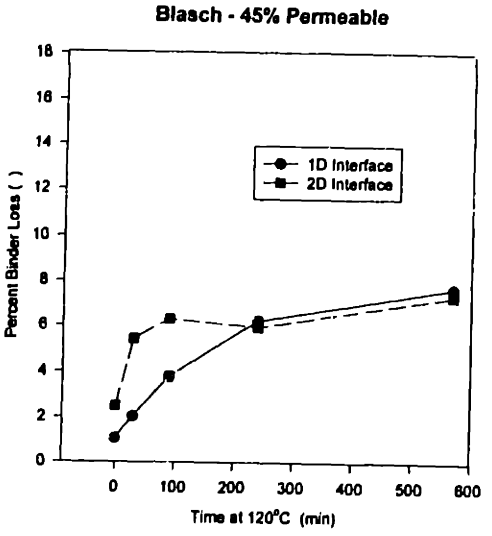

Figure 4.7: Percent binder loss vs. residence time for 1D and 2D interfaces and several setters (HV system).

The HV system samples show, as expected, larger amounts of binder loss for the 2D interface samples. Both types of binder systems show, however, an interesting behavior regarding binder loss with Selee Foam setters. With these setters the 1D interface samples lost considerably more binder than the 2D samples. This is contrary to expectation and the evidence gathered with other setter materials. Only after SEM analysis of the setter microstructure it is possible to understand the reason behind this particular behavior. Figure 4.8 shows two SEM images of the unmachined flat surface corresponding to the 2D interface, and the machined surface corresponding to the 1D interface in Selee Foam material.

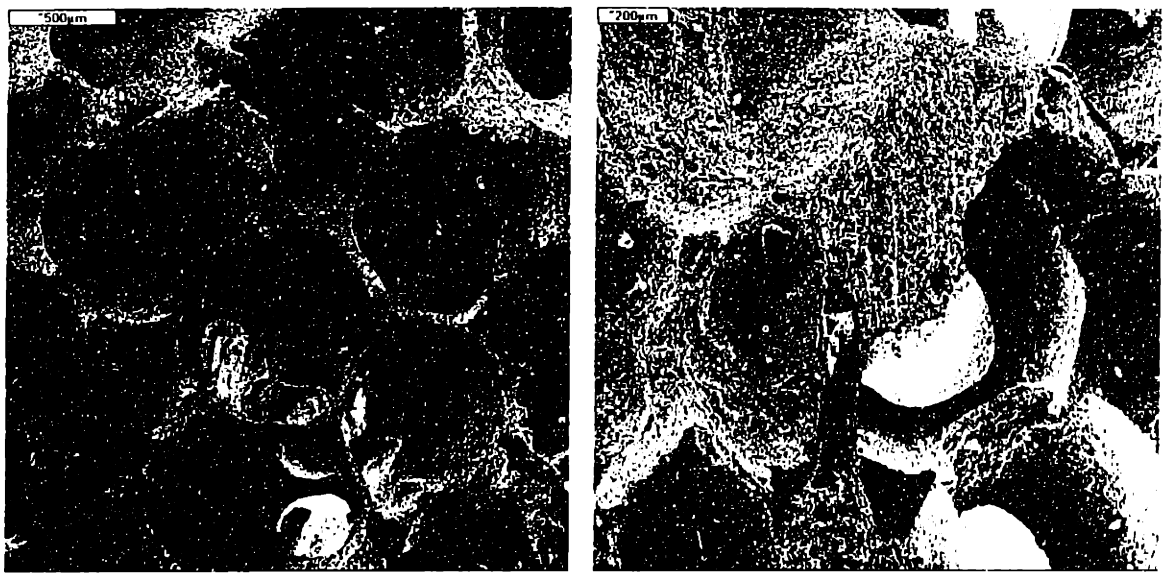

(a) (b)

Figure 4.8: Microstructure of Selee Foam setter: (a) unmachined surface corresponding to 2D interface; (b) machined surface corresponding to 1D interface.

Figure 4.8(a) shows the unmachined surface corresponding to the 2D interface. 2D interfaces are characterized by widespread, pore rich, contact areas which facilitate mass transfer between sample and setter. The surface shown in Figure 4.8(a), however, does not show this type of large flat surfaces. On the contrary, this surface is characterized by sparse peaks between large pores. This has a dual effect on binder removal. First, the nature and non-continuity of the contacts inhibits rather than facilitate binder transfer since they correspond to point contacts rather than 2D interfaces. Second, the limited number of small pores and the presence of very large pores that exert little capillary pressure, reduces the extent of the suction force on the setter. The machined surface shown in Figure 4.8(b), however, shows many of the features that would be expected in a 2D interface surface. Along the walls corresponding to the 1D interface contact points large flat surfaces can be seen. These surfaces represent good contact points with the green article surface. The flat features are also rich in very small pores which exert strong capillary pressure on the sample. The photograph has been taken at a larger magnification to emphasize these structures. These factors explain the greater extent to which the 1D interface was capable of removing binder. The unpredictable

behavior described here stresses the importance of not limiting setter analysis and characterization to techniques for evaluating porosity distributions. It is extremely important to study and analyze setter microstructure as well.

Figure 4.9 shows comprehensive plots of total amount binder loss vs. setter pore size. Both types of interfaces, 1D and 2D, have been identified as well as different binder systems.

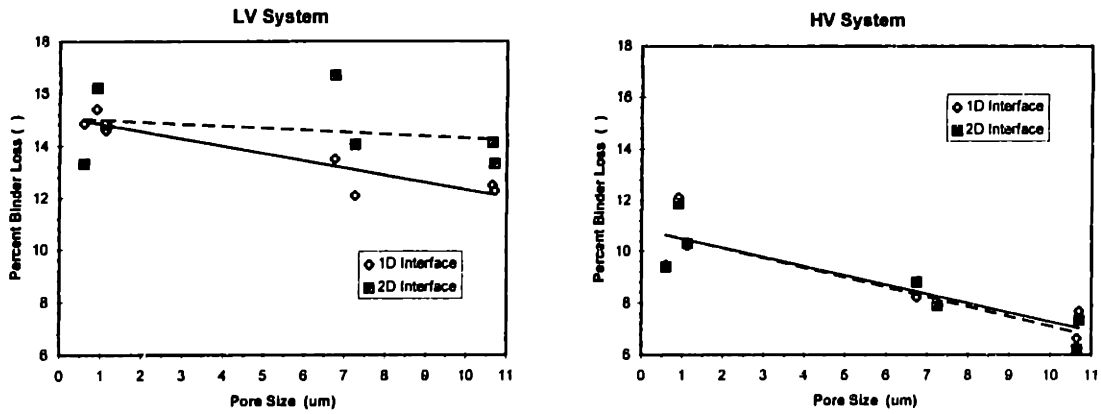

Figure 4.9: Percent binder loss vs. pore size.

The figure shows that the amount of binder wicked from the samples decreases as pore size in the setter increases. This trend is visible for both types of interfaces and binder systems and agrees with the expected trend. The plot also shows considerable difference between the amount of binder lost by LV and HV type samples. This may be explained by considering the surface tension of the two binder systems. This information is not available at this time so no conclusive remarks can be made.

The information gathered with these experiments allows us determine whether the sample is undergoing densification or creating new pores as binder is removed. Figure 4.10 and Figure 4.11 show a comparison between the volume loss of the sample calculated from weight data and the volume loss calculated from image analysis by measuring changes in the cross-sectional area of the samples.

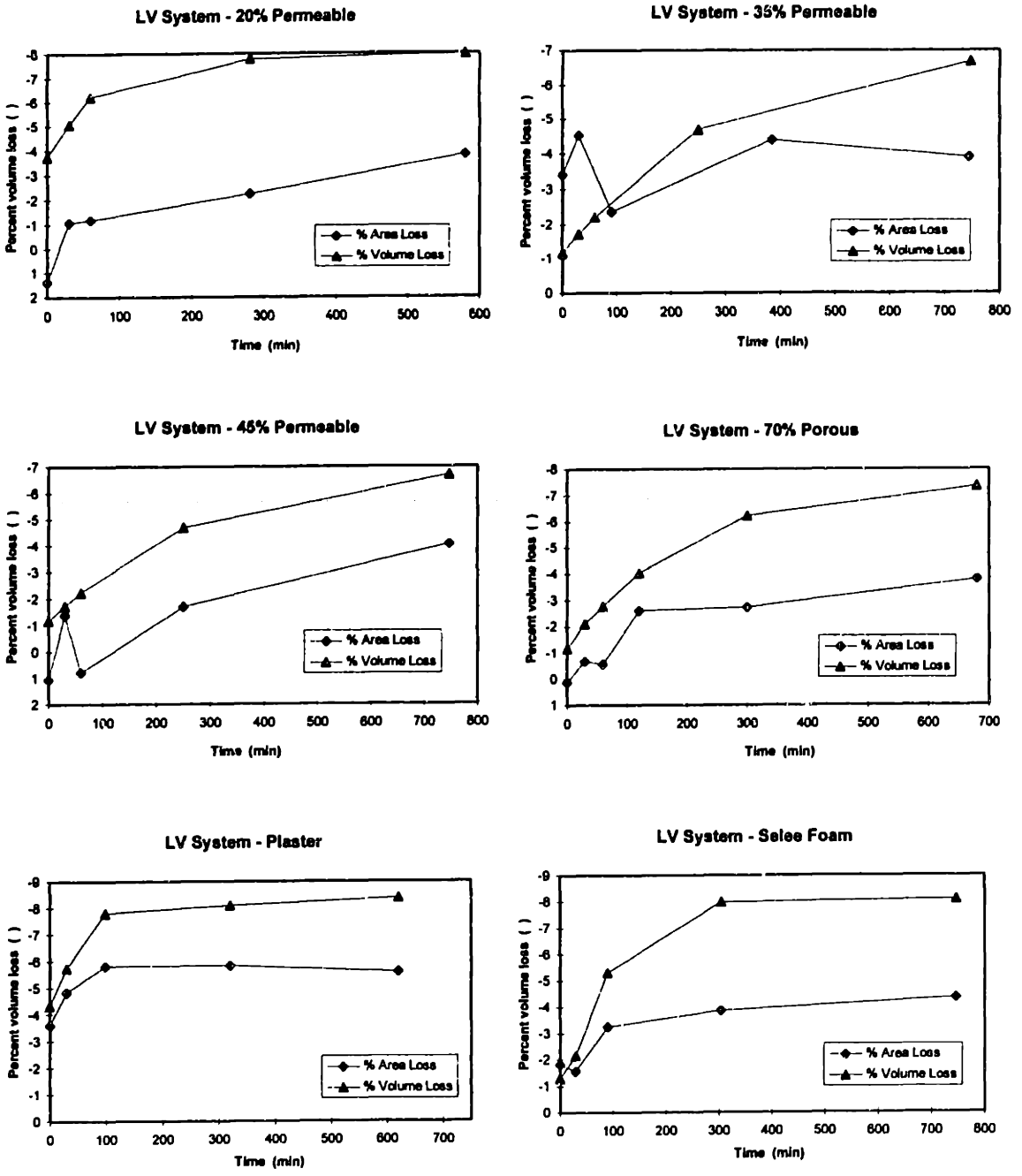

Figure 4.10: Comparison between volume losses calculated from weight loss information and from cross-sectional area measurements (LV - System).

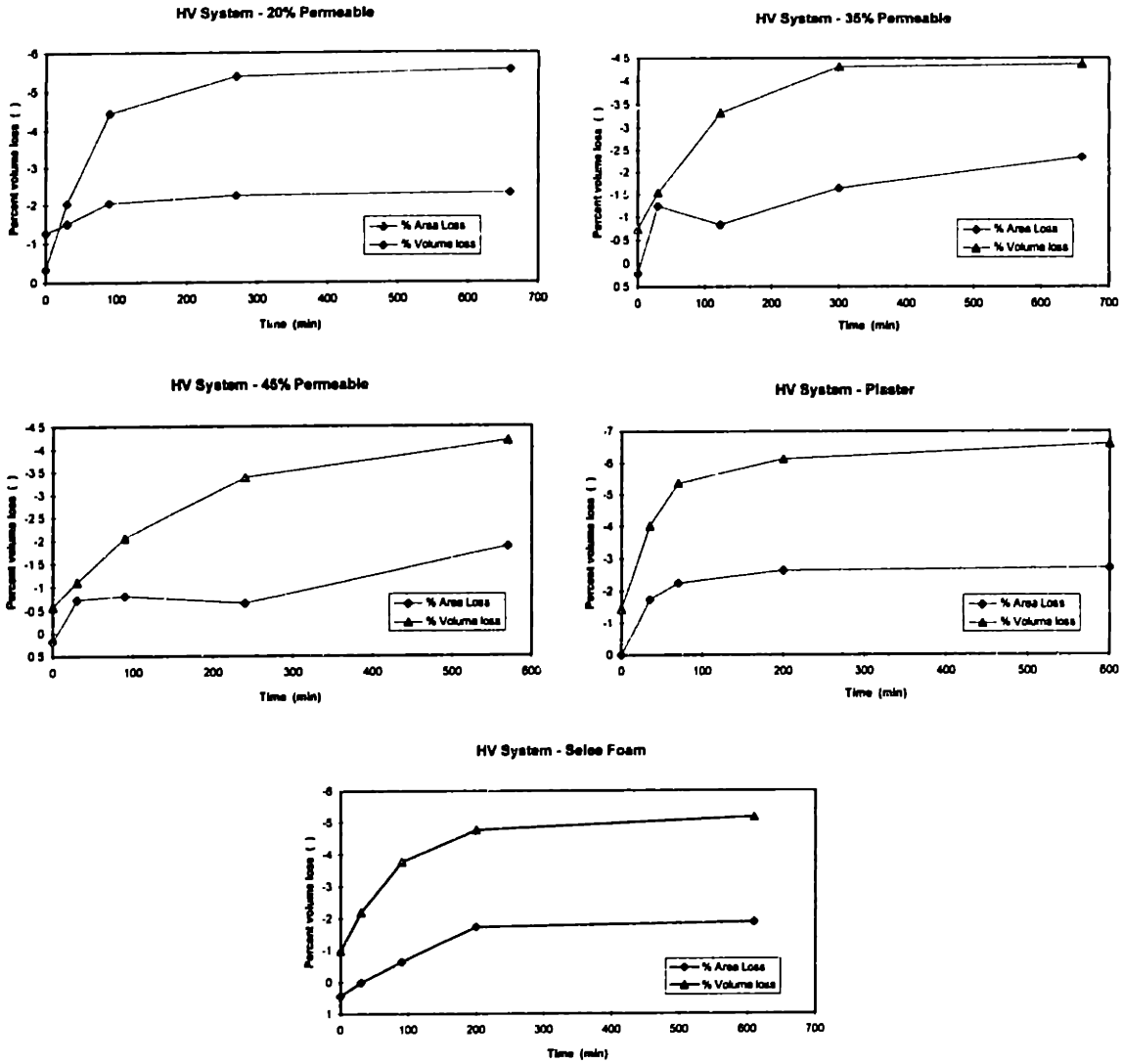

Figure 4.11: Comparison between volume losses calculated from weight loss information and from cross-sectional area measurements (HV - System).

The plots show that, in general, the volume loss obtained from weight loss calculations is greater than the actual volume loss measured in the sample. This means that pores were created in the sample during heat treatment. The difference between experimental and theoretical volume changes was greater for the HV system samples. This is expected because particle redistribution and densification is more difficult with highly viscous binders. This information is important because it confirms that the decreased saturation causes increased resistance to binder flow, and, therefore, much lower binder removal rates. Pores are generated because of binder depletion. The

location and distribution of these pores is, however, not available from the data obtained with the previous experiments.

Uneven binder distribution was, however, confirmed by TGA of selected sample areas. TGA (10°C/min up to 450°C, 5°C/min to 550°C) on samples heat treated for twenty minutes on plaster and 70% porous setters showed that upper portions of the sample had higher binder content than areas closer to the interface. For example, upper portions of LV system samples heat treated for 20 minutes on plaster setters had a volume fraction of binder of 0.526 while lower portions had a volume fraction of binder of 0.493 (assuming a particle packing factor of 0.46). The sample showed a total binder loss before TGA of 5.4%. The same heat treatment on Zircar - 70% Porous setters gave an upper volume fraction of binder of 0.533 vs. a lower one of 0.517 (binder loss prior to TGA was 2.1%). This confirms that those portions closer to the sample/setter interface were depleted of binder faster than more isolated areas and that this took place very early during the binder removal process. TGA was performed on the HV system samples heat treated for the same amount of time on Plaster setters. The volume fraction of binder in the upper part of the sample was 0.531 vs. 0.519 in the lower part (binder loss was 2.0%). TGA on the same type of samples heat treated on 70% porous setters lead to upper binder volume fractions of 0.533 vs. 0.529 in the lower part (binder loss was 1.0%). Pore formation was also confirmed, as seen earlier, by dimensional change results.

4.2.4.2 Binder distribution within setters

Part of theses experiments consisted in the qualitative monitoring of binder distributions within setters. Figure 4.12 shows three different views of binder distributions inside a porous setter.

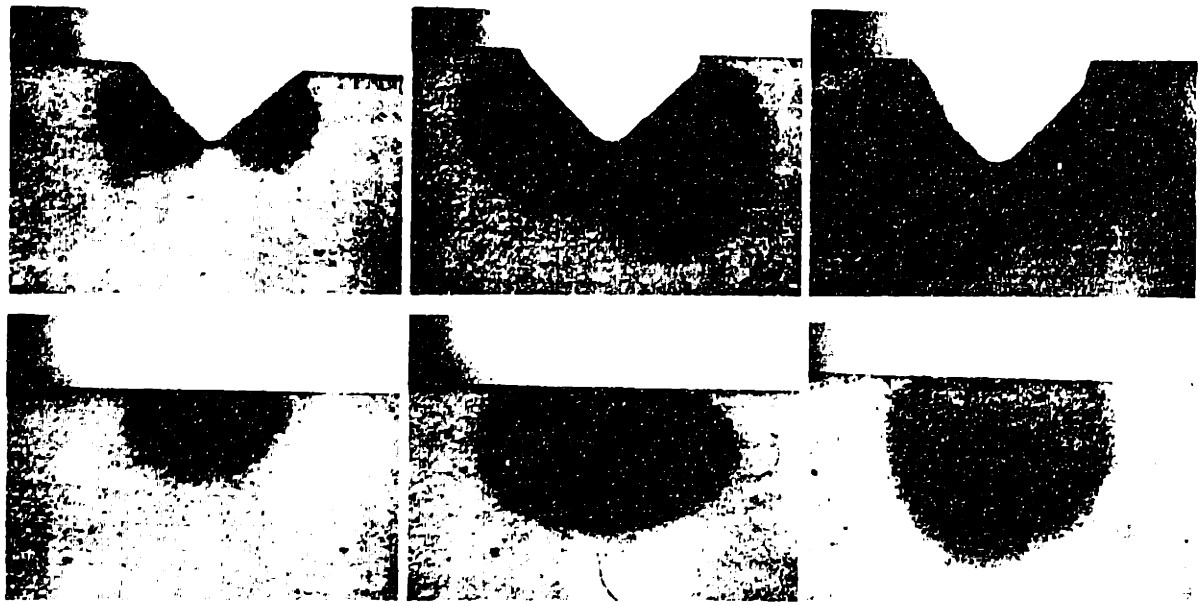

Figure 4.12: Binder distribution within Blasch - 20% permeable setters at three different times during heat treatment (LV system).

This type of distribution was similar to that encountered in other types of setters for samples with the same binder system. There was a relatively uniform distribution of the binder across a fairly widespread area within the setter. However, wetting properties of the binder played an important role in influencing binder distribution within the setter. Figure 4.13 shows binder distributions in the same type of porous setter as in Figure 4.12 but for the HV binder system.

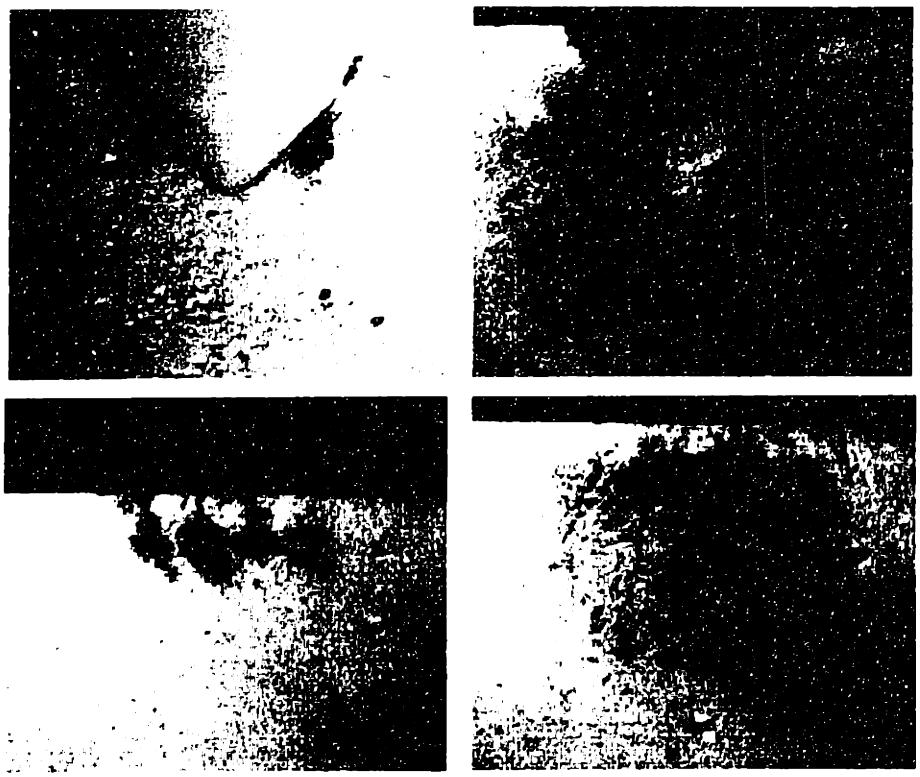

(0 min) (660 min)

Figure 4.13: Binder distribution within Blasch - 20% permeable setters at two different times during heat treatment (HV system).

In this case the binder distribution in the setter is not as homogeneous as with the LV system. The edges of the binder traces are not clearly defined as well. These differences in binder distributions can be attributed to different wetting properties and viscosities of the two binder systems. Once again, however, no information is available on the subject.

An interesting phenomenon that could have interesting practical consequences was the anisotropic binder distributions within Zircar 93% porous setters. These setters are manufactured by stacking and compressing beds of fibers. These fibers are stacked approximately in horizontal and they confer a definite anisotropy to the material. This anisotropy affects the distribution of binder in the setter which migrates preferentially along channels created between fibers. Figure 4.14 shows binder traces in two setters

that have been machined in such a way that fibers lay preferentially in the horizontal direction in one case, and in the vertical direction, in the second case.

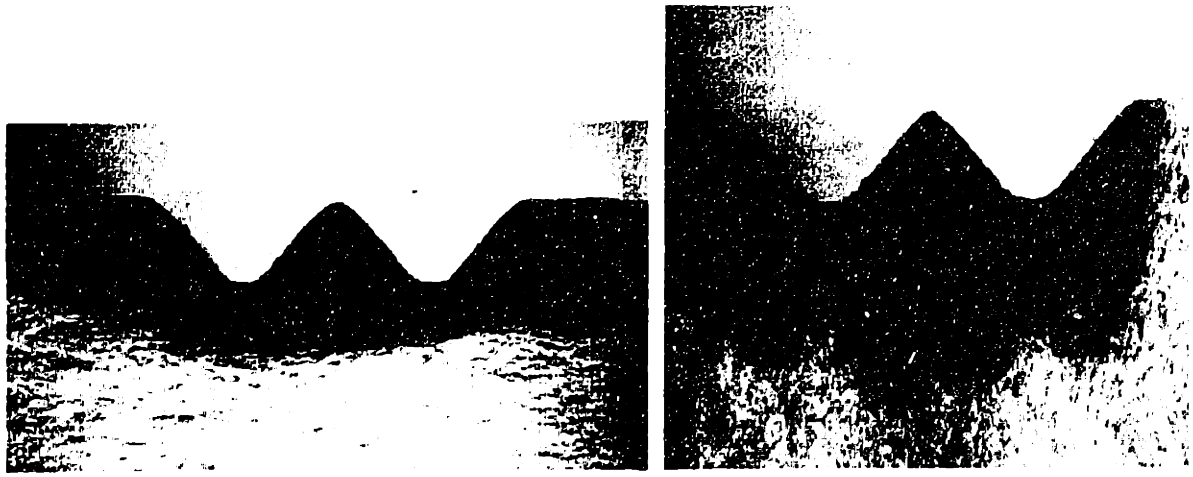

(a) (b)

Figure 4.14: Binder distribution in Zircar - 93% porous setters machined to obtain preferential fiber orientation in (a) horizontal direction and (b) vertical direction (LV system).

The preferential direction of migration of the binder is quite pronounced in both cases. This phenomenon could have important consequences in operations involving large production runs. One of the factors determining the required distance between samples in a setter is interference of the binder traces within the setter. Considerable overlapping of the traces within the setter could influence wicking of binder by saturating setter pores. Distances between samples are therefore chosen so that minimal or no interference occurs. The relatively large distances existing between samples reduces sample density per furnace, which in turn increases production costs. Distances between components can be reduced by designing the setter with a preferentially vertical fiber orientation since binder migration in the horizontal direction is very limited. This could potentially increase the density of samples per setter, allowing larger, more economical production runs.

4.2.5 CONCLUSIONS

The relationship between setter porosity, interface geometry, and amount binder removed was explored. Setters with the smallest pore sizes exerted greater capillary pressure and were more capable of removing binder from the sample. This trend was found for both types of binder systems, LV and HV. Large, flat interface areas allowed greater amounts of binder to be removed during the earlier stages of heat treatment. Generally this meant that 2D interfaces performed better than 1D interfaces. However, an exception was found for setters in which the unmachined flat surface offered few contact points and had relatively large pores. In this case, the machined 1D interface performed better because of the presence of large flat structures rich in small pores. This unexpected result confirmed the necessity of performing in depth analysis of setter micro structures to predict binder removal behavior.

Experimental evidence was found proving that, during binder removal, pore formation rather than densification of the article was taking place. TGA allowed to measure considerable difference in binder content between upper and lower areas of the samples. The lower areas, closer to the interface, were depleted of binder to greater extent than upper portions of the samples.

The distribution of binder within setters was also analyzed. It was found that binder distributions are strongly influenced by the wetting characteristics of the binder system. Good wetting lead to fairly homogeneous binder traces while poor wetting lead to spottier and, in general, less homogeneous binder distributions. It was also observed that, within setters, binder migrates according to fiber orientation. This was visible in the Zircar 93% porous material.

Important lessons were learned about the effect of setter porosity and interface geometry on the total amount of binder removed from the green sample. However, more remained to be learned about the influence on binder removal rates and binder flux. The

experiments described in the next section were designed to investigate this important aspect of the binder removal process.

4.3 BINDER REMOVAL RATE AND BINDER FLUX

4.3.1 INTRODUCTION

The previous section focused on the relationship existing between the total amount of binder removed, setter microstructure, and interface geometry. It is known that sample distortions can be greatly reduced by maximizing the amount of binder removed during the very early stages of heat treatment, when the binder system liquefies and looses structural support. This means that a complete analysis of the relationship existing between binder removal, setter microstructure, and interface geometry should also focus on the correlation with binder removal rates.

It has been established in the previous section that interface geometry strongly controls the amount of binder removed from the sample, especially in the early stages of binder removal. The 1D interface, corresponding theoretically to a line contact between sample and setter, offered higher resistance to mass transfer than the widespread 2D interface. This was shown by the different amounts of binder removed as a function of time. This implies that the rate of mass transfer is higher for the 2D interface than the 1D interface. This result raises some questions. Theoretically, the 1D interface corresponds to a line contact between sample and setter. A line interface should not allow any mass transfer. The interface has a finite thickness in reality, but this is still considerably smaller than the 2D interface. The binder removal rates of the 1D interface were, however, within the same order of magnitude of those of the 2D interface. Much lower binder removal rates should have been expected if binder removal rate were

directly proportional to contact area, suggesting that binder transfer rate and binder flux vary non-linearly with area.

The two contact areas described in the previous section represent the maximum and minimum limits of mass transfer resistance. Other interfacial area sizes need to be tested to determine the relationship between binder removal rate and flux with changing area. The binder migration distances inside the green heated samples need to be considered as well. Highly viscous binders will offer greater resistance to flow within the sample. For a description of the equations governing this flow see section 4.2.1.

In this section, binder removal rates and binder flux are described. The dependence of these to setter characteristics and binder type is explored. The onset of binder concentration gradients within the setter due to localized binder removal is also studied.

4.3.2 Materials and Methods

The setters used in this series of experiments are the same as those described in the previous section. Machining techniques and tools were also the same. Samples had the same two types of compositions described previously. Their shapes included however several shapes not included in earlier experiments. Figure 4.15 shows a sequence of samples used in these experiments with the corresponding interfacial areas in mm^2. These samples were designed to obtain intermediate interfacial areas between the 1D and 2D interfaces. They were obtained by grinding the green sample with emery paper [Three-m-ite elek-tro-cut, cloth Jwt. 220, 3M Corp., St. Paul, MN] until the desired shape was obtained.

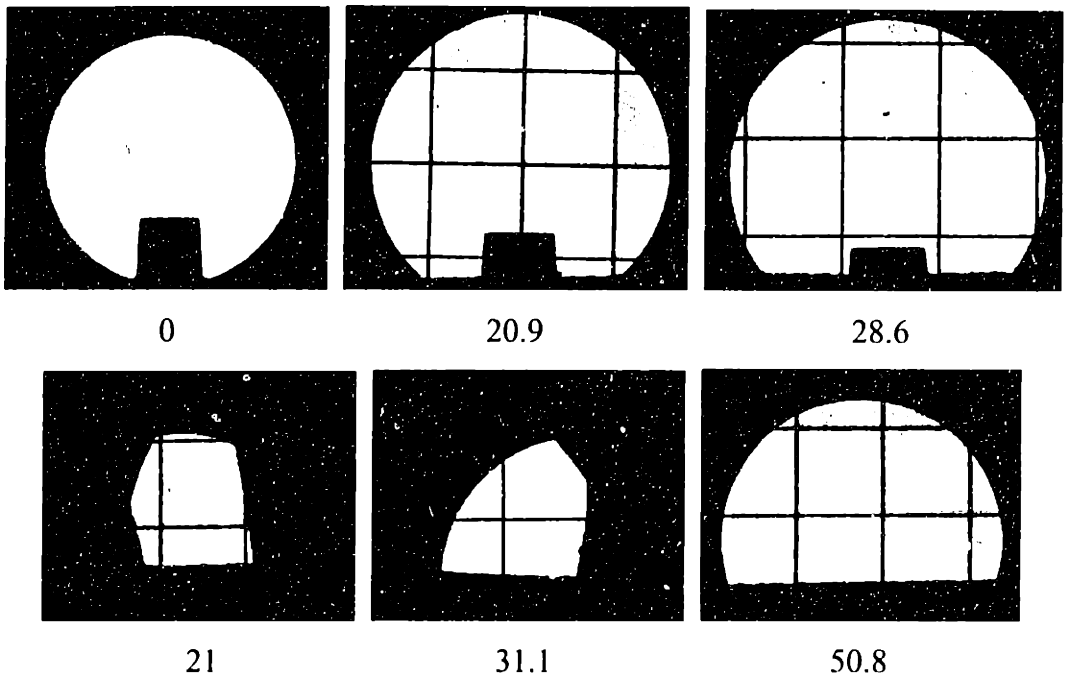

Figure 4.15: Cross sections of green samples prior to heat treatment with corresponding interfacial areas.

4.3.3 Experimental Procedure

These experiments were designed to obtain accurate binder removal rates as a function of interface area. Previously, green samples had been inserted in the furnace prior to initiating the heating ramp. Some binder loss was always experienced between room temperature and the desired target temperature. The new type of experiment, however, consisted in inserting the sample in a preheated furnace. This way, the mass loss between room and target temperatures was not observed. The sample was taken out of the furnace after a predetermined residence time, quenched in air, and weighted to monitor mass losses. The same sample was then reintroduced in the furnace and the cycle repeated. Figure 4.16 shows a schematic of the heat treatment cycle.

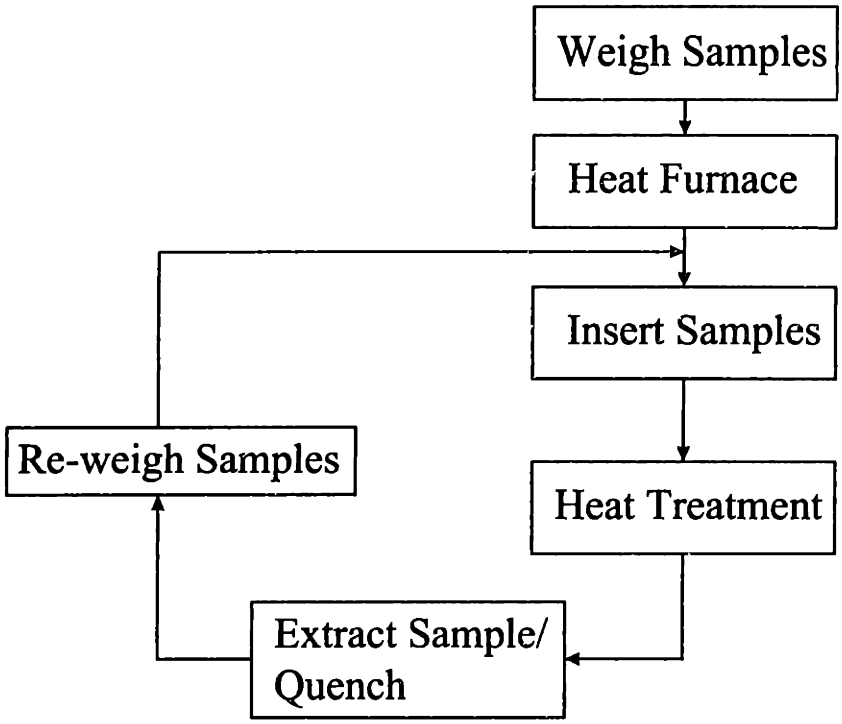

Figure 4.16: Procedure used in binder removal rate experiments.

Despite the difference in procedure, the mass losses were quite similar to those obtained in previous experiments. This is shown by Figure 4.17 which is a comparison between binder losses in a LV system sample obtained with the old and new heat treatments. The figure shows minimal differences between the two samples except for the percent binder loss at time zero. This discrepancy is due to the fact that in the old experimental technique, time zero, referred to the time at which the sample reached the target temperature.

Samples were enclosed in epoxy after heat treatment, sectioned, polished, photographed and their interfacial areas measured using an image analysis program, as described earlier.

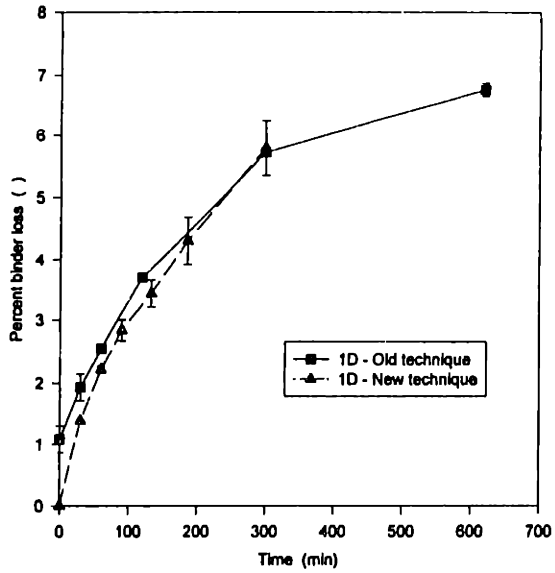

Figure 4.17: Comparison between binder losses obtained in a LV system sample on a 70% porous setter at 100°C with the old and new experimental techniques.

4.3.4 RESULTS AND DISCUSSION

Figure 4.18 shows percent binder losses as a function of time for different types and sizes of interface areas. In the legend, 1D refers to the smallest area, 2D to the largest, and all the areas in between are in increasing order (similar to those shown in Figure 4.15).

The slopes of the curves shown represent the binder loss rates. Generally, as the interface area increases the binder removal rate increases. The HV system samples show greater variability and don't follow the trend as well. This can be explained by poorer contact between sample and setter. Because of their greater viscosity, these samples were less likely to conform to the setter surface and create good contact with pores in the setter. Poor contact was due to natural irregularities in the setter surface and the lack of a perfectly flat surface in the sample.

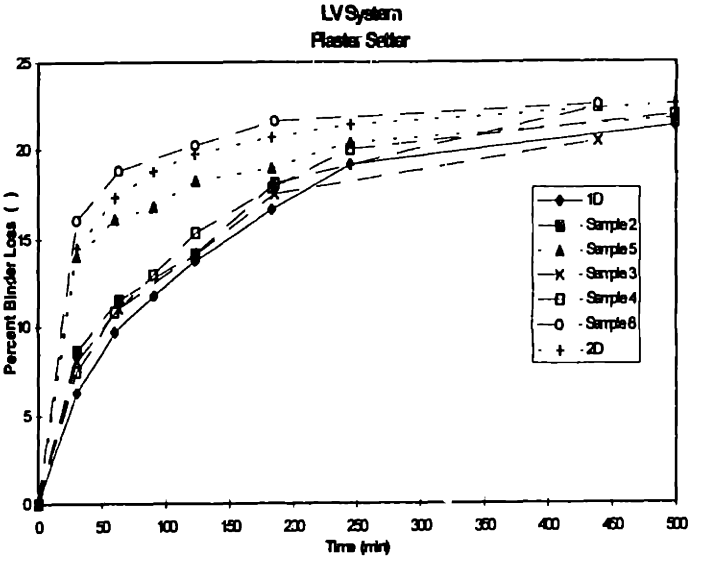

(a)

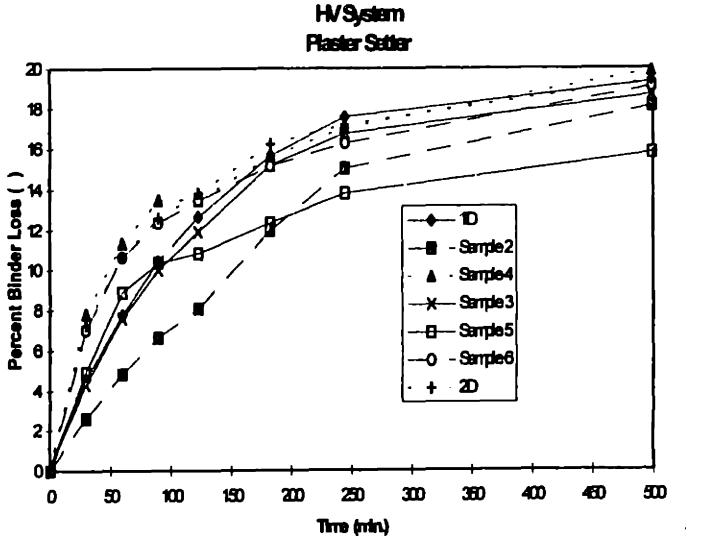

(b)

Figure 4.18: Percent binder loss as a function of time and interface size for samples on plaster setters: (a) LV - system; (b) HV - system.

The increase in binder removal rate with increasing contact area suggests that, as expected, larger interfacial areas offer less resistance to binder transfer than smaller areas. The same trend was seen on Zircar 70% porous setters. For this type of setter,

Figure 4.19 shows binder removal rates as a function of time for 1D and 2D interfaces together with power curve fits. The difference between 1D and 2D interfaces is dramatic. It is also possible to see that while there is considerable difference between the 2D binder removal rates of the two binder systems, there curves relative to the 1D interface are almost coincident. This suggests that the controlling mechanisms for binder transfer are different for the two types of interfaces. Binder transfer through the 1D interface is controlled by the very limited size of the contact area. Binder transfer through the 2D interface is controlled by the hydraulic resistance to mass transfer which is greater for the HV binder system.

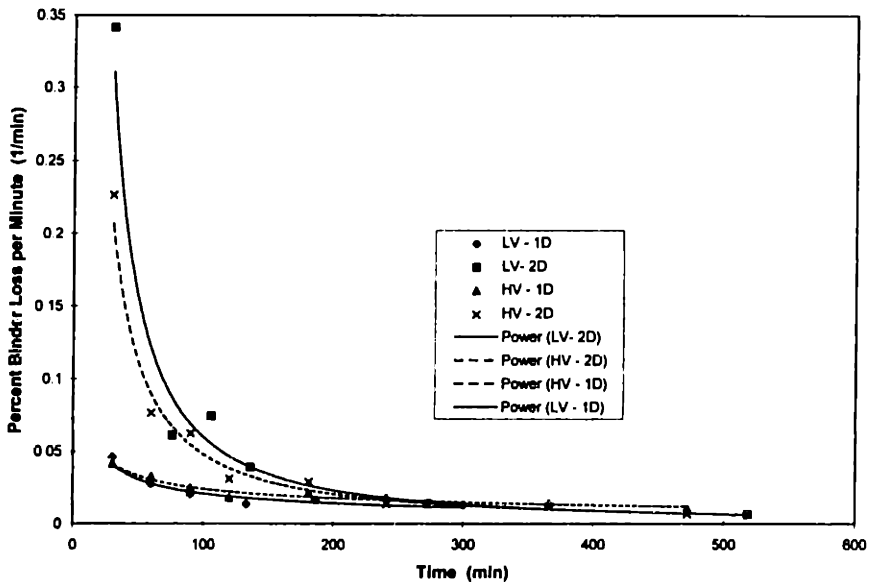

Figure 4.19: Binder removal rate vs. time for two interface types and both binder systems.

Greater insight on the mechanics of binder transfer can be obtained by calculating binder flux and plotting them against interface area. Figure 4.20 shows binder flux as a function of interface area. The sample cross-sections are also shown for clarity. Flux is mass transfer normalized with respect to interfacial area. Therefore, if flux were independent of interfacial area, a constant value would be obtained. However, Figure 4.20 shows that flux varies non linearly with interfacial area.

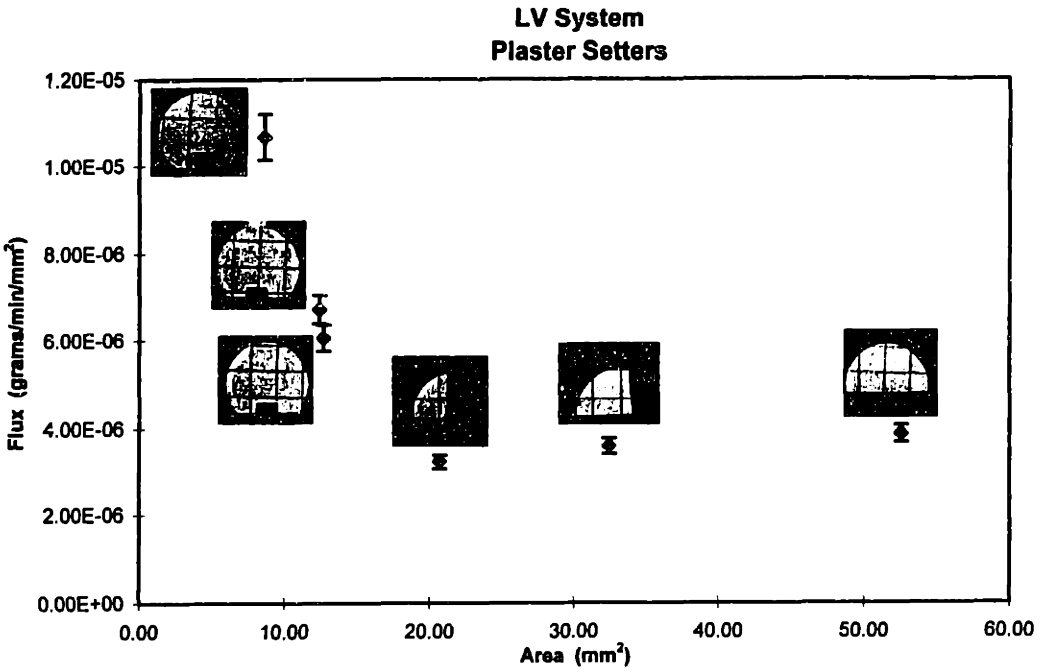

(a)

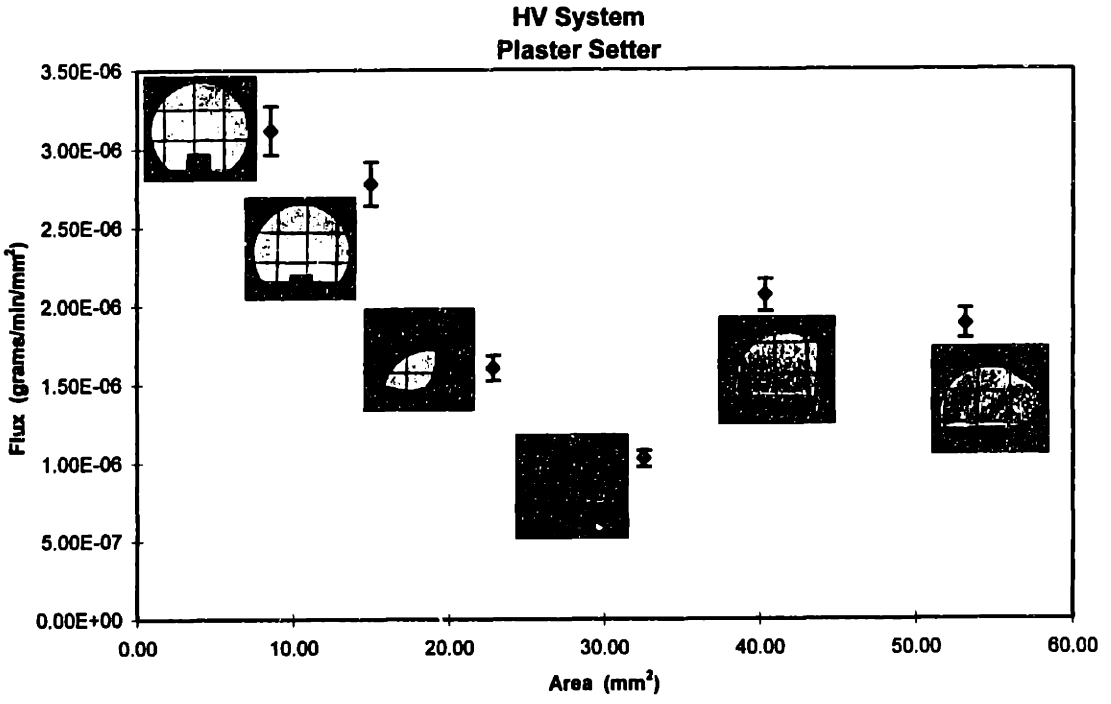

(b)

Figure 4.20: Binder flux vs. interface area: (a) LV - system; (b) HV - system.

Binder flux seemed to decrease rapidly as interfacial area increased and then acquired a somewhat constant value. This can be explained only by considering the migration distance in the samples. It was argued that binder flux depended upon the length scale of the migration distance to the interfacial area. Now that binder flux information is available, it is possible to calculate the required pressure gradient to remove binder from the sample by using equation 1. The permeability factor, k, can be calculated from equation 1: using $\beta = \pi/6$ (for spherical particles), d = 1.35 μm (particle diameter in the sample), ε = .54 (green sample), and $\lambda = 3\pi$ (for a sphere in an infinite fluid, fully saturated medium), k results equal to 6.4184E-14 m^2. Using a relatively low value for the flux from the experimental data, such as $4x10^{-6}g/mm^2/s$ and a fluid viscosity η = 0.223Pa-sec (Polyethylene @ 125°C, Aldrich Catalogue # 19191-4), it is possible to calculate the required pressure drop for a characteristic length of 3mm (approximately the diameter of the sample). The pressure drop ΔP results equal to $4.17x10^7$Pa. The suction pressure exerted by the setter on a fluid with a surface tension of 0.03Pa, is $1x10^5$ Pa (Selee Foam, d = 0.6μm). This pressure is several orders of magnitude smaller than the pressure required to pull binder from the top to the bottom of the sample. The same calculation performed with Paraffin Wax as the binder system (η=0.0027PA-sec, Aldrich Catalogue # 32,720-4) gives a required pressure drop of $5.05x10^5$Pa. This means that binder is pulled only from the areas adjoining the sample/setter interface, where the migration distances are small.

This calculation also explains why a reduction in binder flux is experienced as interfacial area increases. The migration distance involved in three typical samples can be seen in Figure 4.21.

The migration distances in each of the samples is symbolized by the arrows. Moving from left to right, the area of the sample increases and so does the distance the binder needs to cover to reach the interface area. It is difficult for the setter to "pull" binder from areas relatively far from the interface since a large hydraulic resistance needs to be overcome.

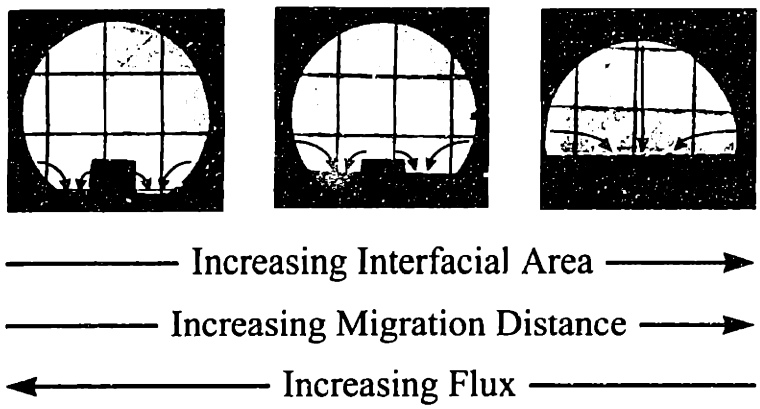

Figure 4.21: Relationship between interfacial area, migration distance, and binder flux.

This means that the center of large interface areas is the locus of little binder transfer. Binder is exchanged from the sample to the setter near the edges of the sample, where migration distances and hydraulic resistances are small. The consequence is that, overall, flux decreases as interfacial area and migration distance increase. Of course, binder removal rates are still higher for larger areas because the increase in area overcomes the decrease in flux. Finally, the flux of binder seems to level off in the three samples with the larger interfacial areas because, in these cases, the migration distance is the approximately same for all of them and it is dictated by the thickness of the sample.

4.3.5 CONCLUSIONS

Binder removal rates were examined against two binder viscosities and several interfacial areas. It was found that binder removal rates were dependent on interfacial areas, that is, larger areas led to higher binder removal rates. This trend was found in all samples and for all tested setters. However, removal rates seemed to be controlled by two different mechanisms depending on whether transfer was taking place through a line contact or through a large surface. The resistance opposed by the theoretically infinitesimally small area was the controlling element in the former case, while in 2D interfaces, binder removal rate seemed to be more directly related to binder viscosity.

Proof was obtained that binder flux is dependent upon migration distance and interfacial area. The mechanism controlling binder flux was understood. Binder flux depended predominantly on migration distance due to the hydraulic resistance that must be overcome by the setter in order to remove binder. Large interfacial areas need to be located close to suitable sources of binder (open sample surface to the atmosphere) to be completely effective.

4.4 BINDER REMOVAL AND DEFORMATIONS

4.4.1 INTRODUCTION

The rate of deformation of samples heat treated over non porous setters was studied experimentally and through the aid of a final element model in Chapter 3. These deformations originate from gravitational forces and are due to the loss of structural support from the binder system upon liquefaction. Good agreement was found between the experimental results and the theoretical predictions. However, deformation due to slumping are only one type of distortion that can take place in the sample. Distortions can also arise due to phenomena related to binder removal.

The viscosity of the sample depends on the amount of binder present. Higher amounts of binder mean lower viscosity. Uneven binder distributions can create areas of different viscosity within the sample. The deformation of the sample will then depend on the interaction between regions of different viscosity.

The deformations occurring on samples heat treated on different types of setters are analyzed in this section. These distortions are compared with those of samples heat treated over non porous setters to understand the effect of binder removal on the creep behavior of the ceramic article. Finally, binder distributions within the heat treated sample are related to sample distortions.

4.4.2 MATERIALS AND METHODS

The samples used in this series of experiments were the same ones described previously and so were the setters. Only full, non-ground, samples were analyzed for deformation. These samples have specially designed features that serve as useful reference points when measuring deformations.

4.4.3 EXPERIMENTAL PROCEDURE

The samples were heat treated as described in section 4.2.3, enclosed in epoxy, sectioned, photographed, and measurements were made using an image analysis software [Sigma Scan, Jandel Corp., San Rafael, CA]. Measured distortions were plotted against residence times and binder removal rates [Sigma Plot, Jandel Corp., San Rafael, CA].

4.4.4 RESULTS AND DISCUSSION

Figure 4.22 shows the cross sections of two samples before and after heat treatment.

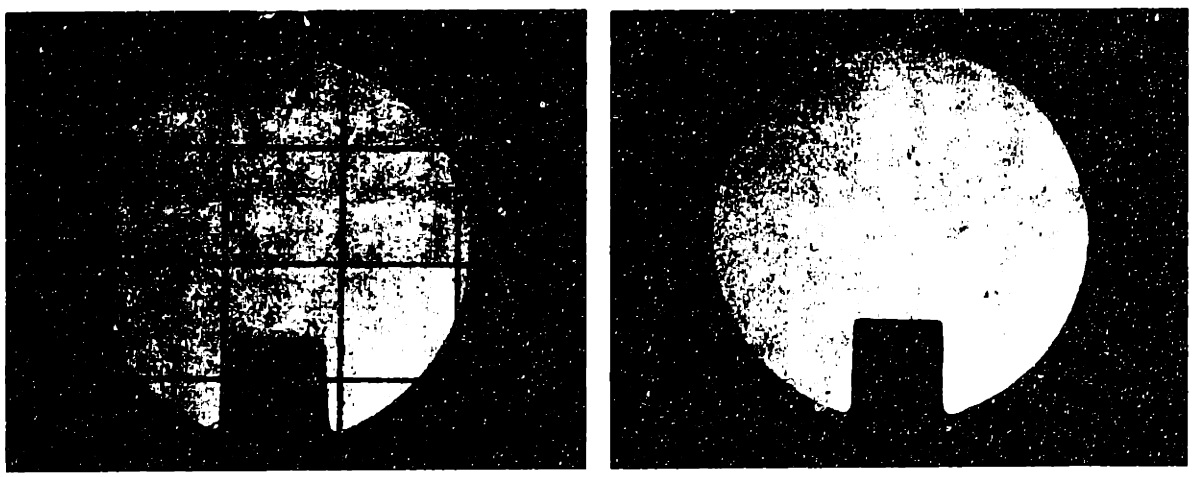

(t = 0 min) (t = 747 min)

Figure 4.22: Cross-sections of two samples before and after heat treatment (LV - system, 45% Permeable setters, not to scale).

The most striking difference between the two cross-sections is the contraction of the bottom groove. At time zero, the groove appears as it has actually been designed, with a slight taper to facilitate mold extraction. In the post-heat treatment sample, however, the

taper in the groove has disappeared. This means that the groove has effectively contracted.

This result is opposite to what was obtained experimentally and with the finite element model. It was described earlier that in both cases the groove of a sample heat treated over a non-porous setter actually expanded instead of contracting. This suggests that binder removal has an effect on shaping the final heat treated article. The result shown above was encountered in all combinations of samples and setters as shown in Figure 4.23.

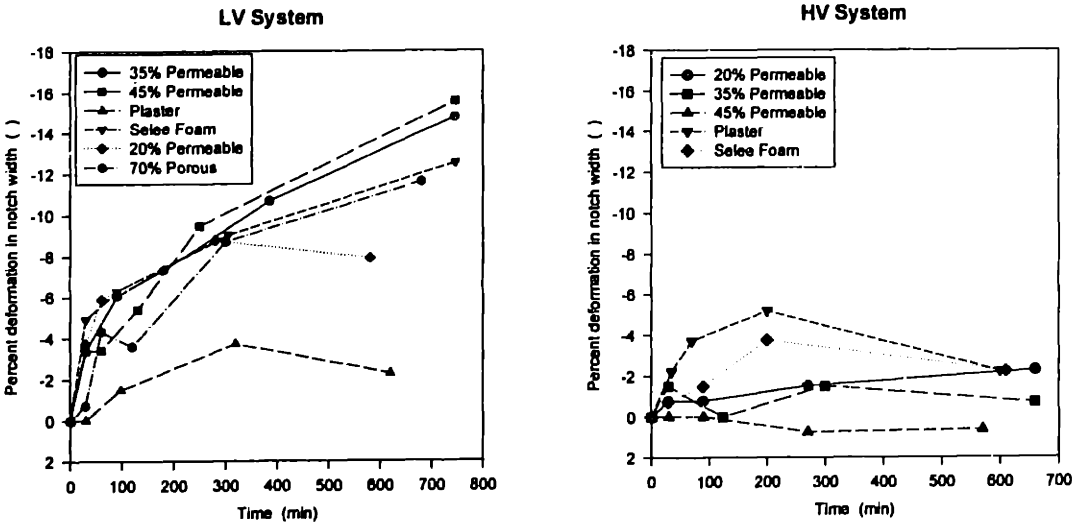

Figure 4.23: Percent deformation in notch dimension as a function of residence time for several types of setters and two binder systems.

All samples showed notch contraction as heat treatment progressed. Differences between deformations in the LV and HV systems can be attributed to the different viscosity of the two binder systems. The HV system samples deformed to lower extent because of the higher viscosity of the binder.

The deformation could not be attributed to shrinkage of the sample due to binder loss. The effect of shrinkage was estimated by measuring the whole width of the sample cross-section. This dimension was chosen since deformations due to slumping should be

minimal according to previous results obtained with the finite element model. Figure 4.24 shows sample shrinkage as a function of residence time and setter type.

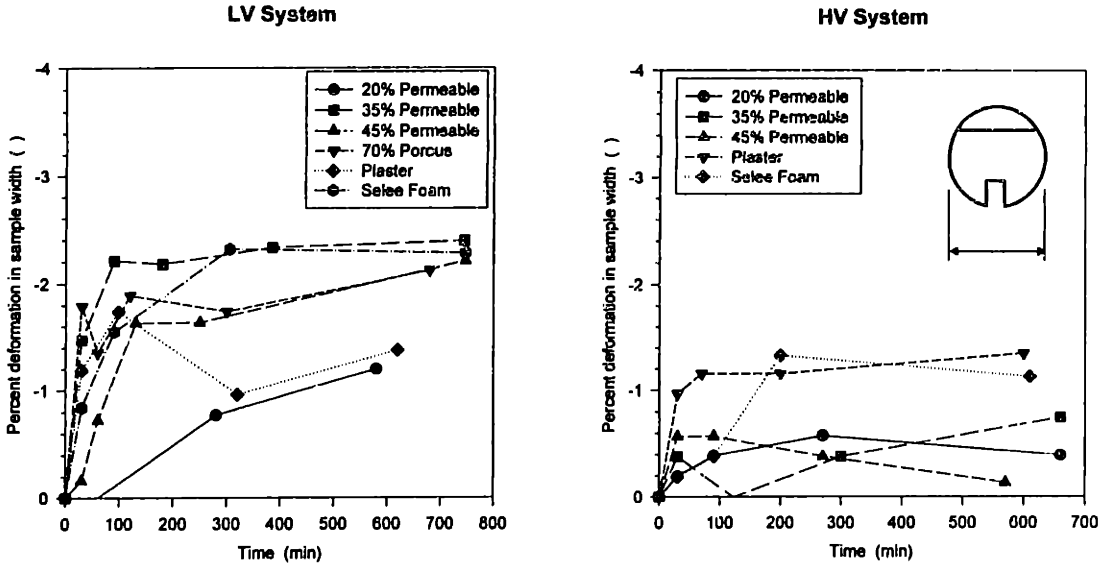

Figure 4.24: Percent shrinkage as a function of time for several types of setters and two binder systems.

The level of shrinkage in the sample is much less than the measured contractions in notch width suggesting that notch contractions are a combination of overall part shrinkage and mostly binder removal phenomenon.

The contraction of the notch can be explained by considering binder concentration gradients within the article during heat treatment. Binder was removed through two contact points located in the lower portion of the sample at 45° angles with respect to the horizontal through the center of the sample. Binder removal, as proven earlier, was not homogeneous throughout the sample. Binder was removed preferentially from areas closer to the sample/setter interface. This means that there was a depletion of binder around the areas surrounding the interfacial area, as proven with TGA tests. These areas, which coincide with the surroundings of the notch, became more viscous than the upper areas of the sample, which were still binder rich and, therefore, soft. The higher stiffness of the area surrounding the notch prevented the onset of local creep;

instead, these areas may be incapable of deforming. Bound by the setter walls and squeezed by the weight of the sample, each of the two notch walls impinged against the upper, softer, areas, rotating inward. This resulted in contraction of the notch.

Indirect confirmation of this theory was also obtained when inverted (upside down) samples where heat treated on porous and non-porous setters (see Appendix B). Preliminary finite element analysis showed that, with this configuration, the notch of the sample was expected to contract. Actual sample deformation on, both, non-porous and porous (Zircar - 70% Porous material) setters, agreed with finite element model. Localized binder extraction had no effect on the notch because of the large distance to the sample/setter interface. Figure 4.25 shows theoretical and experimental change in height vs. time for a sample heat treated on dense setters (the two experimental curves show slightly different results obtained for two LV system samples). There is good correlation between experimental and theoretical deformation but only for initial deformation rates. The finite element model did not predict a non-steady state secondary expansion of the notch. This expansion could not be predicted by the finite element model because the phenomenon is associated with an upward velocity component due to the rotation of the notch walls. Relocation of boundary conditions during deformation may also be involved.

Figure 4.26 shows a plot of sample distortions as a function of binder removal rate for different types of setters. Distortions were defined as

$$Distortion = 1 - \left(\frac{\Delta W / W}{\Delta L / L} \right) \tag{5}$$

W and L are defined in Figure 4.26.

This figure summarizes the effect of binder removal rate on sample distortions. Even if there is considerable scatter, it is possible to see that as binder removal rate increased sample distortions decreased significantly.

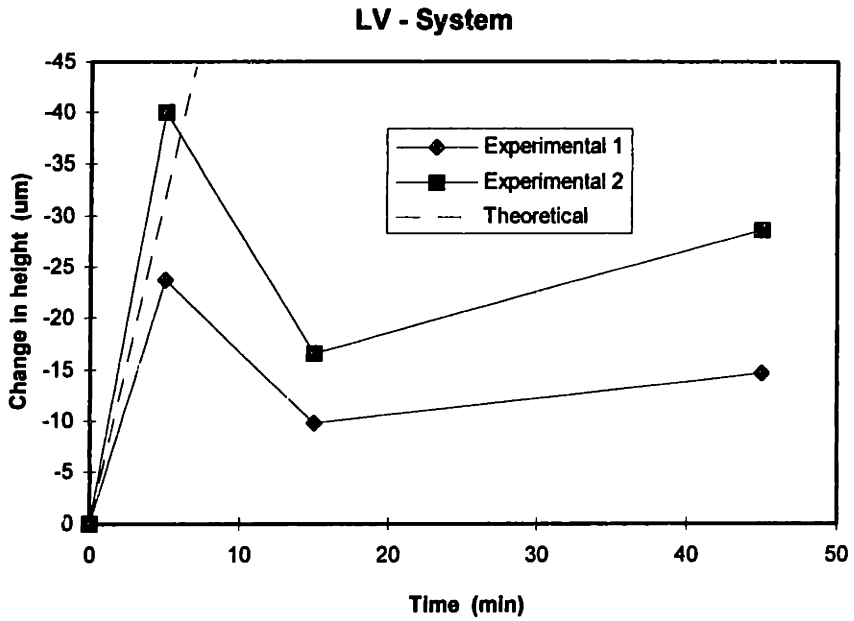

Figure 4.25: Theoretical and experimental height change (Viscosity = 40,000 Pa-sec).

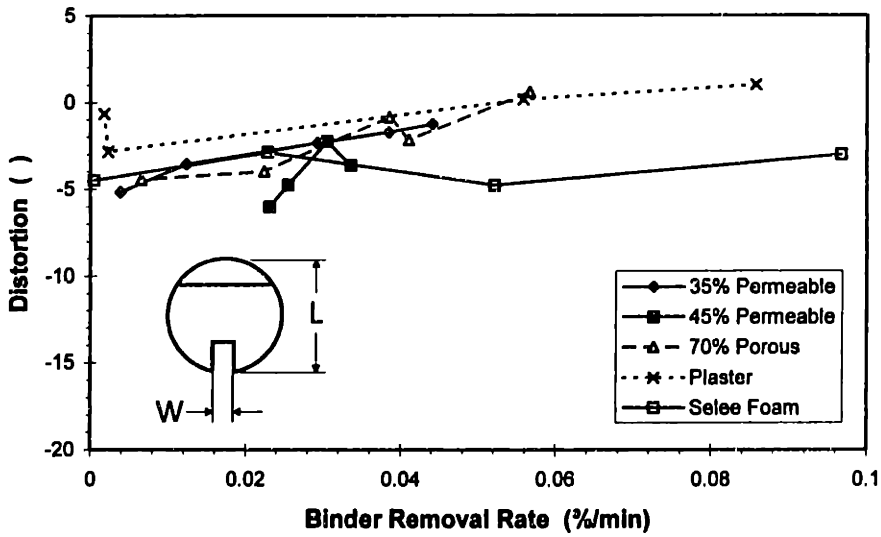

Figure 4.26: Distortion vs. binder removal rate (LV - system)

This phenomenon can be explained as follows. The more viscous the sample, the less it deformed due to gravitational forces, creep. Stiffness is a function of binder content: the lower the binder content the stiffer the sample. As binder was removed from the sample, stiffness increased. Those samples that lost considerable amounts of binder earlier during heat treatment became more viscous in a relatively short time, not enough for the onset of large deformations due to creep. Those samples that did not undergo rapid loss of binder, on the other hand, remained softer and more likely to deform due to creep.

4.4.5 CONCLUSIONS

Deformations in samples heat treated on porous setters were measured, analyzed, and compare to those of samples heat treated on non-porous setters. Considerable differences in deformation behavior were found between the two. These differences were attributed to the presence of binder gradients within the sample. Binder gradients determine relative stiffnesses of different sample locations, influencing the mechanics of deformation of the ceramic article. The binder concentration gradients were measured experimentally. The results suggested that binder deformations were highly coupled with local binder concentrations. Proof was also given of the fact that binder removal rate directly influences overall sample distortions by affecting sample stiffness and susceptibility to creep.

Deformations due to creep behavior and due to binder removal are highly coupled and influence each other in complex ways. It is not possible to estimate accurately sample distortions without simultaneously solving the equations of creep and those governing binder concentration within the sample. More sophisticated tools need to be develop in order to solve this highly non linear set of equations.

[1] M. J. Edirisinghe, J. R. G. Evans, "Fabrication of Engineering Ceramics by Injection Moulding. II. Techniques," Int. J. High Technology Ceramics, **2**, 249-278 (1986)

[2] Patterson, B. R., Aria, C. S., "Debinding Injection Molded Materials by Melt Wicking," TMS

[3] Cima, M. J., "Setter Design for Binder Removal from Injection Molded Ceramic Components," 98th Annual Meeting of the American Ceramic Society, Indianapolis, IN, April 17th, 1996 (Basic Science Division, Paper No. B-193-96).

[4] Bear, J., "Dynamics of Fluids in Porous Media," Dover Publications Inc., New York, 1988.

5. CONCLUSIONS

This thesis has described a study aimed at gaining greater knowledge on how setter characteristics affect binder removal from injection molded ceramic components. The study focused on setter characteristics such as porosity, microstructure, and sample/setter interface geometry and area and their effect on binder removal amounts, rates, and fluxes.

Three main sets of sub-studies were pursued. A series of preliminary experiments was performed to identify deformation mechanisms in the articles of interest. These experiments helped determine the precise time and causes associated with the onset of deformation. A second set of experimental and theoretical studies was directed towards modeling of deformations of components heat treated on non-porous setters. Accuracy of the results was checked by comparison with experimental values. The final set of experiments focused on determining binder removal rates and fluxes and studying their effect of component deformation. The following is a list of the main lessons learned from these studies.

1) Component deformation originates early in the heat treatment process and is due primarily to creep effects associated with the liquefaction of the binder medium.
2) Blister formation occurs only at high heating rates which are not of particular interest since usually not pursued in industry.
3) Components with highly viscous binder systems show smaller deformation than components with low viscosity binder systems since creep rates are drastically reduced.
4) Excellent agreement exists between creep rates predicted by the finite element model and experimentally creep rates of samples heat treated over dense aluminum setters.
5) Setter groove angle has strong effect on sample deformation. It can be optimized to reduce or nullify deformation in a particular dimension of interest.

6) The amount of binder removed from the sample depends on setter porosity and binder system viscosity. Setters with smaller pores exert greater capillary pressure and can, therefore, remove greater amounts of binder. Interfacial geometry does not affect the final amount of binder removed.
7) The components described in this thesis do not undergo particle reorganization during binder removal. Binder is removed from areas immediately surrounding the sample/setter interface, because of the high hydraulic resistance associated with binder removal.
8) Binder removal rate depends strongly on interfacial area. Growth of binder removal rate with interfacial area is, however, less than linear.
9) Binder flux is strongly dependent on binder migration distance, it is not independent of interfacial area. The hydraulic resistance to mass transfer controls the amount of binder that can be removed per unit time.
10) Large interfacial areas are more effective when associated with small binder migration distances.
11) Sample/setter combinations exhibiting higher binder removal rates, in general, deform less than sample/setter combinations with low binder removal rates. High binder removal rates are associated with high viscosities achieved early during heat treatment. This drastically reduces creep rates and, consequently, deformation.
12) Binder concentration has strong effect on sample deformation. Depending on the hydraulic resistance associated with mass transfer, binder gradients can be created within the sample. This influences the viscosity of the binder/powder system. Areas with higher binder concentrations are more likely to deform under creep than areas that are binder depleted because of their higher viscosity.

Important information can be learned from a more detailed and quantitative analysis of binder concentration gradients within the sample. This study should also include the preparation of a finite element model capable of predicting binder concentrations as a function of binder viscosity, setter porosity, particle size,

sample/setter interface area. The conditions necessary to obtain uniform part shrinkage may be derived from this information.

The study of binder migration within the setter may also give greater understanding on the mechanisms controlling binder distribution and setter saturation and on how these factors influence binder removal rates. Anysotropic binder distribution within the setter shows potential for profitable manufacturing applications.

Finally, a comprehensive model of the coupled equations controlling binder concentration within the sample and creep due to gravitational forces may allow to accurately predict deformation rates for any sample and setter geometry.

APPENDIX A

The following is the code used in conjunction with PDEAse2 to model creep behavior of a sample on a non-porous setter. Setter angle can be specified by the user.

```
title "Creep Model - Multiple Setter Angles"
select macsyma
select painthcopy
select printplots = on
ERRLIM = 0.0002

regrid=on
ngrid=20

variables
 U                          { declare U and V to be the system variables }
 V

definitions
 nu                         { define Poisson's Ratio }
 E                          { Young's Modulus x 10**-11 }
 c = e/(1-nu**2)  G = E/[2*(1+nu)]

 ex=dx(u)
 ey=dy(v)
 exy = dx(v)+dy(u)
 sx=c*(ex+nu*ey)  sy=c*(nu*ex+ey)  sxy=G*exy
 Fy                         {Specific Weight [N/m^3]}
 ra = .00167                {radius in m}
 p = .999
 th = 46.5                  {setter angle in degrees}
 K = th*3.141593/180

 {Calculation of sample/setter intersection points}
 q = ra*p/(cos(K))
 temp1 = 2*(1+(tan(K))^2)
 temp2 = (2*tan(K)*p*ra)/cos(K)
 temp3 = 4*(p*ra*tan(K)/cos(K))^2
 temp4 = 4*(ra^2)
 temp5 = ((p/cos(K))^2)-1
 x1 = (1/temp1)* (temp2-(temp3-temp4*temp5*temp1/2)^.5)
 x2 = (1/temp1)* (temp2+(temp3-temp4*temp5*temp1/2)^.5)
 y1 = (tan(K))*x1-q
 y2 = (tan(K))*x2-q
```

```
equations
{plane stress}

{ dx(c*(dx(u)+nu*dy(v)))+dy(G*(dx(v)+dy(u)))=0
 dx(G*(dx(v)+dy(u)))+dy(c*(dy(v)+nu*dx(u)))+Fy=0}

{plain strain}

  dx[((1-nu)/(1+nu))*(E/(1-2*nu))*dx(U)+(nu/(1+nu))*(E/(1-2*nu))*dy(V)] +
       dy[(E/2/(1+nu))*(dx(V)+dy(U))]=0
  dx[(E/2/(1+nu))*(dx(V)+dy(U))] + dy[(nu/(1+nu))*(E/(1-2*nu))*dx(U)+((1-
       nu)/(1+nu))*(E/(1-2*nu))*dy(V)] + Fy = 0


boundaries

  Region 1                    {This is the actual sample}
  {Center at 0,0}
  {radius=1.67 MM}
   nu = 0.3                   { define Poisson's Ratio }

  E  = 120000    G  = E/[2*(1+nu)]


   Fy = - 32.48e3             {Specific Weight of Sample [N/m^3]}

   start (-.0004,-.00162)
   natural (U) = 0
   natural (V) = 0
   line to (-.0004,-.00079) to (.0004,-.00079) to (.0004,-.00162)

   arc (center =0,0) to (x1,y1)
   line to (x2,y2)
   arc (center =0,0) to (0,.00167)

   arc (center =0,0) to (-x2,y2)
   line to (-x1,y1)
   arc (center =0,0) to (-.0004,-.00162)

   finish

   Region 2
   {This is the setter}
```

```
nu = 0.3                    { define Poisson's Ratio}
E  = 10
Fy = 0 {3.247}     {Specific Weight [N/m^2]}


start (0,-q)
natural (U) = 0
natural (V) = 0
value (U) =0
value (V) =0
line to (x2,y2)
natural (U) = 0
natural (V) = 0
value (U) =0
value (V) =0
line to (x2+.001,tan(K)*(x2+.001)-q)
natural (U) = 0
natural (V) = 0
value (U) =0
value (V) =0
line to (x2+.001,-q-.001)
natural (U) = 0
natural (V) = 0
value (U) =0
value (V) =0
line to (-(x2+.001),-q-.001)
natural (U) = 0
natural (V) = 0
value (U) =0
value (V) =0
line to (-(x2+.001),tan(K)*(x2+.001)-q)
natural (U) = 0
natural (V) = 0
value (U) =0
value (V) =0
line to (0,-q)
finish


feature                     {form a semicircular arc for better gridding resolution
                            and radius = .95% of orginal}
start(-ra*.95,0)
arc (center= 0,0) angle=70

feature
start (ra*.95,0)
```

```
   arc (center=0,0) angle=-70



monitors
   grid(x+U,y+V)     { show deformed grid as solution progresses }

plots                { hardcopy at finish: }
  grid(x,y) pause
  grid(x+U,y+V)      { show final deformed grid }
  vector(U,V) as "Flow Characteristics (m/sec)" pause { show displacement field }

  contour(sx) as "X-Stresses"  pause  contour(sy) as "Y-Stresses" pause
  contour(U) as "X-Deformation Rate"  pause
  contour(V) as "Y-Deformation Rate" pause
  contour(V) as "Y-Deformation Rate" zoom(-.001,.001,.0015,.0015) pause
  contour(V) as "Y-Deformation Rate" zoom(-.0005,-.002,.002,.002) pause
  contour(((U^2)+(V^2))^0.5) as "Magnitude of Deformation Rate"



end
```

APPENDIX B

The following is the code used in conjunction with PDEAse2 to model creep behavior of an inverted sample on a non-porous setter.

```
title "Creep Model - Inverted Sample - 45 Deg."
select macsyma
select painthcopy
select printplots = on
ERRLIM = 0.0002

regrid=on
ngrid=20



variables
 U                          { declare U and V to be the system variables }
 V

definitions
 nu                         { define Poisson's Ratio }
 E                          { Young's Modulus x 10**-11 }
 c = e/(1-nu**2)  G = E/[2*(1+nu)]


 ex=dx(u)
 ey=dy(v)
 exy = dx(v)+dy(u)
 sx=c*(ex+nu*ey)  sy=c*(nu*ex+ey)  sxy=G*exy
 Fy                         {Specific Weight [N/m^3]}
 ra = .00167                {radius in m}
 p = .999
 a = ra*p
 q = -2*a/((2)**.5)
 x1 = (-2*q-(8*(ra**2)-4*(q**2))**(.5))/(4)
 x2 = (-2*q+(8*(ra**2)-4*(q**2))**(.5))/(4)
 y1 = x1+q
 y2 = x2+q



equations
  {plane stress}
{ dx(c*(dx(u)+nu*dy(v)))+dy(G*(dx(v)+dy(u)))=0
```

```
dx(G*(dx(v)+dy(u)))+dy(c*(dy(v)+nu*dx(u)))+Fy=0}

  {plain strain}

dx[((1-nu)/(1+nu))*(E/(1-2*nu))*dx(U)+(nu/(1+nu))*(E/(1-2*nu))*dy(V)] +
dy[(E/2/(1+nu))*(dx(V)+dy(U))]=0
dx[(E/2/(1+nu))*(dx(V)+dy(U))] + dy[(nu/(1+nu))*(E/(1-2*nu))*dx(U)+((1-
nu)/(1+nu))*(E/(1-2*nu))*dy(V)] + Fy = 0


boundaries

  Region 1
  {This is the actual sample}
  {Center at 0,0}
  {radius=1.67 MM}
   nu = 0.3          { define Poisson's Ratio }

  E  = 120000    G  = E/[2*(1+nu)]


   Fy = - 32.48e3              {Specific Weight of Sample [N/m^3]}

   start (.0004,.00162)
   natural (U) = 0
   natural (V) = 0
   line to (.0004,.00079) to (-.0004,.00079) to (-.0004,.00162)

   arc (center =0,0) to (-x2,y2)
   line to (-x1,y1)
   arc (center =0,0) to (0,-.00167)

   arc (center =0,0) to (x1,y1)
   line to (x2,y2)
   arc (center =0,0) to (.0004,.00162)

   finish

   Region 2
   {This is the surface on which the cylinder is sitting on}
   nu = 0.3                    {define Poisson's Ratio }
   E  = 1e40
   Fy = 0                      {Specific Weight [N/m^3]}


   start (0,q)
```

```
  natural (U) = 0
  natural (V) = 0
  value (U) =0
  value (V) =0
  line to (x2,y2)
  natural (U) = 0
  natural (V) = 0
  value (U) =0
  value (V) =0
  line to (x2+.001,y2+.001)
  natural (U) = 0
  natural (V) = 0
  value (U) =0
  value (V) =0
  line to (x2+.001,y2-.0025)
  natural (U) = 0
  natural (V) = 0
  value (U) =0
  value (V) =0
  line to (-(x2+.001),y2-.0025)
  natural (U) = 0
  natural (V) = 0
  value (U) =0
  value (V) =0
  line to (-(x2+.001),y2+.001)
  natural (U) = 0
  natural (V) = 0
  value (U) =0
  value (V) =0
  line to (0,q)
  finish


  feature                    {form a semicircular arc for better gridding resolution
                              and radius = .95% of orginal}
    start(-ra*.95,0)
    arc (center= 0,0) angle=70

  feature
    start (ra*.95,0)
    arc (center=0,0) angle=-70


monitors
  grid(x+U,y+V)              { show deformed grid as solution progresses }
```

```
plots                          { hardcopy at finish: }
  grid(x,y) pause
  grid(x+U,y+V)                { show final deformed grid }
  vector(U,V) as "Flow Characteristics (m/sec)" pause { show displacement field }

  contour(ex) as "X-Stresses"  pause  contour(ey) as "Y-Stresses" pause
  contour(U) as "X-Deformation Rate"  pause
  contour(V) as "Y-Deformation Rate" pause
  contour(V) as "Y-Deformation Rate" zoom(-.0005,-.002,.002,.002) pause
  contour(((U^2)+(V^2))^0.5) as "Magnitude of Deformation Rate"
  zoom (-ra,-ra,ra,ra) }


end
```